

# Observed Evidences of Frequency-Dependent Site Spectral Amplification due to Strong Structural Control of Active Reverse Faults at Different Three Localities in Japan

Mostafa Thabet (✉ [mostafa.thabet@aun.edu.eg](mailto:mostafa.thabet@aun.edu.eg))

Assiut University Faculty of Science <https://orcid.org/0000-0001-5856-6064>

---

## Research Article

**Keywords:** Fault zone, Guided waves, Site response, Fourier spectrum, Spectral ratio, KiK-net and K-NET (Japan).

**Posted Date:** July 26th, 2021

**DOI:** <https://doi.org/10.21203/rs.3.rs-606889/v1>

**License:**  This work is licensed under a Creative Commons Attribution 4.0 International License.

[Read Full License](#)

---

1 **Observed Evidences of Frequency-Dependent Site Spectral Amplification**  
2 **Due To Strong Structural Control of Active Reverse Faults at Different**  
3 **Three Localities in Japan**

4 Mostafa Thabet<sup>1,2,\*</sup>

5 <sup>1</sup>*Lecturer, Geology Department, Faculty of Science, Assiut University, Assiut 71516, Egypt*

6 <sup>2</sup>*M.Sc. and Ph.D., Geoscience Division, Graduate School of Science, Osaka City University, Osaka, Japan*

7 *\*Corresponding Author,*

8 E-mail: [mostafa.thabet@aun.edu.eg](mailto:mostafa.thabet@aun.edu.eg)

9 Web: <http://www.aun.edu.eg/membercv.php?M%20ID=422>

10 <https://scholar.google.com/citations?user=wPsYhrMAAAAJ&hl=en>

11 [http://www.researchgate.net/profile/Mostafa\\_Thabet2](http://www.researchgate.net/profile/Mostafa_Thabet2)

12  
13 ORCID ID: 0000-0001-5856-6064

14 Scopus Author ID: 23101743600

15  
16 Tel: (002) – 01275134332 (mobile) and (002) – 088 – 2412223 (work)

17 Fax: (002) – 088 – 2342223 (work)

18

19

## Abstract

20 In the present study, observed active fault zone related site amplification is calculated based on Fourier  
21 acceleration spectrum (FAS) at three different localities in Japan. For this purpose, the FASs are  
22 calculated using 26432 earthquakes recorded at 126 K-NET and KiK-net seismic stations, which are  
23 distributed on the fault zones and upthrown and downthrown sides. This observed amplification is  
24 strongly frequency-dependent because of the presence of the near-surface low-velocity flower fault  
25 structure and the deeper fault zone. Moreover, the amplification patterns at each study area are  
26 tectonic-specific patterns. Sources inside the active fault zones could produce amplification at high  
27 frequencies at stations on both fault zone and far away from the fault zone. This is because of the  
28 impact of the near-surface fault zone. Sources outside the active fault zones could not produce  
29 significant amplification at high frequencies, whereas remarkable high amplification at low  
30 frequencies exhibits a gradual increase through stations on hanging walls, fault zones, and footwalls.  
31 Remarkably, low-frequency amplification due to sources outside the active fault zones at stations on  
32 footwalls is much higher than those observed on hanging walls. Interestingly, the peaks of the low-  
33 frequency amplification are corresponding to wavelengths that approximately equalize the width of the  
34 fault zone. Diffuse field theory inversion using earthquake horizontal-to-vertical spectral ratio  
35 (EHVSR) could successfully detect the presence of fault zone low-velocity layers. However, analyzing  
36 the fault zone related site effects using HVSr is not effective because of the strong amplification  
37 related structural control of the active fault zones on the ground motions.

38

39 *Keywords: Fault zone, Guided waves, Site response, Fourier spectrum, Spectral ratio, KiK-net and K-*  
40 *NET (Japan).*

41

## 42 1. Introduction

43 Because many industrial and/or metropolitan areas are built on alluvial fans or basins, a correct  
44 quantification of the local site effects is necessary for a systematic and robust assessment of seismic  
45 hazards due to the direct relation with significant seismic damage and consequent loss of life. The  
46 amplification of an earthquake signal at a site plays a significant role in increasing seismic damage.  
47 The seismic site response due to fault zones has important implications on earthquake hazard on a  
48 local scale causing amplified motions near faults due to guided waves. Valuable research works by Li  
49 *et al.* (1994) and Li and Leary (1990) on fault zone guided waves due to the San Andreas Fault zone  
50 grow attention to this issue. Constructive interference between reflected seismic waves is responsible  
51 for generating highly amplified fault zone guided waves and later arrivals of dispersive energy after  
52 *S*-waves (Igel *et al.* 1997; Ben-Zion and Aki 1990). Fault gouge, clay-rich fault gouge, fracturing,  
53 increased porosity, remineralization, crack dilatation, and pore-fluid concentration near fault zones  
54 are the possible causes for this low-velocity zone (Thurber 1983; Cormier and Spudich 1984;  
55 Mooney and Ginzburg 1986; Li and Leary 1990; Ben-Zion 1998; Ben-Zion and Sammis 2003;  
56 Hickman *et al.* 2005).

57  
58 Recently, studies by Peruzza *et al.* (2017) and Tortorici *et al.* (2019) were focused on analyzing the  
59 site effects due to the presence of fault zones. Ground motion amplification of directional effects  
60 along polarized horizontal component could be observed because of active faults and extended  
61 fractures (*e.g.* Spudich *et al.*, 1996). These directional effects are observed on horizontal amplitude  
62 variations versus azimuth of fault zones (Rigano *et al.*, 2008; Pischiutta *et al.*, 2015; Panzera *et al.*,  
63 2017a) indicating *S*-wave velocity anisotropy (*i.e.* fast *S*-waves are parallel to fault zone, whereas the  
64 slow *S*-waves are normal causing high amplification).

65  
66 Many researchers such as Rigano *et al.* (2008), Di Giulio *et al.* (2009), Pischiutta *et al.* (2012, 2013,  
67 2015, 2017), Panzera *et al.* (2014, 2016a, 2016b, 2017a, 2017b), Burjánek *et al.* (2012), Panzera *et al.*  
68 (2019), Tortorici *et al.* (2019), and Kakhki *et al.* (2020) used the horizontal-to-vertical spectral ratios  
69 (HVSR) of earthquake and ambient vibration data to reveal the site effects related to fault zones.  
70 They observed systematic directional amplification normal to the dominant fault strike. Panzera *et al.*  
71 (2020) studied the site effects considering tectono-stratigraphic setting of the Santa Caterina area in  
72 Italy and observed maximum directional HVSR amplification of 8 in the perpendicular azimuth of the  
73 dominant N-S fracture zone. In contradict to these studies, Villani *et al.* (2018) did not observe any  
74 significant directional effects through their geophysical investigation at the Victoria fault in Malta.  
75 They interpreted their results because of the present inactivity in the fault zone, which is expressed in  
76 terms of ~ 0.6 Myr ago. Pischiutta *et al.* (2017) found a predominant high horizontal amplification in  
77 the NE-SW to NNE-SSW direction (*i.e.* fault perpendicular direction) across the Vado di Corno fault  
78 in Italy, which is considered as active normal faults during the L'Aquila 2009 earthquake. Di Giulio *et*  
79 *al.* (2009) conducted dense microtremor measurements along and across the intensely fractured zones  
80 of the Pernicana fault, Mount Etna, Italy. They observed strong directional horizontal amplification at  
81 1 Hz close to the highly fractured zone.

82  
83 The existence of seismic stations across the fault provides a good opportunity in identifying these  
84 guided waves. According to studies by Igel *et al.* (2002), Jahnke *et al.* (2002), and Fohrmann *et al.*  
85 (2004), moderate variations of fault zone properties could produce guided waves. Seismogenic depths  
86 > 10 km could act as fault zone waveguide according to studies by Li *et al.* (1997, 2000, and 2004),  
87 Li and Vernon (2001), Korneev *et al.* (2003), Mizuno *et al.* (2004), and Mizuno and Nishigami

88 (2006). Moreover, Ben-Zion and Aki (1990), Ben-Zion (1998), Michael and Ben-Zion (1998),  
89 Rovelli *et al.* (2002), Peng *et al.* (2003), and Lewis *et al.* (2005) proved significant trade-offs between  
90 propagation distance along the fault zone, fault zone width, impedance contrasts between massive and  
91 damaged rock, and source location. Fault zone-related site effects are extensively studied by many  
92 researchers in fault zone stations due to sources not necessarily in the fault zone. Li and Leary (1990)  
93 and Li *et al.* (1990, 1997) used a small number of selected waveforms to study the fault zone guided  
94 waves due to 100 m wide of low-velocity fault zone extending to the seismogenic depth. In  
95 California, 1500 weak ground motions on fault zone arrays were studied by Li and Vernon (2001).  
96 Shallow fault zone could behave as a waveguide due to very deep ground motions and far from the  
97 fault zone (Jahnke *et al.* 2002; Igel *et al.* 2002; Fohrmann *et al.* 2004). Roux *et al.* (2016) and Ben-  
98 Zion *et al.* (2015) used spatially high dense seismic array (*i.e.* 1108 vertical geophones, with  
99 instrument spacing of 10 m to 30 m and sampling interval of 200 Hz) to study the structural image of  
100 the subsurface material in the damage zone of the San Jacinto fault in California.

101  
102 The role of active fault zones in affecting the earthquake hazard estimation is playing an important  
103 role in evaluating the seismic risk analyses. In Japan, a comprehensive database of active faults is  
104 provided by the National Institute of Advanced Industrial Science and Technology (AIST:  
105 [https://gbank.gsj.jp/activefault/index\\_e\\_gmap.html](https://gbank.gsj.jp/activefault/index_e_gmap.html), last accessed January 2021). These active faults  
106 are subdivided into several strands and characterized by their surface trace geometry, rupture history,  
107 slip per event, slip rate, calculated future rupture probability, and recurrence interval. These  
108 characteristics are evaluated based on paleoseismic and geologic studies. To improve the database  
109 system, all these characteristics are compiled based on previous studies, such as, Matsubara and  
110 Obara (2011), Nishida *et al.* (2008), Matsubara *et al.* (2008), Nakamura *et al.* (2008), Abdelwahed

111 and Zhao (2007), Nakajima and Hasegawa (2007a, b, and c), Kato *et al.* (2006), Nakajima *et al.*  
112 (2001), Zhao *et al.* (1996), to cite few among many others. Therefore, the present research work is  
113 originated based on the AIST database of active faults in Japan.

114

115 Motivated by these aforementioned valuable previous studies and the valuable AIST database of  
116 active faults, the present research work is established taking into account that strong variation in  
117 amplitude and frequency content of surface ground motions are strongly related to fault zone's  
118 geometry and seismic properties at depth. The present study is reported observed evidence of active  
119 reverse fault zone-related site spectral characteristics at three different localities in Japan using 26432  
120 earthquakes recorded at 126 K-NET and KiK-net seismic stations. The spectral characteristics of the  
121 ground motions on the footwall (*i.e.* downthrown wall), fault zone, and the hanging wall (*i.e.*  
122 upthrown wall) are investigated by the Fourier acceleration spectrum of the surface orthogonal  
123 components, the HVSR, and the surface-to-borehole spectral ratio. Comparisons among these  
124 techniques are also implemented as a procedure for identifying and analyzing site spectral  
125 amplifications. Considering that reverse faults at those three different localities in Japan have similar  
126 main fault strike, the resulted site spectral amplifications could be possibly inferred to the dominant  
127 fault dip, the dominant frequency caused by the fault zone width, and the different fracture patterns  
128 due to the existence of a dense network of minor and major active faults, and the seismic properties of  
129 the fault zone (*P*-wave and *S*-wave velocities, Poisson's ratio, and perturbation velocities).

130

131

132

## 133 2. Tectonic Patterns and Subsurface Tomography

134 In this study, active reverse faults with a predominant strike of north-south are studied. The study  
135 areas of this work (Figure 1) are located in East Hokkaido, Akita-Iwate, and Fukushima in Japan.

136  
137 The East Hokkaido active reverse faults, which are showing arc-shaped alignment, are composed of  
138 four major behavioral segments, including Shihoro, Otofuke, Tobetsugawa, and Kochien segments  
139 (Figure 2). The first three behavioral segments (*i.e.* Shihoro, Otofuke, and Tobetsugawa) are trending  
140 eastwards dipping reverse faults (dip azimuth/dip angle = N10/30°, N0/30°, and N0/30°, respectively)  
141 along the eastern side of the Tokachi Plain in central Hokkaido. The fourth behavioral segment (*i.e.*  
142 Tobetsugawa) is trending northeastwards dipping reverse fault (dip azimuth/dip angle = N330/45°)  
143 along the eastern side of the Hidaka Mountains in central Hokkaido. The maximum slip rate is  
144 belonging to Shihoro behavioral segment, is estimated based on the vertical displacement of dated  
145 terrace surfaces (Togo 2000) at 0.4 m over about 1000 years with 7.2 m slip per event. Table 1 is  
146 showing detailed characteristics of these behavioral segments as obtained from AIST (2012, 2013).

147  
148 The active reverse fault system in the Akita-Iwate study area is composed of a set of several en-  
149 echelon behavioral segments (Figure 3). Those behavioral segments of this active reverse fault  
150 system have their footwall blocks (*i.e.* downthrown sides) located on the right and left sides of the  
151 study area, whereas their hanging wall blocks (*i.e.* upthrown sides or the main fault zone) located in  
152 the center of the study area. As a result, the reverse fault system in the Akita-Iwate study area could  
153 be considered as a horst fault system. However, this active reverse fault system in the Akita-Iwate  
154 study area could be accommodated in three major parallel active reverse fault stands. The first major

155 fault stand is composed of Ukai, Hanamaki, and Kitakami-nishi behavioral segments and are trending  
156 westwards dipping reverse fault (dip azimuth/dip angle = N10/45°, N10/45°, and N350/45°,  
157 respectively) along the western margin of the Kitakami Basin in northern Honshu. The second is  
158 composed of Shizukuishibonchi-seien, Kawafune, and Warikurayama behavioral segments.  
159 Shizukuishibonchi-seien reverse fault is trending westwards dipping (dip azimuth/dip angle =  
160 N10/45°) along the western margin of the Shizukuishi Basin in northern Honshu. Kawafune has NNE-  
161 SSW trending westwards dipping reverse fault (dip azimuth/dip angle = N20/45°) along the eastern  
162 margin of the Mahiru Mountains in northern Honshu. This fault is ruptured because of the 1896  
163 Rikuu earthquake. Warikurayama is trending westwards dipping reverse fault (dip azimuth/dip angle  
164 = N0/45°) along the eastern margin of the Mahiru Mountains in northern Honshu. The third is  
165 composed of Tazawako-toho, Senya, Kanazawa, and Omoriyama behavioral segments and are  
166 trending eastwards dipping reverse fault (dip azimuth/dip angle = N0/45°, N10/30°, N0/45°, and  
167 N350/45°, respectively). Tazawako-toho segment extends along the eastern shore of Lake Tazawa in  
168 northern Honshu, whereas Senya, Kanazawa, and Omoriyama segments are extending along the  
169 eastern margin of the Yokote Basin in northern Honshu. Tazawako-toho and Senya segments are also  
170 ruptured because of the 1896 Rikuu earthquake. Senya and Hanamaki behavioral segments exhibit  
171 the highest slip rate at 0.8 m over about 1000 years and the highest slip per event of 4.9 m,  
172 respectively. Table 2 is summarizing the characteristics of these behavioral segments as obtained  
173 from AIST (2012, 2013). Moreover, sub-parallel active reverse faults stands are located westwards in  
174 the Akita-Iwate study area. They are composed of Takinosawa and Nakacho segments and are  
175 trending westwards dipping reverse fault (dip azimuth/dip angle = N0/45° and N20/45°, respectively),  
176 whereas Toridame and Kitayuri segments and are trending eastwards dipping reverse fault with dip  
177 azimuth/dip angle = N0/45°.

178

179 Fukushima's active fault system is composed of two sets of behavioral segments (Figure 4). Along  
180 the eastern margin of the Abukuma Mountains in northern Honshu, Watari and Namie segments are  
181 trending westwards dipping reverse fault with dip azimuth/dip angle = N350/80°, while Haramachi  
182 and Sangunmori segments are trending left-lateral strike-slip faults with vertical displacement of  
183 west-side-up and east-side-up, respectively. Table 3 is showing detailed characteristics of these  
184 behavioral segments as obtained from AIST (2012, 2013).

185

186 Understanding the physical properties of the subsurface structure of these large active reverse faults is  
187 an important step towards the understanding of the related site effects on those faults. AIST provides  
188 physical property in two dimension subsurface structures, such as velocities of *P*-wave and *S*-wave,  
189 Poisson's ratio, and perturbation velocities of *P*-wave and *S*-wave, through their subsurface structures  
190 visualization system. In this research work, these physical property structures beneath the  
191 aforementioned active reverse faults are created and viewed for the profiles, which are selected  
192 beforehand in each study area. In the present paper, the velocities of *P*-wave and *S*-wave beneath the  
193 selected profiles are depending on the valuable study by Nakamura *et al.* (2008).

194

195 Profile AB in the East Hokkaido study area is shown in Figure 5. The active reverse fault, which is  
196 dipping eastwards, extends to 30 km depth with Poisson's ratio of 2.2, and *P*-wave and *S*-wave  
197 velocities of 5.5 and 3 km/s, respectively. The intensely damaged and fractured fault material  
198 compared with the high velocities of massive surrounding rocks (footwall and hanging wall blocks)

199 are indicated by lower velocity perturbations of *P*-wave and *S*-wave (~ 8% lower than the initial  
200 velocity structures).

201  
202 In the Akita-Iwate study area, CD and EF profiles are created and viewed using AIST's visualization  
203 system for subsurface structures based on Nakamura *et al.* (2008). The subsurface structures at CD  
204 and EF profiles are shown in Figure 6 and Figure 7, respectively. In profile CD, the reverse faults  
205 dipping eastwards, which are represented in reduced physical property, are seen particularly in the  
206 subsurface structures of *P*-wave velocity perturbations, whereas westwards dipping reverse faults are  
207 losing their reduced physical property evidence. Conversely, the reverse faults dipping westwards are  
208 seen in profile EF when compared with reverse faults dipping eastwards that are losing their reduced  
209 physical property evidence. This lateral discontinuity reveals that Akita-Iwate's fault system is  
210 undergoing a significant activity.

211  
212 At profile GH in the Fukushima study area, the subsurface structures of *P*-wave and *S*-wave  
213 velocities, Poisson's ratio, and perturbation of *P*-wave and *S*-wave velocities are created and viewed  
214 in Figure 8 and Figure 9 based on Nakamura *et al.* (2008) and Nakajima *et al.* (2001), respectively.  
215 The reduced physical property in this active fault system could not be exhibited as seen in the East  
216 Hokkaido active fault system. This could be related to two reasons. First, the currently active fault  
217 trace could accommodate a maximum slip rate that is estimated at 0.1 m over about 1000 years with  
218 2.4 m slip per event. Second, Fukushima active fault system might be young. Consequently, this lack  
219 of reduced physical properties has occurred clearly across the entire fault zone in the Fukushima  
220 study area.

### 221 3. Data and Methods

222 To study site spectral amplification across and along active reverse faults at the aforementioned three  
223 different localities in Japan, K-NET and KiK-net database (<https://www.kyoshin.bosai.go.jp>, last  
224 accessed, January 2020) is used. Dense seismic stations of K-NET and KiK-net are present at those  
225 three different localities of the present study, which are the East Hokkaido, Akita-Iwate, and  
226 Fukushima study areas (Figure 1).

227  
228 Location maps of K-NET and KiK-net seismic stations in the East Hokkaido, Akita-Iwate, and  
229 Fukushima study areas are shown in Figure 2, Figure 3, and Figure 4, respectively. Those stations  
230 located on the footwall (FW) block are differentiated from those located on the hanging wall (HW)  
231 block. Few stations are distributed on the surface of the fault zone (FZ) at the East Hokkaido and  
232 Akita-Iwate study areas, whereas no stations at all are distributed on the FZ in the Fukushima study  
233 area. Accordingly, earthquakes recorded at these stations are also classified based on the locations of  
234 their hypocenters. They are earthquakes having their hypocenters beneath footwall (EFWs), fault  
235 zone (EFZs), hanging wall (EHWs) blocks.

236  
237 A total of manually selected 126 seismic stations, which are maintained by K-NET and KiK-net, are  
238 distributed on FW, FZ, and HW blocks at the three study areas. Additionally, a total of automatically  
239 selected 26432 earthquakes were recorded at those 126 K-NET and KiK-net seismic stations from  
240 May 1996 to January 2020. The selection of earthquakes depends on two criteria. First, only  
241 earthquakes with PGAs (*i.e.* Peak Ground Accelerations) of  $\leq 10 \text{ cm/s}^2$  are used in the present study  
242 to characterize the linear response at each seismic station and avoid later modification due to  
243 nonlinear response (Thabet 2008a, b, 2021). Figure 10 is showing correlations between surface and

244 borehole PGAs using KiK-net stations. Second, the hypocenters of these earthquakes must not exceed  
245 the predefined areas that are shown in Figures 2, 3, and 4. Table 4 is summarizing the detailed  
246 numbers of seismic stations with their corresponding recorded earthquakes at the three study areas.

247  
248 Ben-Zion *et al.* (2003) noted that stations located on the fault zone have motion amplification not  
249 only in the *S*-wave trains but also in the *P*-wave and other portions of the seismograms. Moreover,  
250 they observed that differences between waveforms recorded on fault zone and far from it are  
251 generated by nearly all events (*i.e.* on fault zone and far from it) and they exist not only in fault-  
252 parallel seismograms but also in the other components. Therefore, three orthogonal continuous time  
253 series are prepared at each seismic station in the present study based on the multiple-earthquakes  
254 approach of Thabet (2019), which are representing EFWs, EFZs, and EHWs. Consequently, the  
255 structural control due to the presence of active reverse faults could be observed and interpreted at  
256 each seismic station. Figure 11 is showing an example of three continuous time series of east-west  
257 components (EW) at the TKCH05 KiK-net seismic station, including 111, 26, and 140 recorded  
258 EFWs, EFZs, and EHWs, respectively. Adopting this multiple-earthquakes approach enables us to  
259 study only the structural control of active reverse faults excluding effects of different earthquake  
260 sources with different propagation paths.

261  
262 In engineering seismology, the site effects are usually studied in the frequency domain as variations  
263 of seismic wave's amplitude. There are various spectral ratio methods, which effectively reveal how  
264 active reverse fault zones modify the seismic waves. Since pioneering studies by Nogoshi and  
265 Igarashi (1970, 1971) and Nakamura (1989, 2000), horizontal-to-vertical spectral ratio is the usual  
266 technique for realistically estimate the predominant and fundamental frequencies at a site (Lermo and

267 Chavez-Garcia 1993; Seekins *et al.* 1996; Thabet 2019). The applicability of horizontal-to-vertical  
 268 spectral ratio (HVSR) is tested by Rigano *et al.* (2008) concluding good results on the surface of  
 269 faults. Moreover, surface-to-borehole spectral ratio (SBSR) is early introduced by Borchardt (1970,  
 270 1994), which is considered as the base of other later studies. The resulted in resonant frequencies are  
 271 only characteristic of the soil column between the surface and borehole sensors.

272  
 273 Using Geopsy software (Wathelet 2005; <http://www.geopsy.org>), the Fourier acceleration spectrum  
 274 (FAS) of the three orthogonal continuous time series and their HVSRs are calculated. During  
 275 calculations, and following the SESAME (2004) guidelines, the reliability and quality of these FAS  
 276 and HVSR calculations are checked to yield an acceptable level of scattering (*i.e.* acceptable low  
 277 standard deviation values) that may significantly influence the physical meaning of the FAS and  
 278 HVSR curves. At KiK-net seismic stations only, the SBSRs are calculated using the orthogonal FAS.

279  
 280 To estimate the site spectral amplification (SSA) at each seismic station, equations 1 through 4 are  
 281 used.

$$SSA_{OH} = \frac{S_O}{S_H} \quad ; \quad SSA_{O/L.F} = \frac{S_O}{S_{L.F}} \quad (1)$$

$$SSA_{OF} = \frac{S_O}{S_F} \quad ; \quad SSA_{O/r.F} = \frac{S_O}{S_{r.F}} \quad (2)$$

$$SSA_{HF} = \frac{S_H}{S_F} \quad ; \quad SSA_{l.F/r.F} = \frac{S_{L.F}}{S_{r.F}} \quad (3)$$

$$SSA_{FH} = \frac{S_F}{S_H} \quad ; \quad SSA_{r.F/L.F} = \frac{S_{r.F}}{S_{L.F}} \quad (4)$$

282 where  $S$  could be FAS, HVSR, or SBSR curves (Note: left side equations are applied on the East  
283 Hokkaido and Fukushima study areas, whereas right side equations are applied on the Akita-Iwate  
284 study area).  $F$ ,  $H$ , and  $O$  terms are referring to earthquakes located beneath footwall block, hanging  
285 wall block, and fault zone (*i.e.* hanging wall blocks in the Akita-Iwate study area), respectively.  $r.F$   
286 and  $l.F$  terms are referring to earthquakes located beneath the right and left footwall blocks (Er.FWs  
287 and El.FWs), respectively, in the Akita-Iwate study area.

288  
289 For the purpose of measuring how the active reverse faults modify the amplification spectrum,  
290 equations 3 and 4 are used at stations on FW in East Hokkaido and Fukushima study areas or right  
291 footwall (r.FW) block in Akita-Iwate study area, and HW in East Hokkaido and Fukushima study  
292 areas or left footwall (l.FW) block in Akita-Iwate study area, respectively. To quantify the behavior  
293 of the site spectral amplifications at seismic stations located on different fault blocks, the average site  
294 spectral amplifications are calculated and bounded with their minimum and maximum amplification.

295  
296 To examine the velocity structures beneath the fault zones, earthquake HVSR (EHVSR) inversions  
297 are carried out using inversion code program developed by Nagashima *et al.* (2014, 2017), which is  
298 specifically designed for calculating the theoretical EHVSR based on the diffuse field concept. As a  
299 result, it would be possible to confirm the presence of the low-velocity fault zone.

300

#### 301 **4. Estimation of Site Effects**

302 The link between the fault zone and the spectral analyses of earthquakes has been a long-standing  
303 fundamental problem. It is important for acquiring insight into the physical characteristics of fault  
304 zone guided waves and predicting future ground motions for engineering purposes. The resulted site

305 effects of the present analyses consist of (1) FASs of seismic stations located on FW, FZ, and HW  
306 blocks, independently, and (2) calculations of the averaged SSAs at each independent zone. In the  
307 following sections, results are presented with discussions to interpret the resulted amplification  
308 patterns at the three study areas in the present research work.

309

#### 310 **4.1 East Hokkaido Study Area**

311 In the East Hokkaido study area, Figures 12, 13, and 14 are showing FASs results for stations on FW,  
312 FZ, and HW blocks, respectively. Obviously, the recorded EFZs yield maximum Fourier amplitude in  
313 the high-frequency band (*i.e.* approximately  $> 3$  Hz) at all stations. Moreover, recorded EHWs yield  
314 maximum Fourier amplitude in the low-frequency band (*i.e.* approximately  $< 3$  Hz), particularly at  
315 stations located on FW block and FZ (Figure 12 and Figure 13, respectively). These frequency-  
316 dependent maximum Fourier amplitudes are strongly related to the presence of the active reverse fault  
317 system. For example, the example of continuous-time series of TKCH05 KiK-net station (Figure 11)  
318 is showing very low PGAs for recorded EFZs when compared with those recorded EFWs and EHWs.  
319 However, the FASs of recorded EFZs at TKCH05 (Figure 14) are showing maximum Fourier  
320 amplitude in the high-frequency band (*i.e.* approximately  $> 3$  Hz) in all orthogonal components. For  
321 seismic stations located on HW block, the FASs due to recorded EFWs are clearly exhibiting  
322 maximum amplitudes higher than FASs due to recorded EHWs. For seismic stations located on the  
323 FW block, slightly higher amplitudes of the FASs in the high-frequency band (*i.e.* approximately  $> 3$   
324 Hz) due to recorded EHWs are observed when compared with FASs due to recorded EFWs. For  
325 seismic stations located on FZ, higher amplitudes of the FASs in the high-frequency band (*i.e.*  
326 approximately  $> 3$  Hz) due to recorded EFWs are observed when compared with FASs due to  
327 recorded EHWs.

328  
329 The generalized site spectral amplification patterns in the East Hokkaido study area are independently  
330 exhibited for seismic stations on FW (Figure 15), FZ (Figure 16), and HW (Figure 17) blocks. The  
331 behaviors of  $SSA_{OH}$  and  $SSA_{OF}$  are showing overall similar amplification patterns. This consistency  
332 in amplification patterns is obviously exhibited in Figures 15, 16, and 17 as a transition from high  
333 amplification at high frequencies to low amplification at low frequencies. This indicates that  
334 amplification due to earthquakes outside the fault zone (EFWs and EHWs) is larger than  
335 amplifications due to earthquakes inside the fault zone (EFZs) in the low-frequency band (the  
336 maximum amplifications at 0.5 Hz in the vertical components and 0.3 Hz in the EW and NS  
337 components). Conversely, at seismic stations located on FW and FZ, both behaviors of  $SSA_{HF}$  and  
338  $SSA_{FH}$  are showing a transition from high amplification at low frequencies to low amplification at  
339 high frequencies. It is noteworthy that frequencies at transition points between high amplifications  
340 and low amplifications are 3 Hz, 2 Hz, and < 1 Hz at seismic stations on FW, FZ, and HW blocks,  
341 respectively. In this paper, these frequencies would be called pivoted frequencies (*i.e.* PF). The  
342  $SSA_{FH}$  at seismic stations on the hanging wall is consistent without exhibiting PF. Table 5 is  
343 summarizing the highs and lows of the average of  $SSA_{OH}$ ,  $SSA_{OF}$ ,  $SSA_{HF}$ , and  $SSA_{FH}$  values  
344 considering the orthogonal components observed at FW, FZ, and HW blocks at the East Hokkaido  
345 study area. The high amplifications in the high-frequency bands ( $SSA_{OH}$  and  $SSA_{OF}$ ) reveal the strong  
346 role of the deep FZ effects. The low amplification in the low-frequency ( $SSA_{OH}$  and  $SSA_{OF}$ ) could be  
347 inferred to the strong role of the near- surface impedance effects of the FZ, which are obviously  
348 shown in  $SSA_{HF}$  and  $SSA_{FH}$ . The gradual increase of the low amplification through  $SSA_{OH}$ ,  $SSA_{OF}$ ,  
349 and  $SSA_{HF}$  (shown in Table 5) is reflecting the strong structural control of the HW compared with the  
350 weak role of the FW in amplifying the ground motions. For stations on the FW, the  $SSA_{OH}$  indicates

351 that the effect of EFZs in the high-frequency is similar to the effect of EHWs in the low-frequency.  
352 However, it could be concluded from the amplification factors that the influence of sources inside the  
353 fault zone (EFZs) are higher than those outside the fault zone (EFWs and EHWs) in amplifying the  
354 ground motions.

355  
356 Guided waves of fault zone could be produced due to earthquakes very close to or in the fault zone  
357 (Igel *et al.* 2002; Fohrmann *et al.*, 2004; Li and Vidale, 1996; Jahnke *et al.*, 2002). In the light of  
358 these studies, the FASs of the recorded EFZs favour the highest amplifications at stations on FW, FZ,  
359 and HW blocks in East Hokkaido study area (Figures 12, 13, and 14). Their amplification patterns  
360 ( $SSA_{OH}$ ,  $SSA_{OF}$ ,  $SSA_{HF}$ , and  $SSA_{FH}$ ) shown in Figures 15, 16, and 17 are compatible with the  
361 recent study by Wu *et al.* (2008). They observed that earthquakes inside (*i.e.* EFZs) and outside (*i.e.*  
362 EFWs and EHWs) the fault zone could produce high amplification (*i.e.* guided waves) in the near-  
363 surface fault zone. This near-surface fault zone could guide waves at low-frequency, whereas the  
364 deep part of the fault zone could guide high-frequency waves (Wu *et al.*, 2008). This frequency-  
365 dependent feature makes the guided waves dominant in the earthquake seismogram after travelling  
366 far distances. The shallow layers of the fault system in the East Hokkaido study area resemble the top  
367 part of ‘flower’ structure (Figure 5). The significance of these shallow layers (*i.e.* low-frequency  
368 waveguide) for seismic shaking hazard is considerably higher than that associated with the deep fault  
369 zone layers (*i.e.* high-frequency waveguide), because of the ability to generate motion amplification  
370 from a much broader spatial distribution of earthquakes (*i.e.* EFZs, EFWs, and EHWs in the present  
371 study) as previously concluded by Seeber *et al.* 2000. This consideration is already mentioned and  
372 indicated as the amplification due to earthquakes outside the fault zone (EFWs and EHWs) are larger  
373 than amplifications due to earthquakes inside the fault zone (EFZs) in the low-frequency band (the

374 maximum amplification at 0.5 Hz in the vertical components and 0.3 Hz in the EW and NS  
375 components). Additionally, the peculiar feature of the PF could be interpreted as the transition from  
376 PF of 3 Hz (at stations on FW correspond to high-frequency waveguide due to deep fault zone)  
377 through 2 Hz (at stations on FZ), and  $< 1$  Hz (at stations on HW correspond to low-frequency  
378 waveguide due to shallow flower fault structure). The wavelengths matching or close to the width of  
379 the fault are corresponding to these dominant frequencies. Interestingly, the peaks of the low-  
380 frequency amplification of  $SSA_{OH}$  and  $SSA_{OF}$ , particularly for seismic stations on FZ, are  
381 corresponding to frequencies of 0.5 Hz (vertical components) and 0.3 Hz (EW and NS components).  
382 Moreover, the  $P$ -wave and  $S$ -wave velocities in the FZ are approximately 5 and 3 km/s, respectively  
383 (Figure 5). Consequently, the estimated wavelengths are 10 km that approximately equalize the FZ  
384 width in the East Hokkaido study area.

385

## 386 4.2 Akita-Iwate Study Area

387 In the Akita-Iwate study area, Figures 18, 19, and 20 are showing the results of FASs for stations on  
388 l.FW, FZ (*i.e.* hanging wall blocks or upthrown sides), and r.FW blocks, respectively. The FASs of  
389 stations on l.FW and FZ, which are calculated using recorded earthquakes having their hypocenters  
390 beneath the right footwall block (Er.FWs), have the highest Fourier amplitudes in the low-frequency  
391 band (*i.e.* approximately  $< 5$  Hz). Conversely, the highest Fourier amplitudes in the high-frequency  
392 band (*i.e.* approximately  $> 5$  Hz) are prevailing in the FASs that are calculated using recorded  
393 earthquakes having their hypocenters beneath the left footwall block (El.FWs), as shown in Figures  
394 18 and 19. Seismic stations on the r.FW are exhibiting the highest Fourier amplitudes for FASs due to  
395 recorded El.FWs (Figure 20). Spectacular behavior of FASs, which are calculated using recorded

396 EFZs, could be clearly seen in all seismic stations with approximately intermediate Fourier  
397 amplitudes.

398  
399 Figure 21, Figure 22, and Figure 23 are exhibiting the site spectral amplification patterns in the Akita-  
400 Iwate study area for seismic stations on r.FW, FZ (*i.e.* hanging wall blocks), and l.FW blocks,  
401 respectively. The behavior of  $SSA_{O/l.F}$  is remarkably variant.

402  
403 At seismic stations located on r.FW, the effect of the recorded El.FWs (*i.e.* sources outside the fault  
404 zone) is higher than the recorded EFZs at all frequency bands, as depicted from  $SSA_{O/l.F}$  in Figure  
405 21. At low frequencies (*i.e.* 0.3 ~ 0.5 Hz), the behavior of  $SSA_{O/l.F}$  is showing maximum  
406 amplification factors of 2.08 and 9.37 for seismic stations on FZ and l.FW, respectively. These  
407 maximum amplification factors are reflecting the high influence of the active reverse fault system on  
408 amplifying the ground motions, particularly due to those recorded EFZs (*i.e.* sources inside the fault  
409 zone) at low frequencies (*i.e.* 0.3 ~ 0.5 Hz). Comparable maximum amplification factors from  
410  $SSA_{O/r.F}$  are 2.14, 3.28, and 2.91 at seismic stations on l.FW, FZ, r.FW blocks, respectively. The  
411 amplification pattern resulted from  $SSA_{l.F/r.F}$  at seismic stations on r.FW resembles their  
412 corresponding amplification patterns resulted from  $SSA_{O/r.F}$ . The comparison between maximum  
413 amplification factors, particularly at low-frequency of 0.25 Hz, for  $SSA_{O/r.F}$  and  $SSA_{l.F/r.F}$  is  
414 indicating the higher influence of recorded El.FWs (*i.e.* sources outside the fault zone) than those  
415 recorded EFZs (*i.e.* sources inside the fault zone) in amplifying the ground motions at all frequency  
416 bands, as depicted from Figure 21.

417

418 At seismic stations on FZ (Figure 22), the behavior of  $SSA_{O/r.F}$  is showing maximum amplification  
419 factors at frequencies  $> 10$  Hz, whereas amplification due to recorded EFZs equalizes those Er.FWs  
420 at frequencies lower than 10 Hz. The maximum amplification factors depicted by  $SSA_{O/L.F}$  at low-  
421 frequency between 0.4 and 0.5 Hz are indicating the higher influence of recorded EFZs (*i.e.* sources  
422 or earthquakes inside the fault zone) than those recorded El.FWs (*i.e.* sources or earthquakes outside  
423 the fault zone) in amplifying the ground motions. This could be related to the effect of the shallow  
424 fault zone ‘flower’ structure (Figures 6 and 7). The behavior of  $SSA_{r.F/L.F}$  resembles  $SSA_{O/r.F}$   
425 behavior, indicating the higher impact of Er.FWs than those of El.FWs in amplifying the ground  
426 motions at frequencies  $> 10$  Hz, whereas the comparable response is observed at frequencies  $< 10$  Hz.  
427

428 At seismic stations located on l.FW (Figure 23),  $SSA_{O/r.F}$  is showing a transition from high  
429 amplification of high-frequency to low amplification of low-frequency and vice versa is shown by  
430  $SSA_{O/L.F}$ . This feature is reflecting the strong influence of the near-surface fault zone (flower  
431 structure) at the low frequencies, whereas higher amplification at higher frequencies is related to the  
432 deep fault zone impact. These aforementioned transitions could be exhibited at PF of 5 Hz for EW  
433 and NS components and 7 Hz for UD component. The amplification patterns resulted from  $SSA_{r.F/L.F}$   
434 resemble their corresponding amplification patterns resulted from  $SSA_{O/L.F}$ , but exhibiting PF at 6  
435 Hz for EW and NS components and 8 Hz for UD component. The comparison between maximum  
436 amplification factors, particularly at low frequencies between 0.3 and 0.5 Hz, for  $SSA_{O/L.F}$  and  
437  $SSA_{r.F/L.F}$  is indicating the higher influence of recorded Er.FWs than those recorded EFZs in  
438 amplifying the ground motions at all frequency bands, as depicted from Figure 23.

439

440 Table 6 is summarizing the highs and lows of the averages of  $SSA_{O/LF}$ ,  $SSA_{O/r.F}$ ,  $SSA_{r.F/LF}$ , and  
441  $SSA_{L.F/r.F}$  values considering the orthogonal components observed at r.FW, FZ, and l.FW blocks at  
442 Akita-Iwate study area. It could be concluded from the amplification factors that the influence of  
443 sources or earthquakes far away from the fault zone (El.FWs and Er.FWs) are higher than those in the  
444 fault zone (EFZs) in amplifying the ground motions.

445

### 446 **4.3 Fukushima Study Area**

447 In the Fukushima study area, Figures 24 and 25 are showing the results of FASs for stations located  
448 on footwall and hanging wall blocks, respectively. Two observations are prevailing in this study area.  
449 First, FASs that are calculated using recorded EFZs have the highest Fourier amplitudes. Second, the  
450 amplitudes of FASs, which are calculated using recorded EHWs, are higher than those calculated  
451 using recorded EFWs.

452

453 Similar generalized site spectral amplification patterns in the Fukushima study area (Figure 26 and  
454 Figure 27) as previously seen in the East Hokkaido study area. At both FW and HW blocks, a  
455 transition from high amplification at high frequencies to low amplification at low frequencies is  
456 observed in the behaviors of  $SSA_{OH}$  and  $SSA_{OF}$ . The PFs are ~2 Hz and ~1 Hz at seismic stations  
457 located on FW and HW blocks, respectively. As previously discussed in the East Hokkaido and  
458 Akita-Iwate study areas, these high amplification in the high-frequency bands (> 2 Hz) reveal the  
459 strong role of the deep FZ effects, whereas the low amplification in the low-frequency bands (0.4 ~  
460 0.6 Hz) reveal the strong role of the near-surface impedance effects of the FZ. These low  
461 amplification factors are seen in both  $SSA_{OH}$  and  $SSA_{OF}$  indicates that the effect of EHWs and EFWs

462 (sources outside the fault zone) is higher than the effect of the EFZs (sources inside the fault zone) in  
463 amplifying the ground motions.

464  
465 At seismic stations on FW, the behavior of  $SSA_{HF}$  is showing general high amplification, particularly  
466 at frequencies of 0.3 ~ 0.4 Hz. The behavior of  $SSA_{FH}$  for stations on the HW is exhibiting overall  
467 low amplification with unusual high amplification seen around 1 Hz. This feature is reflecting the  
468 strong structural control of the HW compared with the weak role of the FW in amplifying the ground  
469 motions.

470  
471 Table 7 is summarizing the highs and lows of the averages of  $SSA_{OH}$ ,  $SSA_{OF}$ ,  $SSA_{HF}$ , and  $SSA_{FH}$   
472 values considering the orthogonal components observed at FW and HW blocks at the Fukushima  
473 study area. Both high and low amplifications are reflecting the strong structural role of the HW in  
474 amplifying the ground motions at the expense of the FW block. This feature is similar to the study  
475 case in the East Hokkaido area. Moreover, the effect due to the recorded EHWs and EFWs is higher  
476 than those of the recorded EFZs in amplifying the ground motions at low frequencies and vice versa  
477 at high frequencies.

478  
479 Although the non-presence of clear and well-developed low-velocity fault zone as depicted in Figures  
480 8 and 9, the amplification patterns are comparable to those observed in the East Hokkaido study area.

481

#### 482 **4.4 HVSR and SBSR**

483 Figure 28 is showing examples of HVSRs at different K-NET and KiK-net seismic stations in the  
484 three present study areas. Figure 29 is showing examples of SBSRs at different KiK-net seismic

485 stations. These examples are generalizing the overall results from those HVSRs and SBSRs in the  
486 three present study areas. It is obvious that there are no significant responses that could be interpreted  
487 as the effect of strong structural control due to active reserve faults, which is contradicted to previous  
488 work by Rigano *et al.* (2008) who concluded good HVSR results on the surface of faults through  
489 testing the reliability of HVSR.

490  
491 The effect of the fault zone in the three study areas could not be captured in the SBSRs. This is  
492 because the SBSRs eliminate the source and the propagation path effects completely. As a result,  
493 variation in amplitude or frequency due to the presence of fault zone would not be exhibited in the  
494 processed SBSRs.

495  
496 Pischiutta *et al.* (2015) concluded that fault zone could cause high amplification normal to this fault  
497 zone, which is called directional amplification. In the afore depicted Figures 15, 16, 17, 21, 22, 23,  
498 26, and 27, comparable behaviors of SSAs of the horizontal components is concluded, which conflict  
499 with previous study of Pischiutta *et al.* (2015). The behaviors of SSAs in the EW components are  
500 similar to those in the NS components, through the active fault system in the present study areas are  
501 trending NS. This questionable feature could be inferred to the strong structural prevalence  
502 amplification due to active fault zone guided waves on both the horizontal and vertical components.  
503 Another reason for this feature could be related to the negligible horizontal heterogeneities in the  
504 subsurface.

505

506

507

## 508 4.5 EHVSR Inversion

509 In each study area, two seismic stations on each block (FW, FZ, and HW) are selected to run EHVSR  
510 inversion. However, the different three tectonic patterns in the present study are summarized in  
511 Figure 30 accompanying the resulted maximum averages of SSAs at high and low frequencies  
512 deduced from stations on each block.

513  
514 Figure 31 is showing three examples of inverted EHVSR curves superimposed with their  
515 corresponding observed HVSR curves. Reasonable fitting between the observed and the inverted  
516 EHVSR curves could be achieved. Smoothing technique is not applied; instead the EHVSR curves  
517 are used without smoothing in order to capture all the available information in the HVSR curves.  
518 Consequently, the resulted velocity structures are well recognized for the subsurface structure.

519  
520 Reduced *P*-wave and *S*-wave velocity structures with respect to the surrounding fault blocks (*i.e.* FW,  
521 HW, r.FW, or l.FW) are concluded as inverted from stations on the fault zone system in the East  
522 Hokkaido study area (Figure 32). This reduction extends to ~8 km depth, which indicates the fault  
523 depth existence. Similar velocity reduction is concluded in the Akita-Iwate study area (Figure 33), but  
524 this reduction extends to ~2.5 km depth, which indicates shallow fault system. In the Fukushima  
525 study area, there is no station lying on the fault zone, but FKS007 K-NET station is the closest station  
526 to the fault system in this study area. Remarkably, deep fault system of ~ 8 km depth is concluded in  
527 the Fukushima study area (Figure 34).

528  
529 It is hoped that the present inversion could link these concluded inverted velocity structures with the  
530 frequency-dependent behavior of the different amplification patterns in the three present study areas.

531 As a result, these different amplification patterns reflect the efficiency of the variation of guided  
532 waves with fault system depth. Clarifying the important role of this low-velocity fault zone in the  
533 interpretation of the resulted amplification patterns will require multidisciplinary research works  
534 joining microtremor field studies across these fault systems, two- and three-dimension calculations -  
535 taking into account basins, sedimentary covers, and other topographic effects associated with fault  
536 zones in the near-surface -, measurements in deep boreholes inside and outside fault zones, and other  
537 geophysical studies. Although they are essential, these fuller treatment studies are highly likely  
538 beyond the scope of the present conclusions.

539

## 540 **5. Conclusion**

541 This study has originated from the observation of systematic larger amplitudes of ground motion  
542 spectra at K-NET and KiK-net seismic stations at three different localities in Japan because of the  
543 presence of active faults (AIST, 2012 and 2013). Those north-south active faults have different  
544 degrees of complexity for characterizing fault zones. They could be categorized as 1) low-velocity  
545 active reverse faults (East Hokkaido area), 2) system of active reverse faults (set of several en-  
546 echelon fault traces) composing horst fault system (Akita-Iwate area), and 3) complex active fault  
547 zone that includes vertical strike-slip and reverse faults (Fukushima area). These active reverse fault  
548 zones could produce local amplification not only on these active faults but also far away from these  
549 faults (*i.e.* footwall and hanging wall blocks). Analyzing site response related to these fault zones  
550 using FAS is most effective than using HVSR or SBSR at the present study areas.

551

552 Comparable SSAs at seismic stations on fault zone and far away from the fault zone are resulted at  
553 high frequencies due to sources or earthquakes inside the active fault zones. At low frequencies,

554 sources inside the active fault zones could favor higher SSAs at stations on FW and l.FW in  
555 Fukushima and Akita-Iwate study areas, respectively, than at stations on HW, FZ, and r.FW in both  
556 study areas. In the study area of East Hokkaido, observed amplification could not be produced due to  
557 sources inside the active fault zones at low frequencies. In East Hokkaido and Fukushima study areas,  
558 sources outside the fault zone could not produce significant SSAs at high frequencies, whereas  
559 remarkable high SSAs at low frequencies with a gradual increase from stations on HWs through FZs  
560 and FWs. The stations on r.FW and l.FW in Akita-Iwate study area exhibit similar SSAs due to  
561 sources outside the fault zone at low frequencies, whereas stations on the FZ (*i.e.* HWs) are exhibiting  
562 high SSAs at high frequencies.

563  
564 The observed amplification patterns on FW, FZ, and HW are strongly related to the corresponding  
565 tectonic pattern (*i.e.* tectonic-specific pattern) and the frequency bands. The near-surface (*i.e.* low-  
566 velocity layers forming flower structure) fault zone could produce low-frequency amplification,  
567 whereas high-frequency amplification is inferred to the fault zone in depth. Interestingly, the peaks of  
568 the low-frequency amplification are corresponding to wavelengths approximately equalize fault  
569 zone's width, particularly in the East Hokkaido and Akita-Iwate study areas.

570  
571 Using HVSR is not effective in the present study areas, which is contradicted to previous work by  
572 Rigano *et al.* (2008) who concluded good HVSR results on the surface of faults through testing the  
573 reliability of HVSR. Additionally, the observed horizontal components are showing comparable  
574 amplification patterns. This peculiar feature indicates the strong structural prevalence amplification  
575 due to active fault zone guided waves as exhibited in all motion components (horizontal and vertical).  
576

577 **Acknowledgements**

578 The author is highly appreciated and grateful to the National Research Institute for Earth Science and Disaster  
579 prevention (NIED) for making the valuable KiK-net and K-NET data available (DOI : 10.17598/NIED.0004).

580 The author would appreciate and acknowledge providing the EHVSr inversion code by Prof. Fumiaki  
581 Nagashima (DPRI, Kyoto University). The author would appreciate and acknowledge the generous, valuable,  
582 and constructive comments and suggestions from the Editor and the reviewers.

583

584 **DECLARATIONS**

585 **Funding**

586 The author states that this research work is not supported by any fund and no fund is received.

587 **Conflicts of interest/Competing interests**

588 The author states that there are no any conflicts of interests or competing interests

589 **Availability of data and material**

590 Any data in this research work would be available upon request immediately.

591 **Code availability**

592 Any software application or custom code in this research work would be available upon request immediately.

593 **Authors' contributions**

594 The submitting author confirm that he is a single author named in the manuscript is aware of the submission  
595 and has agreed for the paper to be submitted to Natural Hazards. I am acknowledging the consent  
596 requirements. I am very appreciated for your careful consideration.

597 **References**

- 598 Abdelwahed M F, Zhao D (2007) Deep structure of the Japan subduction zone. *Phys. Earth Planet. Inter.* 162: 32-52.
- 599 AIST (National Institute of Advanced Industrial Science and Technology. Active Fault Database of Japan), February 28,  
600 2012 version. Research Information Database DB095, National Institute of Advanced Industrial Science and Technology.  
601 Geological Survey of Japan [https://gbank.gsj.jp/activefault/index\\_e\\_gmap.html](https://gbank.gsj.jp/activefault/index_e_gmap.html)
- 602 AIST (National Institute of Advanced Industrial Science and Technology, Active Fault Database of Japan), July 23, 2013  
603 Version. Research Information Database DB095, National Institute of Advanced Industrial Science and Technology  
604 [https://gbank.gsj.jp/activefault/index\\_e\\_gmap.html](https://gbank.gsj.jp/activefault/index_e_gmap.html)
- 605 Ben-Zion Y (1998) Properties of seismic fault zone waves and their utility for imaging low-velocity structure. *J. geophys.*  
606 *Res.* 103(12): 567–585.
- 607 Ben-Zion Y, Aki K (1990) Seismic radiation from an SH line source in a laterally heterogeneous planar fault zone. *Bull.*  
608 *seism. Soc. Am.* 80: 971–994.
- 609 Ben-Zion Y, Sammis C G (2003) Characterization of fault zones. *Pure appl. Geophys.* 160: 677–715.
- 610 Ben-Zion Y, Peng Z, Okaya D, Seeber L, Armbruster J G, Ozer N, Michael A J, Baris S, Aktar M (2003) A shallow fault-  
611 zone structure illuminated by trapped waves in the Karadere–Duzce branch of the North Anatolian Fault, western Turkey.  
612 *Geophys. J. Int.* 152: 699–717.
- 613 Ben-Zion, Y. *et al.*, 2015. Basic data features and results from a spatially dense seismic array on the San Jacinto fault  
614 zone, *Geophys. J. Int.*, 202, 370–380.
- 615 Borchardt RD, (1970) Effects of local geology on ground motion near San Francisco Bay. *Bull. seism. Soc. Am.* 60(1):  
616 29–61.
- 617 Borchardt RD (1994) Estimates of site-dependent response spectra for design (methodology and justification). *Earthq*  
618 *Spectra* 10(4): 617–653.

619 Burjánek, J., Moore, J.R., Yugsi-Molina, F.X., Fäh, D., 2012. Instrumental evidence of normal mode rock slope vibration.  
620 *Geophys. J. Int.* 188 (2), 559–569. <https://doi.org/10.1111/j.1365-246X.2011.05272.x>.

621 Cormier V F, Spudich P (1984) Amplification of ground motion and waveform complexity in fault zones: Examples from  
622 the San Andreas and Calaveras faults. *Geophys. J. R. astron. Soc.* 79: 135–152.

623 Di Giulio, G., F. Cara, A. Rovelli, G. Lombardo, and R. Rigano (2009), Evidences for strong directional resonances in  
624 intensely deformed zones of the Pernicana fault, Mount Etna, Italy, *J. Geophys. Res.*, 114, B10308,  
625 doi:10.1029/2009JB006393

626 Fohrmann M, Igel H, Jahnke G, Ben-Zion Y (2004) Guided waves from sources outside faults: an indication for shallow  
627 fault zone structure?. *Pure Appl. Geophys.* 161: 2125–2137.

628 Hickman S H, Zoback M D, Ellsworth W L (2005) Structure and composition of the San Andreas Fault zone at Parkfield:  
629 Initial results from SAFOD Phase 1 and 2. *EOS, Trans. Am. geophys. Un.* 83(47): 237.

630 Igel H, Ben-Zion Y, Leary P (1997) Simulation of *SH* and *P-SV* wave propagation in fault zones. *Geophys. J. Int.* 128:  
631 533–546.

632 Igel H, Jahnke G, Ben-Zion Y (2002) Numerical simulation of fault zone guided waves: accuracy and 3-D effects. *Pure*  
633 *Appl. Geophys.* 159: 2067–2083.

634 Jahnke G, Igel H, Ben-Zion Y (2002) Three-dimensional calculations of fault zone guided waves in various irregular  
635 structures. *Geophys. J. Int.* 151: 416–426.

636 Kakhki, M.K., Peters, F.C., Mansur, W.J., SadidKhoii, A., Rezaei, S., 2020. Deciphering site response directivity in  
637 landslide-prone slopes from ambient noise spectral analysis. *Eng. Geol.* 269, 105542  
638 <https://doi.org/10.1016/j.enggeo.2020.105542>.

639 Kato A, Sakai S, Hirata N, Kurashimo E, Iidaka T, Iwasaki T, Kanazawa T (2006) Imaging the seismic structure and  
640 stress field in the source region of the 2004 mid-Niigata prefecture earthquake: Structural zones of weakness and  
641 seismogenic stress concentration by ductile flow. *J. Geophys. Res.* 111: B08308. doi:10.1029/2005JB004016.

642 Korneev V A, Nadeau R M, McEvilly T V (2003) Seismological studies at Parkfield IX: fault-zone imaging using guided  
643 wave attenuation. *Bull. seism. Soc. Am.* 93: 1415–1426.

644 Lermo J, Chavez-Garcia FJ (1993) Site effect evaluation using spectral ratios with only one station. *Bull. seism. Soc. Am.*  
645 83(5):1574–94.

646 Lewis M A, Peng Z, Ben-Zion Y, Vernon F L (2005) Shallow seismic trapping structure in the San Jacinto fault zone near  
647 Anza, California. *Geophys. J. Int.* 162: 867–881. doi:10.1111/j.1365-246X.2005.02684.x.

648 Li Y G, Leary P C (1990) Fault-zone trapped seismic waves. *Bull. seism. Soc. Am.* 80: 1245–1271.

649 Li Y G, Leary P C, Aki K, Malin P (1990) Seismic trapped modes in the Orville and San Andreas Fault zones. *Science*  
650 249: 763–766.

651 Li Y G, Aki K, Adams D, Hasemi A, Lee W H K (1994) Seismic guided waves trapped in the fault zone of the Landers,  
652 California, earthquake of 1992. *J. geophys. Res.* 99: 11705–11722.

653 Li Y G, Ellsworth W L, Thurber C H, Malin P E, Aki K (1997) Fault zone guided waves from explosions in the San  
654 Andreas fault at Parkfield and Cienega Valley, California. *Bull. seism. Soc. Am.* 87: 210–221.

655 Li Y G, Vernon F L (2001) Characterization of the San Jacinto fault zone near Anza, California, by fault zone trapped  
656 waves. *J. geophys. Res.-Solid Earth* 106(30): 671–688.

657 Li Y G, Vidale J E, Aki K, Xu F (2000) Depth-dependent structure of the Landers fault zone from trapped waves  
658 generated by aftershocks. *J. geophys. Res.-Solid Earth* 105: 6237–6254.

659 Li Y G, Vidale J E (1996) Low-velocity fault-zone guided waves: numerical investigations of trapping efficiency. *Bull.*  
660 *seism. Soc. Am.* 86: 371–378.

661 Li Y G, Vidale J E, Cochran E S (2004) Low-velocity damaged structure of the San Andreas fault at Parkfield from fault  
662 zone trapped waves. *Geophys. Res. Lett.* 31: 2165, doi:10.1029/2001JB001456.

663 Matsubara M, Obara K, Kasahara K (2008) Three-dimensional P- and S-velocity structures beneath the Japan Islands  
664 obtained by high-density seismic stations by seismic tomography. *Tectonophysics* 454: 86-103.  
665 doi:10.1016/j.tecto.2008.04.016

666 Matsubara M, Obara K (2011) The 2011 Off the Pacific coast of Tohoku earthquake related to a strong velocity gradient  
667 with the Pacific plate. *Earth Planets Space* 63: 663-667. doi:10.5047/eps.2011.05.018.

668 Michael A J, Ben-Zion Y (1998) Inverting fault zone trapped waves with genetic algorithm. *EOS, Trans. Am. geophys.*  
669 *Un.* 79: F584.

670 Mizuno T, Nishigami K, Ito H, Kuwahara Y (2004) Deep structure of the Mozumi-Sukenobu fault, Central Japan,  
671 estimated from the subsurface array observation of fault zone trapped waves. *Geophys. J. Int.* 159: 622– 642.

672 Mizuno T, Nishigami K (2006) Deep structure of the Nojima Fault, southwest Japan, estimated from borehole  
673 observations of fault-zone trapped waves. *Tectonophysics* 417: 231–247.

674 Mooney W D, Ginzburg A (1986) Seismic measurements of the internal property of fault zone. *Pure appl. Geophys.* 124:  
675 141–157.

676 Nagashima F, Matsushima S, Kawase H, Sánchez-Sesma FJ, Hayakawa T, Satoh T, Oshima M (2014) Application of  
677 horizontal-to-vertical (H/V) spectral ratios of earthquake ground motions to identify subsurface structures at and around  
678 the K-NET site in Tohoku, Japan. *Bull. seism. Soc. Am.* 104: 2288–2302. <https://doi.org/10.1785/0120130219>

679 Nagashima F, Kawase H, Matsushima S (2017) Estimation of horizontal seismic bedrock motion from vertical surface  
680 motion based on horizontal-to-vertical spectral ratios of earthquake motions. In: 16th world conference on earthquake  
681 engineering, No. 3685, 9–13 Jan 2017, Santiago

682 Nakajima J, Hasegawa A (2007a) Deep crustal structure along the Niigata-Kobe Tectonic Zone, Japan: Its origin and  
683 segmentation. *Earth, Planets and Space* 59: e5-e8.

684 Nakajima J, Hasegawa A (2007b) Tomographic evidence for the mantle upwelling beneath southwestern Japan and its  
685 implications for arc magmatism. *Earth and Planetary Science Letters* 254: 90-105.

686 Nakajima J, Hasegawa A (2007c) Subduction of the Philippine Sea plate beneath southwestern Japan: Slab geometry and  
687 its relationship to arc magmatism. *J. Geophys. Res.* 112: B08306. doi:10.1029/2006JB004770

688 Nakajima J, Matsuzawa T, Hasegawa A, Zhao D (2001) Three-dimensional structure of Vp, Vs, and Vp/Vs beneath  
689 northeastern Japan: Implications for arc magmatism and fluids. *J. Geophys. Res.* 106(21); 843-857.

690 Nakamura Y (1989) A method for dynamic characteristics estimations of subsurface using microtremors on the ground  
691 surface. *Q Rep RTRI Jpn* 30: 25–33.

692 Nakamura Y (2000) Clear identification of fundamental idea of Nakamura's technique and its application. Proceedings of  
693 the XII World Conf. Earthq. Engrg., Auckland, New Zealand, 8 pp.

694 Nakamura M, Yoshida Y, Zhao D, Takayama H, Obana K, Katao H, Kasahara J, Kanazawa T, Kodaira S, Sato T,  
695 Shiobara H, Shinohara M, Shimamura H, Takahashi N, Nakanishi A, Hino R, Murai Y, Mochizuki K (2008) Three-  
696 dimensional P- and S-wave velocity structures beneath Japan. *Phys. Earth Planet. Inter.* 168: 49-70.  
697 doi:10.1016/j.pepi.2008.04.017.

698 Nishida K, Kawakatsu H, Obara K (2008) Three-dimensional crustal S wave velocity structure in Japan using  
699 microseismic data recorded by Hi-net tiltmeters. *J. Geophys. Res.* 113: B10302. doi:10.1029/2007JB005395.

700 Nogoshi M, Igarashi T (1970) On the propagation characteristics estimations of subsurface using microtremors on the  
701 ground surface. *J Seismol Soc Jpn* 23: 264– 280.

702 Nogoshi M, Igarashi T (1971) On the amplitude characteristics of microtremor (Part 2). *J Seismol Soc Jpn* 24: 26–40.

703 Panzera, F., Pischiutta, M., Lombardo, G., Monaco, C., Rovelli, A., 2014. Wavefield polarization in fault zones of the  
704 western flank of Mt. Etna: observations and fracture orientation modelling. *Pure Appl. Geophys.* 171, 3083–3097.  
705 <https://doi.org/10.1007/s00024-014-0831-x>.

706 Panzera, F., Lombardo, G., Monaco, C., 2016a. New evidence of wavefield polarization on fault zone in the lower NE  
707 slope of Mt. Etna. *Ital. J. Geosci.* 135 (2), 250–260. <https://doi.org/10.3301/IJG.2015.22>.

708 Panzera, F., Lombardo, G., Sicali, S., D'Amico, S., 2016b. Surface geology and morphologic effects on seismic site  
709 response: the study case of Lampedusa, Italy. *Phys. Chem. Earth Parts A/B/C* 98, 62–72.  
710 <https://doi.org/10.1016/j.pce.2016.08.006>.

711 Panzera, F., Halldorsson, B., Vogfjörð, K., 2017a. Directional effects of tectonic fractures on ground motion site  
712 amplification from earthquake and ambient noise data: a case study in South Iceland. *Soil Dyn. Earthq. Eng.* 97, 143–154.  
713 <https://doi.org/10.1016/j.soildyn.2017.03.024>.

714 Panzera, F., Lombardo, G., Longo, E., Langer, H., Branca, S., Azzaro, R., Cicala, V., Trimarchi, F., 2017b. Exploratory  
715 seismic site response surveys in a complex geologic area: a case study from Mt. Etna volcano (southern Italy). *Nat.*  
716 *Hazards* 86, 385–399. <https://doi.org/10.1007/s11069-016-2517-4>.

717 Panzera, F., D'Amico, S., Colica, E., Viccaro, M., 2019. Ambient vibration measurements to support morphometric  
718 analysis of a pyroclastic cone. *Bull. Volcanol.* 81 (12), 74. <https://doi.org/10.1007/s00445-019-1338-1>.

719 Panzera F, Tortorici G, Romagnoli G, Marletta G, Catalano S (2020) Empirical evidence of orthogonal relationship  
720 between directional site effects and fracture azimuths in an active fault zone: The case of the Mt. Etna lower eastern flank.  
721 *Engineering Geology* 279 (2020) 105900, <https://doi.org/10.1016/j.enggeo.2020.105900>

722 Peng Z, Ben-Zion Y, Zhu L, Michael A J (2003) Inference of a shallow fault zone layer in the rupture zone of the 1992.  
723 Landers, California earthquake from locations of events generating trapped waves and travel time analysis. *Geophys. J. Int.*  
724 155: 1021–1041.

725 Peruzza, L., Azzaro, R., Gee, R., D'Amico, S., Langer, H., Lombardo, G., Pace, B., Pagani, M., Panzera, F., Ordaz, M.,  
726 Suarez, M.L., Tusa, G., 2017. When probabilistic seismic hazard climbs volcanoes: the Mt. Etna case, Italy – part 2:  
727 Computational implementation and first results. *Nat. Hazards Earth Syst. Sci.* 17, 1999–2015.  
728 <https://doi.org/10.5194/nhess-17-1999-2017>.

729 Pischietta, M., Salvini, F., Fletcher, J.B., Rovelli, A., Ben-Zion, Y., 2012. Horizontal polarization of ground motion in the  
730 Hayward fault zone at Fremont, California: dominant fault-high-angle polarization and fault-induced cracks. *Geophys. J.*  
731 *Int.* 188 (3), 1255–1272. <https://doi.org/10.1111/j.1365-246X.2011.05319.x>.

732 Pischiutta, M., Rovelli, A., Salvini, F., Di Giulio, G., Ben-Zion, Y., 2013. Directional resonance variations across the  
733 Pernicana fault, Mt. Etna, in relation to brittle deformation fields. *Geophys. J. Int.* 193 (2), 986–996.  
734 <https://doi.org/10.1093/gji/ggt031>.

735 Pischiutta M, Savage M K, Holt R A, Salvini F (2015) Fracture-related wavefield polarization and seismic anisotropy  
736 across the Greendale Fault. *J. Geophys. Res. Solid Earth* 120: 7048–7067. doi:10.1002/2014JB011560.

737 Pischiutta, M., Fondriest, M., Demurtas, M., Magnoni, F., Di Toro, G., Rovelli, A., 2017. Structural control on the  
738 directional amplification of seismic noise (Campo Imperatore, Central Italy). *Earth Planet. Sci. Lett.* 471, 10–18.  
739 <https://doi.org/10.1016/j.epsl.2017.04.017>.

740 Rigano R, Cara F, Lombardo G, Rovelli A (2008) Evidence of ground motion polarization on fault zones of Mount Etna  
741 volcano. *J Geophys Res.* 113: B10306. [http:// dx.doi.org/10.1029/2007JB005574](http://dx.doi.org/10.1029/2007JB005574).

742 Rovelli A, Caserta A, Marra F, Ruggiero V (2002) Can seismic waves be trapped inside an inactive fault zone? The case  
743 study of Nocera Umbra, central Italy. *Bull. seism. Soc. Am.* 92: 2217–2232.

744 Roux, P., Moreau, L., Lecointre, A., Hillers, G., Campillo, M., Ben-Zion, Y., Zigone, D., Vernon, F., 2016. A  
745 methodological approach toward high-resolution surface wave imaging of the San Jacinto Fault Zone using ambient-noise  
746 recordings at a spatially dense array. *Geophys. J. Int.* 206 (2), 980–992. <http://dx.doi.org/10.1093/gji/ggw193>.

747 Seeber L, Armbruster J G, Ozer N, Aktar M, Baris S, Okaya D, Ben-Zion Y, Field E (2000) The 1999 Earthquake  
748 Sequence along the North Anatolia Transform at the Juncture between the Two Main Ruptures, in The 1999 Izmit &  
749 Duzce Earthquakes: preliminary results. edit. Barka A., O. Kazaci, S. Akyuz & E. Altunel, Istanbul technical university,  
750 209-223.

751 Seekins LC, Wennerberg L, Marghereti L, Liu HP (1996) Site amplification at five locations in San Fransico, California:  
752 a comparison of S waves, codas, and microtremors. *Bull. seism. Soc. Am.* 86(3): 627–35.

753 SESAME (2004) Guidelines for the implementation of the H/V spectral ratio technique on ambient vibrations:  
754 Measurements, processing and interpretation, SESAME (Site Effects Assessment Using Ambient Excitations. EC-RGD,  
755 Project No. EVG1-CT-2000-00026 SESAME), European Research Project WP12, deliverable D23.12, at [http://sesame-](http://sesame-fp5.obs.ujfgrenoble.fr/Deliverables)  
756 [fp5.obs.ujfgrenoble.fr/Deliverables](http://sesame-fp5.obs.ujfgrenoble.fr/Deliverables) 2004

757 Spudich, P., Hellweg, M., Lee, H.K., 1996. Directional topographic site response at Tarzana observed in aftershocks of  
758 the 1994 North-ridge, California, earthquake: implications for mainshock motions. *Bull. Seismol. Soc. Am.* 86, S193–  
759 S208.

760 Thabet M, Nemoto H, Nakagawa K (2008a) Variation process in stiffness inferred by nonlinear inversion during  
761 mainshocks at Kushiro Port vertical array site. *Earth Planet Sp* 60: 581–589. <https://doi.org/10.1186/BF03353121>

762 Thabet M (June, 2008b) Variation Process in Stiffness of Liquefiable Subsurface Layer Caused by Large Earthquake –  
763 Application to Vertical Array Sites of Port Island in Kobe and Kushiro Port in Hokkaido, Japan-. Doctor Dissertation.  
764 Osaka City University. (PDF, researchgate.net)

765 Thabet M (2019) Site-Specific Relationships between Bedrock Depth and HVSR Fundamental Resonance Frequency  
766 Using KiK-NET Data from Japan. *Pure Appl. Geophys.* 176: 4809–4831. <https://doi.org/10.1007/s00024-019-02256-7>

767 Thabet M (2021) Nonlinearity evaluation considering the uncertainty of *S*-wave velocity based on total stress analyses and  
768 diffuse field assumption: the  $M_w$  9.1 great Tohoku Taiheiyō-Oki earthquake at 05:46 UTC on 11 March 2011. *J Seismol.*  
769 <https://doi.org/10.1007/s10950-020-09974-9>

770 Thurber C H (1983) Earthquake locations and three-dimensional crustal structure in the Coyote Lake area, central  
771 California. *J. geophys. Res.* 88: 8226–8236.

772 Togo M (2000) Geomorphological Analysis on Surface Ruptures by Reverse Faulting. 206 pp. Kokon. Tokyo.

773 Villani, F., D’Amico, S., Panzera, F., Vassallo, M., Bozionelos, G., Farrugia, D., Galea, P., 2018. Shallow high-resolution  
774 geophysical investigation along the western segment of the Victoria Lines Fault (island of Malta). *Tectonophysics* 724–  
775 725, 220–233. <https://doi.org/10.1016/j.tecto.2018.01.010>.

776 Tortorici, G., Romagnoli, G., Grassi, S., Imposa, S., Lombardo, G., Panzera, F., Catalano, S., 2019. Quaternary negative  
777 tectonic inversion along the Sibillini Mts. Thrust zone: the Arquata del Tronto case history (Central Italy). *Environ. Earth*  
778 *Sci.* 78 (1), 37. <https://doi.org/10.1007/s12665-018-8021-2>.

779 Wathelet M (2005) Array Recordings of Ambient Vibrations: Surface-Wave Inversion. Ph.D. thesis, Liège University,  
780 Belgium.

781 Wu J, Hole J A, Snoko J A, Imhof M G (2008) Depth extent of the fault-zone seismic waveguide: effects of increasing  
 782 velocity with depth. *Geophys. J. Int.* 173: 611–622. doi: 10.1111/j.1365-246X.2008.03755.x

783 Zhao D, Kanamori H, Negishi H, Wiens D (1996) Tomography of the source area of the 1995 Kobe earthquake:  
 784 Evidence for fluids at the hypocenter?. *Science* 274: 1891-1894.

785

786

787

788 Table 1: Characteristics of the behavioral segments of the East Hokkaido active reverse faults  
 789 (AIST 2012, 2013).

Symbol	<b>a</b>	<b>b</b>	<b>c</b>	<b>d</b>
Name	Shihoro	Otofuke	Tobetsugawa	Kochien
Description	N-S trending east-dipping reverse fault along the eastern margin of the Tokachi Plain in central Hokkaido	N-S trending east-dipping reverse fault along the eastern margin of the Tokachi Plain in central Hokkaido	N-S trending east-dipping reverse fault along the eastern margin of the Tokachi Plain in central Hokkaido	NW-SE trending northeast-dipping reverse fault along the eastern margin of the Hidaka mountains in central Hokkaido
Trend	10°	0°	0°	330°
Dip	30° E	30° E	30° E	45° E
Length	62 Km	18 Km	40 Km	26 Km
Sense of faulting	Reverse	Reverse	Reverse	Reverse
Upthrown side	East	East	East	East
Slip rate	0.4 m/K years	0.0 m/K years	0.3 m/K years	0.1 m/K years
Slip per Event	7.2 m		4.7 m	3.0 m
Recurrence Interval	18000 years	-----	16000 years	24000 years
Elapsed time rate	-----	-----	-----	0.68
Rupture Probability in next 30 years	0.2 %	-----	0.2 %	0.1 %

790

791

792

793

794

795

796

797

798 Table 2: Characteristics of the behavioral segments of the Akita-Iwate active reverse faults (AIST 2012, 2013).

Symbol	a	b	c	d	e	f	g	h	i	j
Name	Ukai	Hanamaki	Kitakami-nishi	Shizukuishibonchi-seien	Kawafune	Warikurayama	Tazawakotoho	Senya	Kanazawa	Omoriyama
Description	N-S trending west-dipping reverse fault along the western margin of the Kitakami Basin in northern Honshu	N-S trending west-dipping reverse fault along the western margin of the Kitakami Basin in northern Honshu	N-S trending west-dipping reverse fault along the western margin of the Kitakami Basin in northern Honshu	N-S trending west-dipping reverse fault along the western margin of the Shizukuishi Basin in northern Honshu	NNE-SSW trending west-dipping reverse fault along the eastern margin of the Mahiru Mountains in northern Honshu, ruptured during the 1896 Rikuu earthquake	N-S trending west-dipping reverse fault along the eastern margin of the Mahiru Mountains in northern Honshu	N-S trending east-dipping reverse fault along the eastern shore of Lake Tazawa in northern Honshu, partly ruptured during 1896 Rikuu earthquake	N-S trending east-dipping reverse fault along the eastern margin of the Yokote Basin in northern Honshu, ruptured during the 1896 Rikuu earthquake	N-S trending east-dipping reverse fault along the eastern margin of the Yokote Basin in northern Honshu	N-S trending east-dipping reverse fault along the eastern margin of the Yokote Basin in northern Honshu
Trend	10°	10°	350°	10°	20°	0°	0°	10°	0°	350°
Dip	45° W	45° W	45° W	45° W	45° W	45° W	45° E	30°E	45° E	45° E
Length	11 Km	42 Km	27 Km	21 Km	24 Km	17 Km	10 Km	24 Km	17 Km	23 Km
Sense of faulting	Reverse	Reverse	Reverse	Reverse	Reverse	Reverse	Reverse	Reverse	Reverse	Reverse
Uplifted side	West	West	West	West	West	West	East	East	East	East
Slip rate	0.0 m/K years	0.6 m/K years	0.2 m/K years	0.6 m/K years	0.1 m/K years	0.0 m/K years	0.3 m/K years	0.8 m/K years	0.3 m/K years	0.2 m/K years
Slip per Event	-----	4.9 m	3.1 m	2.4 m	2.2 m	-----	1.2 m	2.9 m	2.0 m	2.7 m
Recurrence Interval	-----	8200 years	13000 years	4300 years	22000 years	-----	3900 years	3700 years	6700 years	16000 years
Elapsed time rate	-----	0.51	-----	0.41	0.0	-----	-----	0.03	-----	-----
Rupture Probability in next 30 years	-----	0.4 %	0.2 %	0.7 %	0.1 %	-----	0.8 %	0.8 %	0.5 %	0.2 %

799

800  
801  
802  
803  
804  
805  
806  
807  
808

Table 2: Cont.

Symbol	<b>k</b>	<b>l</b>	<b>m</b>	<b>n</b>
Name	Takinosawa	Nakacho	Toridame	Kitayuri
Description	N-S trending west-dipping reverse fault in northern Honshu	NNE-SSW trending west-dipping reverse fault in northern Honshu	N-S trending east-dipping reverse fault in northern Honshu	N-S trending east-dipping reverse fault along the western offshore of northern Honshu
Trend	0°	20°	0°	0°
Dip	45° W	45° W	45° E	45° E
Length	18 Km	9 Km	11 Km	29 Km
Sense of faulting	Reverse	Reverse	Reverse	Reverse
Upthrown side	West	West	East	East
Slip rate	0.0 m/K years	0.1 m/K years	0.0 m/K years	0.9 m/K years
Slip per Event	-----	-----	-----	3.4 m
Recurrence Interval	-----	-----	-----	3600 years
Elapsed time rate	-----	-----	-----	0.41
Rupture Probability in next 30 years	-----	-----	-----	0.8 %

809  
810  
811  
812  
813  
814

815  
816

Table 3: Characteristics of the behavioral segments of the Fukushima active reverse faults (AIST 2012, 2013).

Symbol	<b>a</b>	<b>b</b>	<b>c</b>	<b>d</b>
Name	Watari	Haramachi	Namie	Sangunmori
Description	N-S trending west-dipping reverse fault along the eastern margin of the Abukuma Mountains in northern Honshu	N-S trending left-lateral strike-slip fault with west-side-up vertical displacement along the eastern margin of the Abukuma Mountains in northern Honshu	N-S trending west-dipping reverse fault along the eastern margin of the Abukuma Mountains in northern Honshu	N-S trending left-lateral strike-slip fault with east-side-up vertical displacement in the Abukuma Mountains, northern Honshu
Trend	350°	350°	350°	0°
Dip	80° W	90° V	80° W	90° V
Length	21 Km	21 Km	53 Km	15 Km
Sense of faulting	Reverse	L-lateral	Reverse	L-lateral
Upthrown side	West	West	West	East
Slip rate	0.1 m/K years	0.1 m/K years	0.0 m/K years	0.1 m/K years
Slip per Event	2.4 m	1.5 m	-----	1.7 m
Recurrence Interval	24000 years	10000 years	-----	17000 years
Elapsed time rate	-----	0.20	-----	-----
Rupture Probability in next 30 years	0.1 %	0.3 %	-----	0.2 %

817  
818  
819  
820  
821  
822  
823  
824  
825  
826  
827  
828

829 Table 4: Detailed numbers of seismic stations and recorded earthquakes at the three study areas.

		East Hokkaido		Fukushima			Akita-Iwate	
		K-NET	KiK-net	K-NET	KiK-net		K-NET	KiK-net
FW	Sta.	5	5	4	2	r.FW	16	11
	Eq.	2925		6618			6081	
FZ	Sta.	3	2	---	---	FZ (Upthrown side)	5	6
	Eq.	643		102			3114	
HW	Sta.	17	10	14	8	l.FW	10	8
	Eq.	5806		570			573	

830 (Note: Sta. is station, Eq. is earthquake, FW is footwall block, FZ is fault zone, HW is hanging wall block, and r.FW  
831 and l.FW are right and left footwall blocks, respectively)

832

833

834

835

836

837

838 Table 5: Summary of highs and lows of site spectral amplifications in the East Hokkaido study  
839 area deduced from Figures 22, 23, and 24.

			SSA <sub>OH</sub>	SSA <sub>OF</sub>	SSA <sub>HF</sub>	SSA <sub>FH</sub>
Footwall	EW	H.	2.98	2.68	5.39	---
		L.	0.29	0.45	0.86	---
	NS	H.	3.15	3.15	4.05	---
		L.	0.35	0.57	0.89	---
	UD	H.	3.17	2.90	4.59	---
		L.	0.25	0.52	0.87	---
Fault zone	EW	H.	3.25	2.28	---	3.73
		L.	0.15	0.50	---	0.69
	NS	H.	3.35	2.39	---	3.53
		L.	0.18	0.49	---	0.65
	UD	H.	3.51	2.37	---	3.39
		L.	0.22	0.52	---	0.59
Hanging wall	EW	H.	3.14	2.46	---	1.61
		L.	0.69	0.74	---	1.10
	NS	H.	2.97	2.25	---	1.73
		L.	0.86	0.72	---	1.22
	UD	H.	2.98	2.66	---	1.77
		L.	0.71	0.71	---	1.09

840  
 841  
 842  
 843  
 844  
 845  
 846  
 847  
 848  
 849  
 850

Table 6: Summary of highs and lows of site spectral amplifications in the Akita-Iwate study area deduced from Figures 25, 26, and 27.

			SSA <sub>O/L.F</sub>	SSA <sub>O/r.F</sub>	SSA <sub>L.F/r.F</sub>	SSA <sub>r.F/l.F</sub>
Right Footwall	EW	H.	0.90	2.02	8.85	---
		L.	0.29	0.94	2.66	---
	NS	H.	0.89	2.14	15.59	---
		L.	0.28	1.13	2.78	---
	UD	H.	1.08	2.12	9.05	---
		L.	0.30	1.03	2.45	---
Fault zone (Hanging wall blocks)	EW	H.	2.08	2.98	---	3.47
		L.	0.57	0.93	---	0.83
	NS	H.	1.83	3.28	---	3.59
		L.	0.56	0.91	---	0.69
	UD	H.	2.02	3.06	---	3.89
		L.	0.64	0.85	---	0.86
Left Footwall	EW	H.	9.37	2.54	---	15.63
		L.	0.50	0.30	---	0.24
	NS	H.	7.45	2.39	---	14.19
		L.	0.46	0.30	---	0.22
	UD	H.	8.29	2.91	---	14.96
		L.	0.49	0.30	---	0.25

851  
 852  
 853  
 854

855

856

857

858

859

860 Table 7: Summary of highs and lows of site spectral amplifications in the Fukushima study area  
861 deduced from Figures 28 and 29.

862

			SSA <sub>OH</sub>	SSA <sub>OF</sub>	SSA <sub>HF</sub>	SSA <sub>FH</sub>
Footwall	EW	H.	4.79	7.13	4.79	---
		L.	0.32	0.76	1.32	---
	NS	H.	6.14	7.24	4.40	---
		L.	0.26	0.44	1.07	---
	UD	H.	5.78	7.92	4.53	---
		L.	0.41	0.81	1.27	---
Hanging wall	EW	H.	2.72	7.91	---	2.11
		L.	0.59	1.07	---	0.45
	NS	H.	2.61	8.44	---	1.29
		L.	0.58	0.99	---	0.41
	UD	H.	3.02	8.70	---	1.89
		L.	0.58	0.68	---	0.41

863

864

# Figures

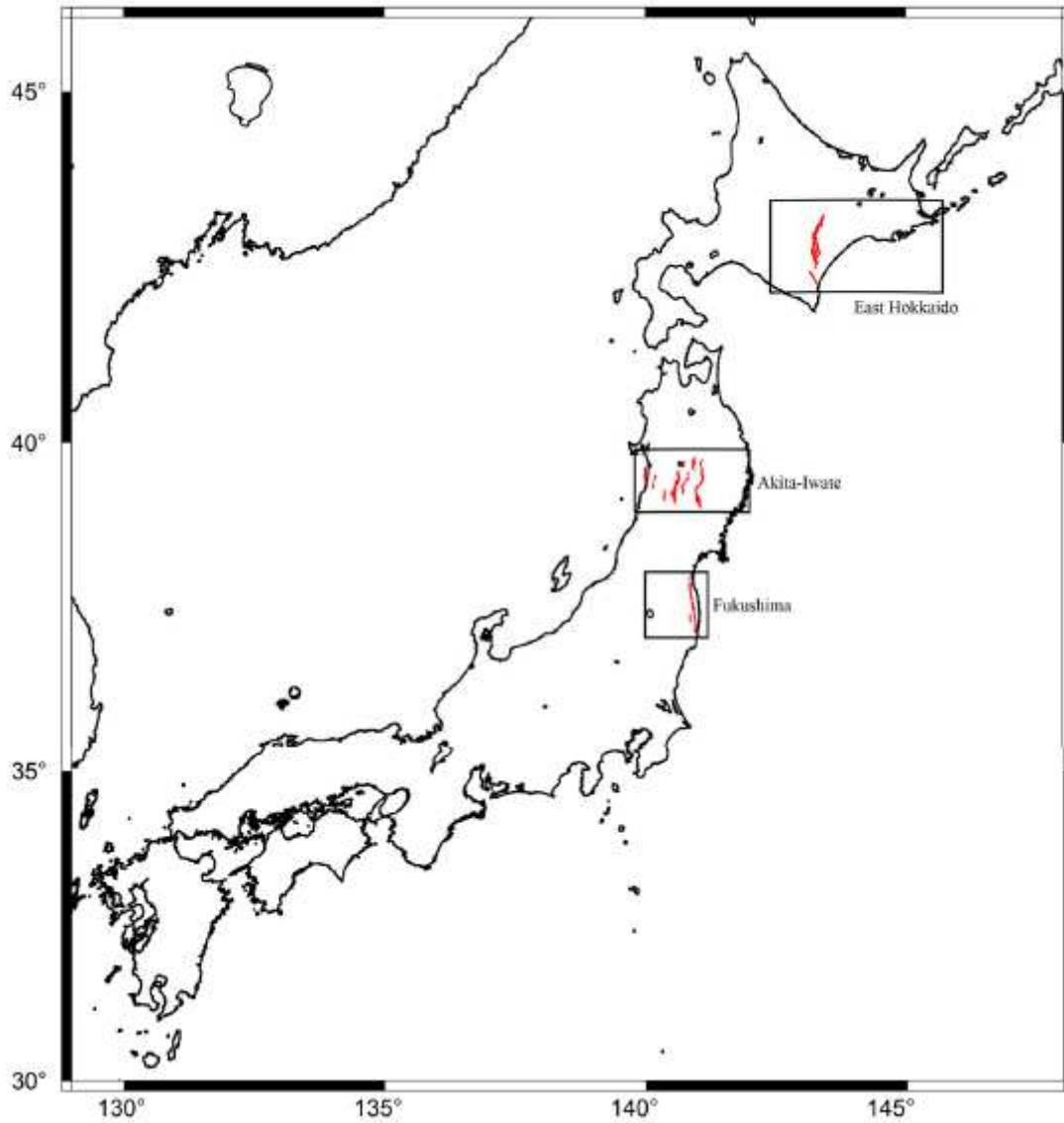


**Figure 1**

Location map for the three different study areas of East Hokkaido, Akita-Iwate, and Fukushima in Japan that are used in the present study. (Note: red lines are representing the active reverse fault traces)

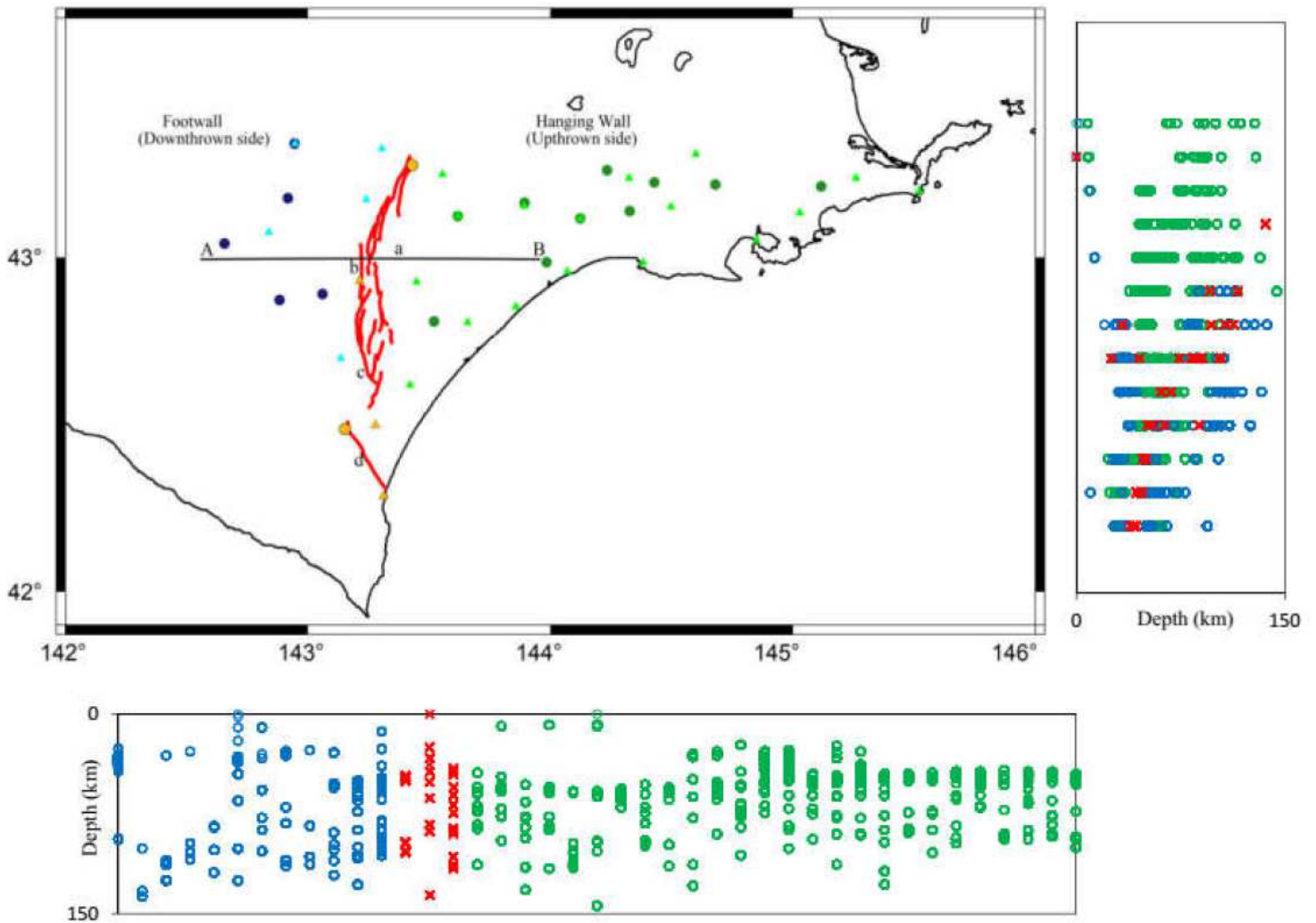


**Figure 2**

Distribution of K-NET (triangles) and KiK-net (circles) seismic stations and the recorded earthquakes with their focal depths in East Hokkaido study area. (Note: The station's color of blue, yellow, or green on map, and the focal depth's color of blue, red, or green are used to discriminate locations on and beneath FW, FZ, or HW, respectively. Red lines on map are representing active reverse fault traces. AB is profile across fault zones.)

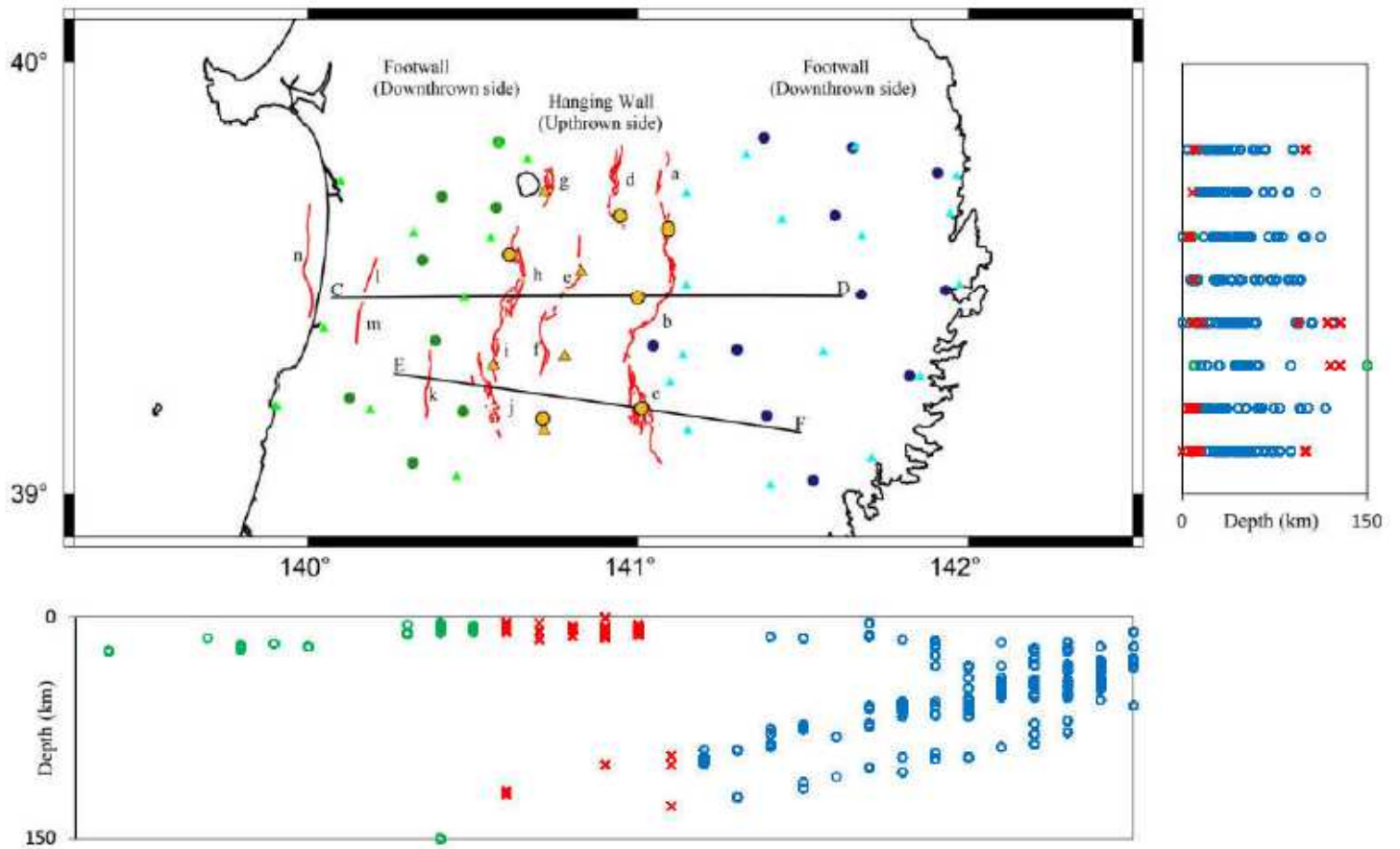


**Figure 3**

Distribution of K-NET (triangles) and KiK-net (circles) seismic stations and the recorded earthquakes with their focal depths in Akita-Iwate study area. (Note: On map, the colors of green, blue, and yellow are used to discriminate seismic stations located on left and right footwall blocks, and fault zone, respectively. For events, the colors of green, blue, and red are used to discriminate focal depths beneath left and right FW, and FZ, respectively. Red lines on map are representing active reverse fault traces. CD and EF are profiles across fault zones.)

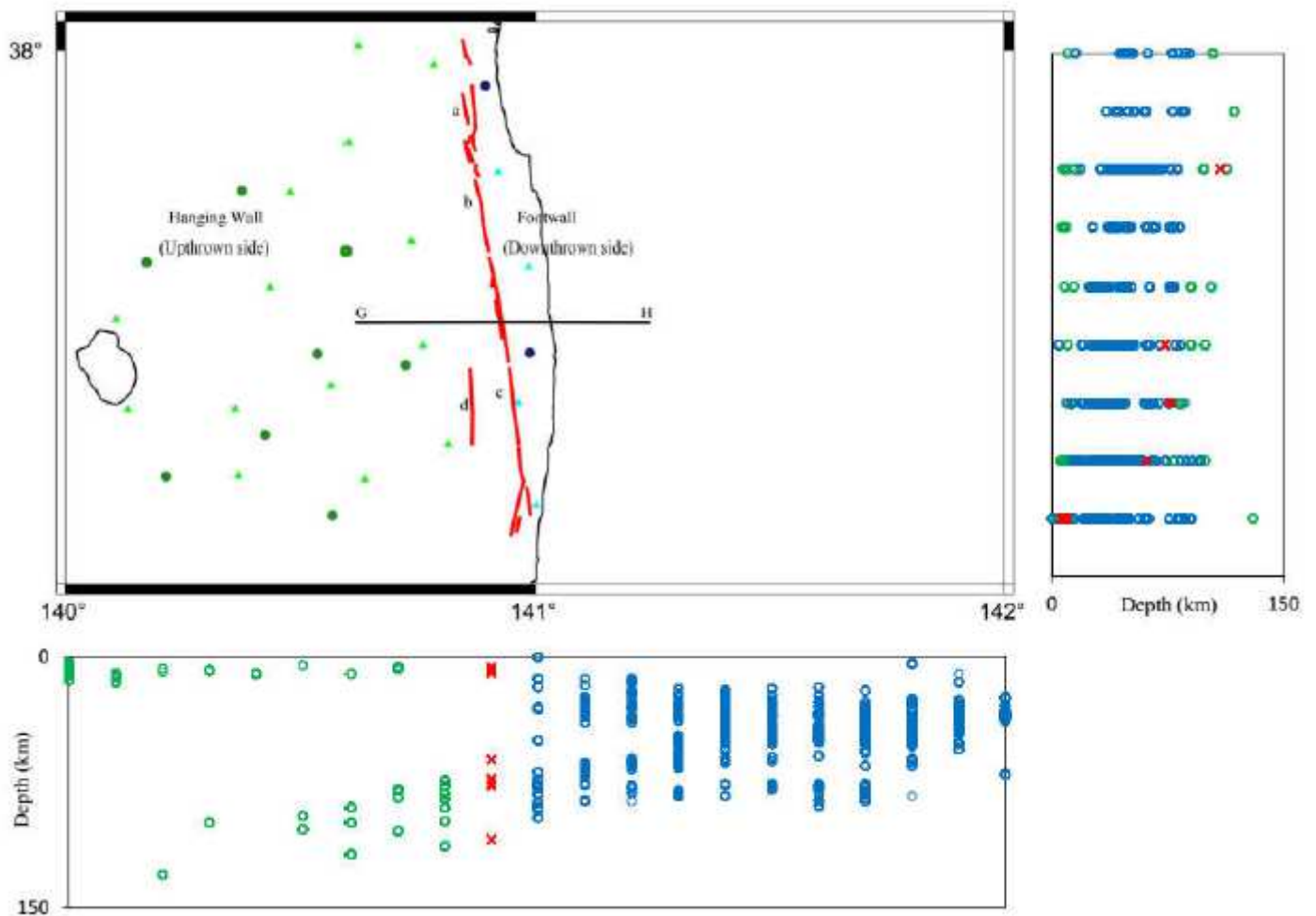


**Figure 4**

Distribution of K-NET (triangles) and KiK-net (circles) seismic stations and the recorded earthquakes with their focal depths in Fukushima study area. (Note: On map, the colors of green and blue are used to discriminate seismic stations located on hanging wall block and footwall blocks, respectively. For events, the colors of green, red, and blue are used to discriminate focal depths beneath HW, FZ, and FW, respectively. Red lines on map are representing active reverse fault traces. GH is profile across fault zones.)

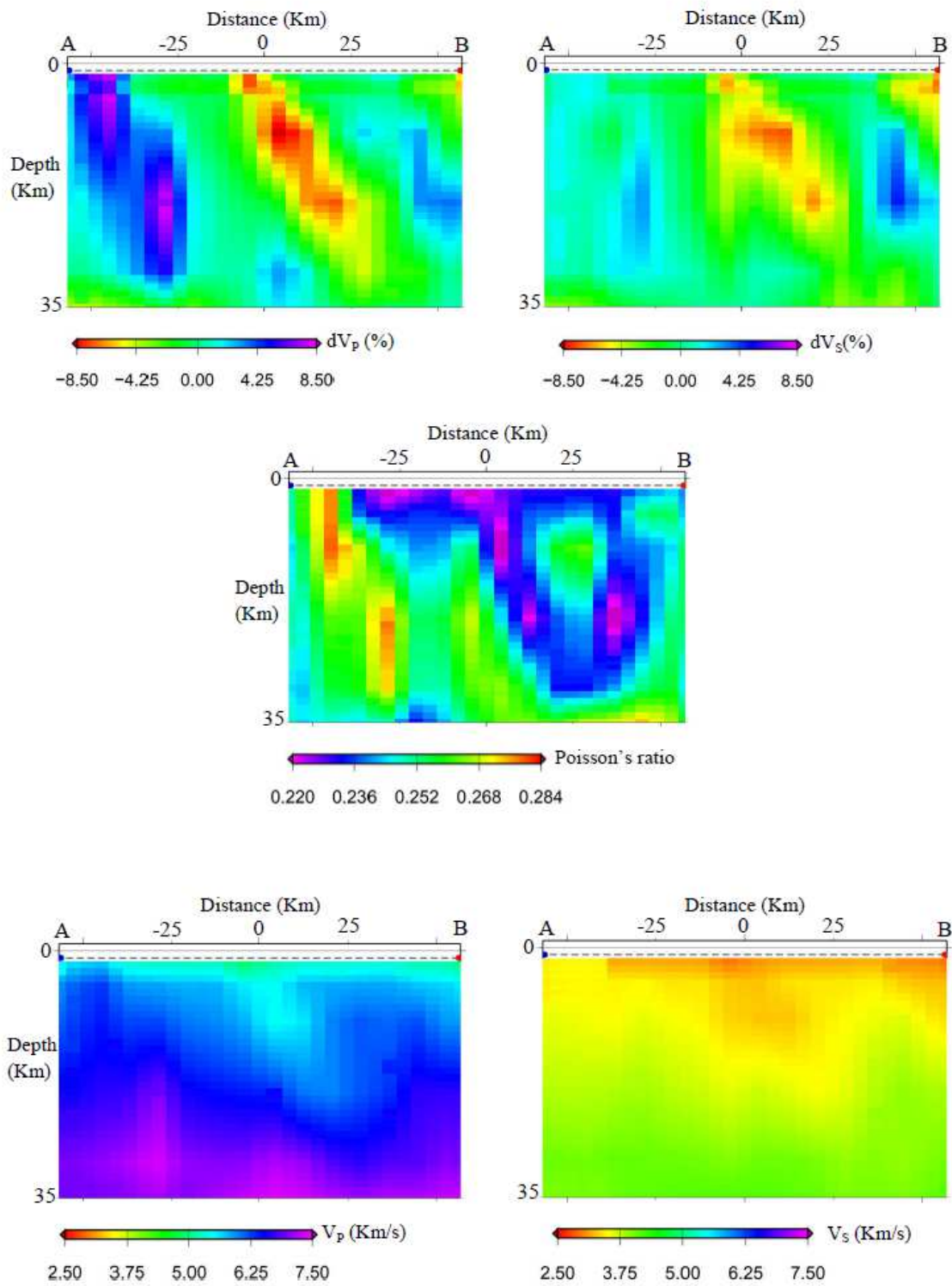


**Figure 5**

Subsurface tomography structures along profile AB in East Hokkaido study area.

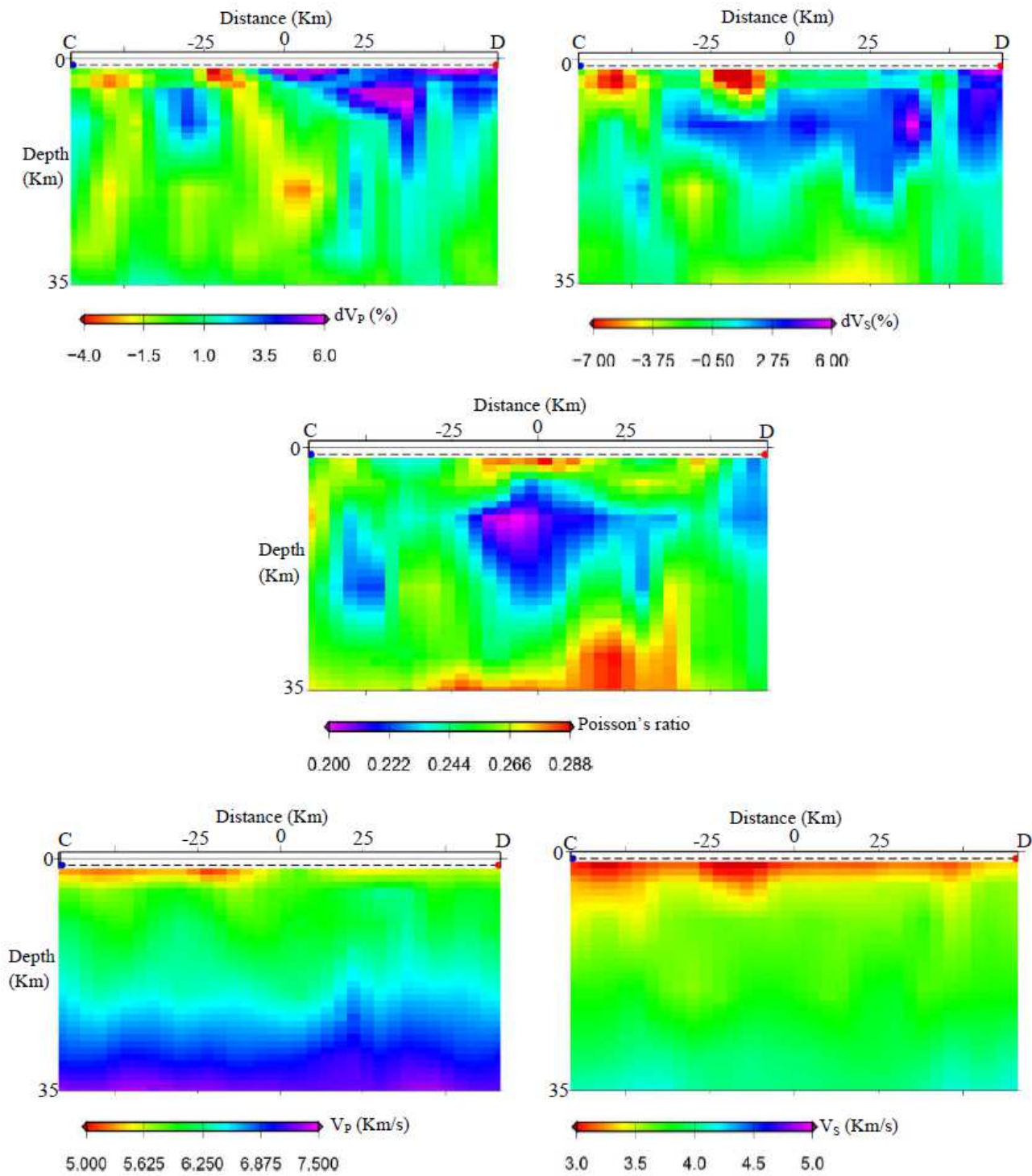


**Figure 6**

Subsurface tomography structures along profile CD in Akita-Iwate study area.

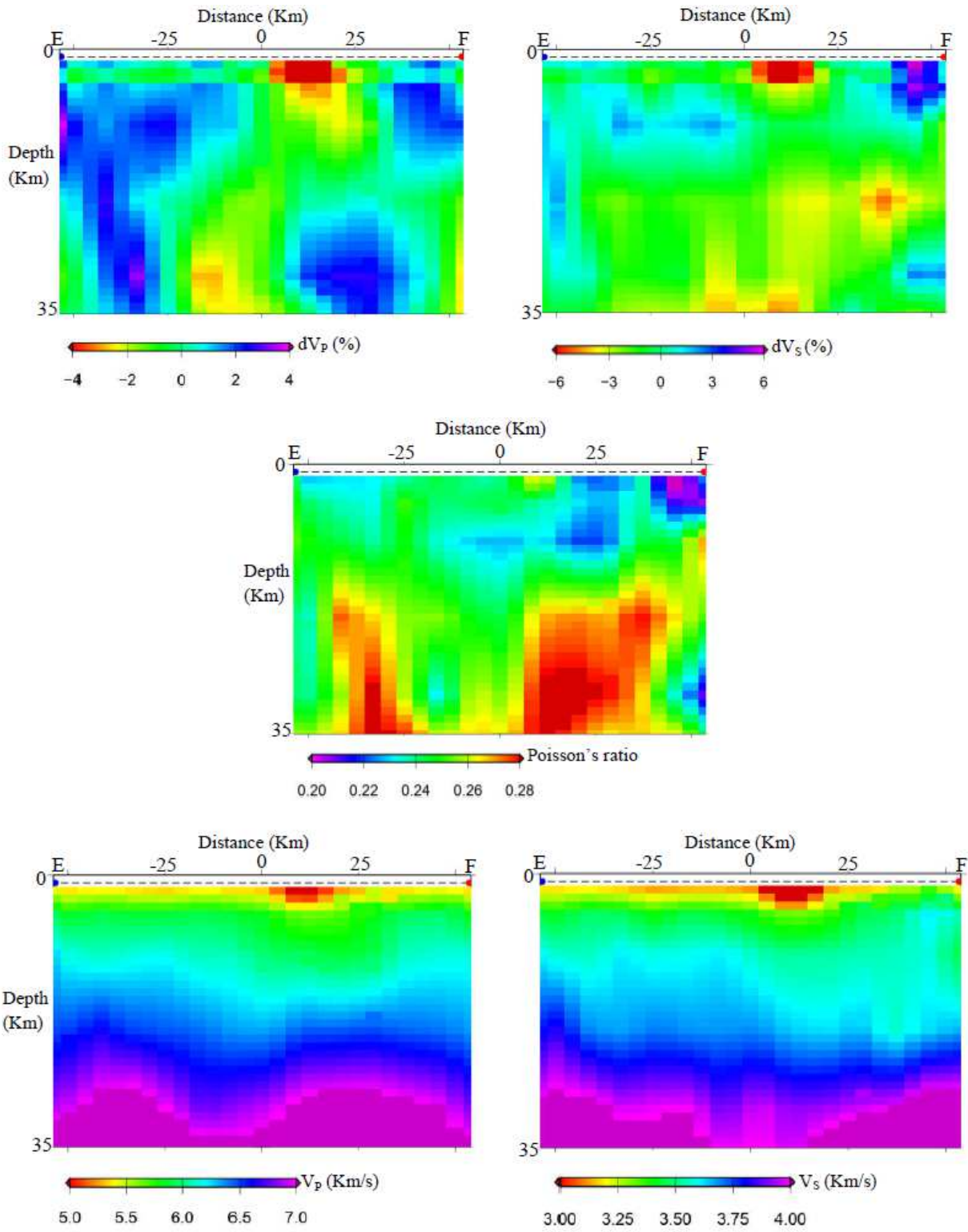


**Figure 7**

Subsurface tomography structures along profile EF in Akita-Iwate study area.

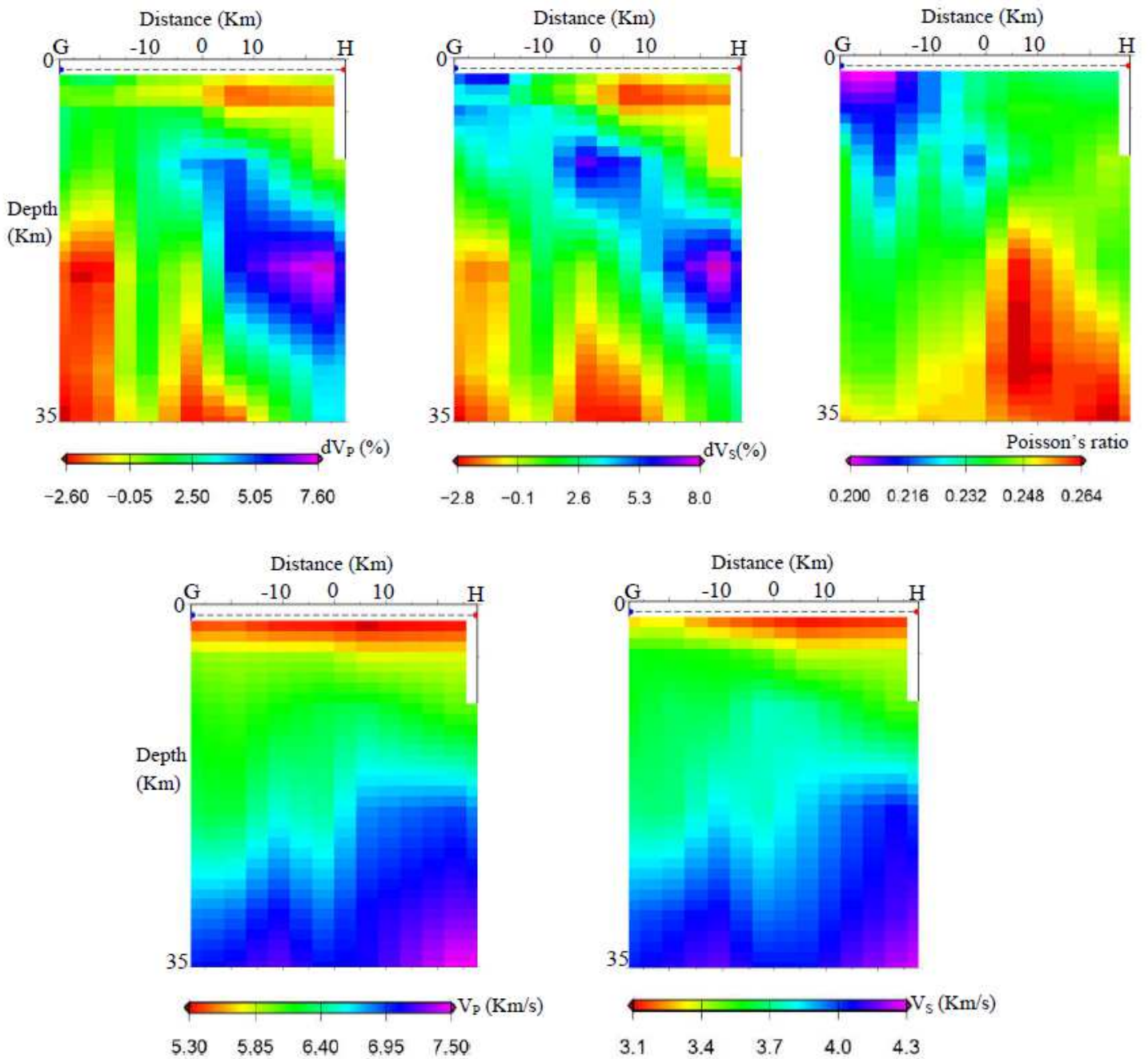


**Figure 8**

Subsurface tomography structures along profile GH in Fukushima study area based on calculation by Nakamura et al. (2008).

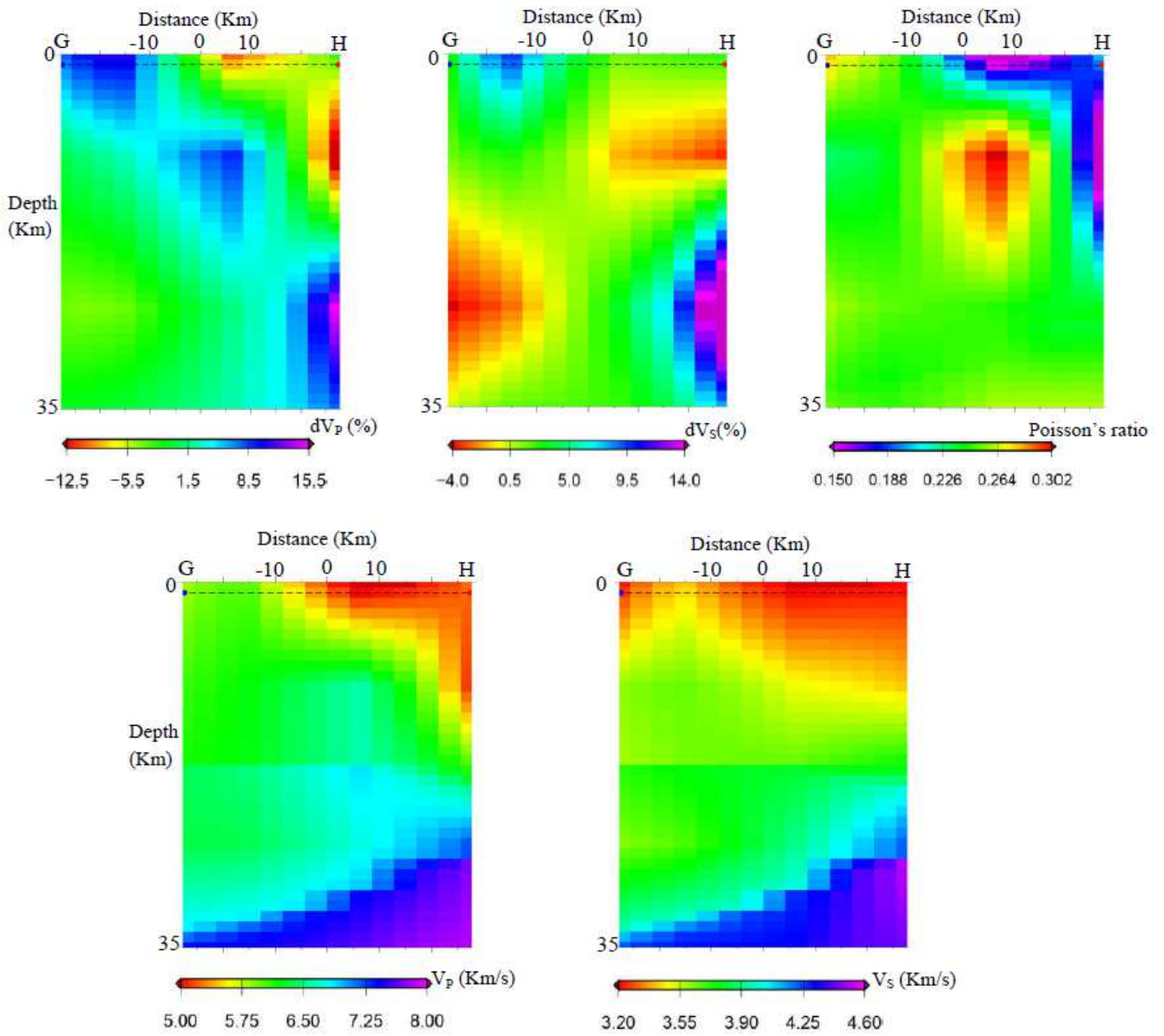


**Figure 9**

Subsurface tomography structures along profile GH in Fukushima study area based on calculation by Nakajima et al. (2001).

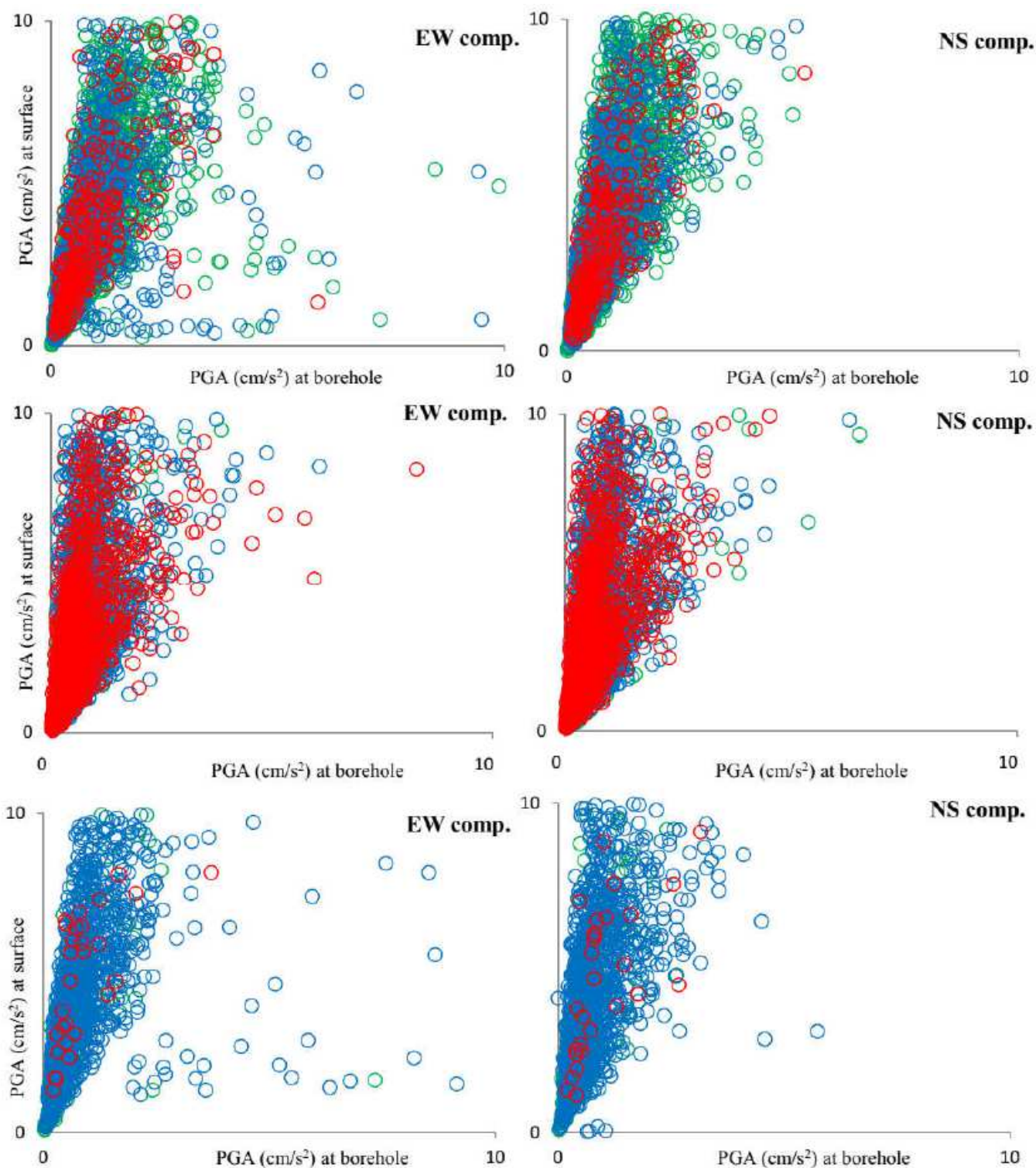


**Figure 10**

Correlation between PGAs of EW and NS components at surface and borehole obtained from KiK-net stations at the East Hokkaido (upper), Akita-Iwate (middle), and Fukushima (lower) study areas. (Note: colors of green, blue, and red are used to discriminate PGAs on HW (l.FW in the Akita-Iwate study area), FW (r.FW in Akita-Iwate study area), and FZ (upthrown blocks in the Akita-Iwate study area), respectively)

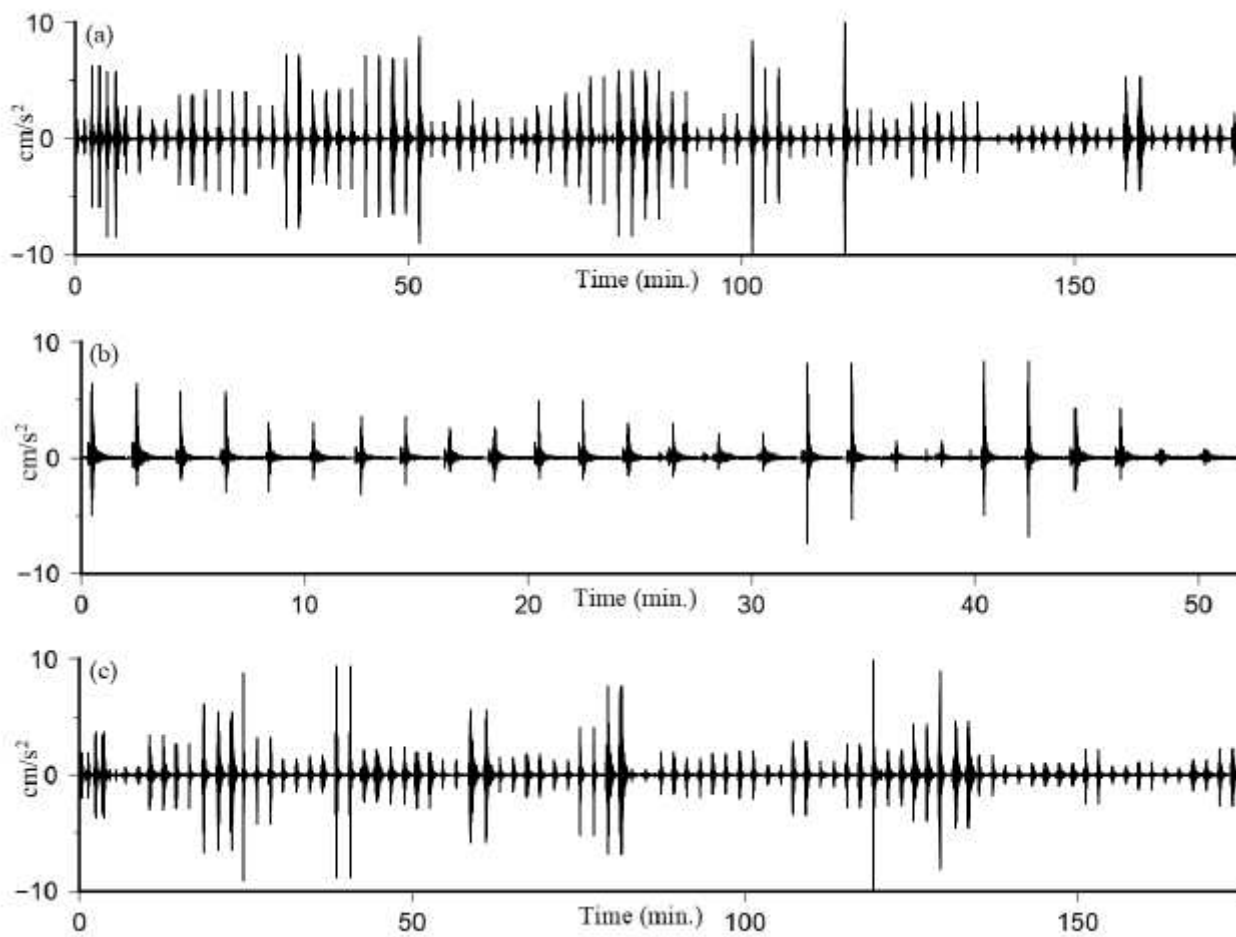


**Figure 11**

Example of continuous time series of EW components recorded at TKCH05 KiK-net station with their hypocenters located beneath FW (a), FZ (b), HW (c).

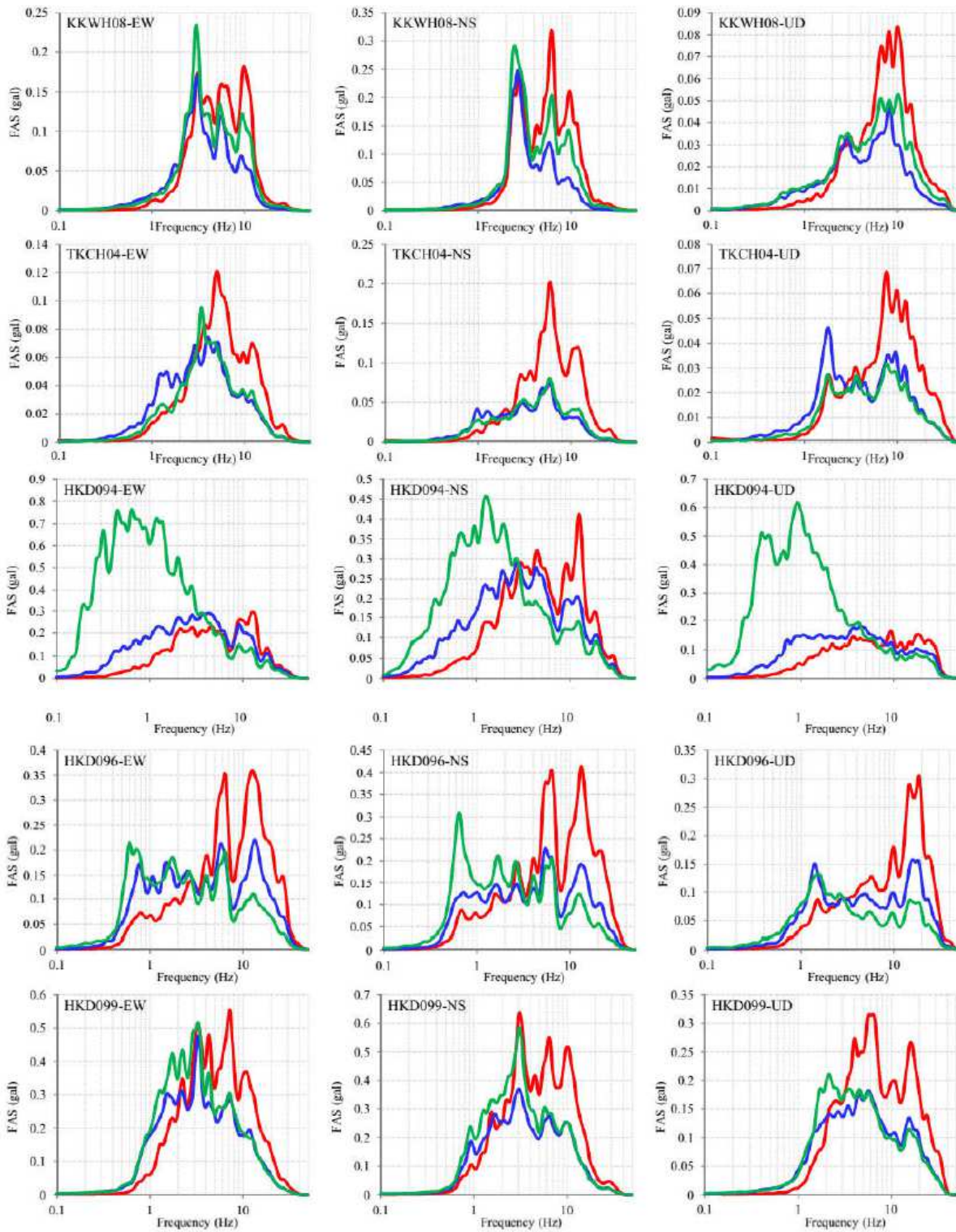


**Figure 12**

FASs at seismic stations located on FW block in the East Hokkaido study area due to recorded EFWs (blue), EFZs (red), and EHWs (green).

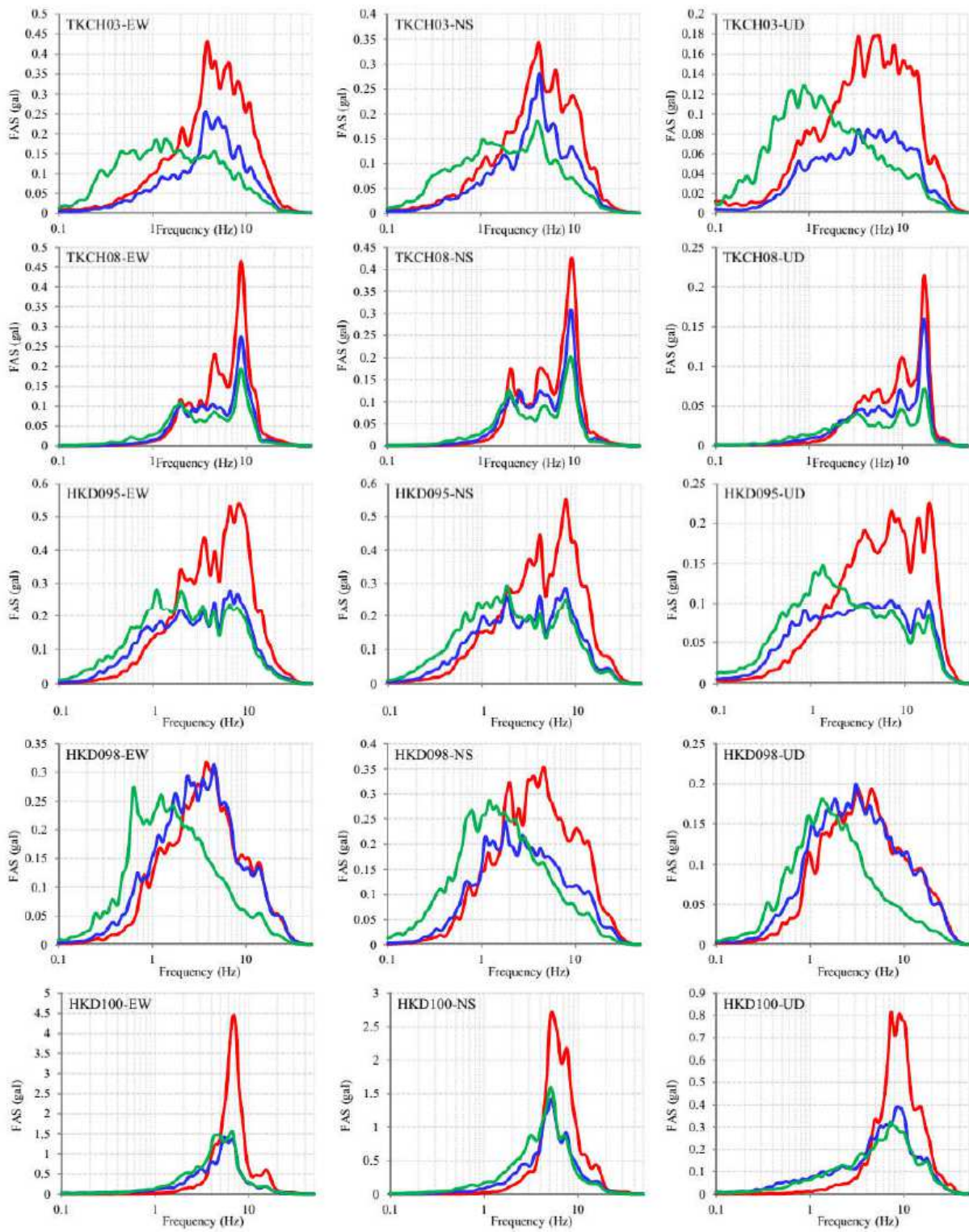


**Figure 13**

FASs at seismic stations located on FZ in the East Hokkaido study area due to recorded EFWs (blue), EFZs (red), and EHWs (green).

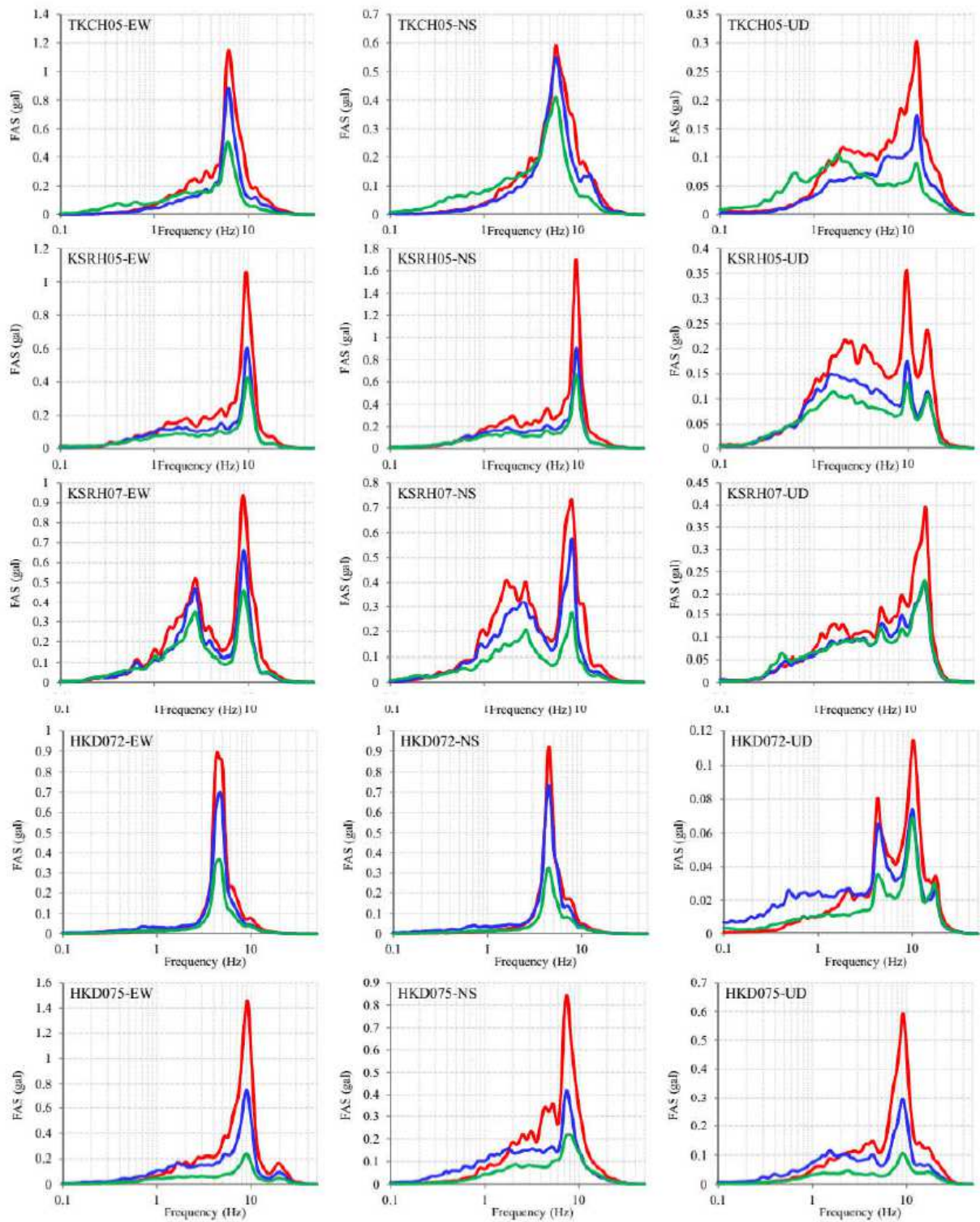


**Figure 14**

FASs at seismic stations located on HW block in the East Hokkaido study area due to recorded EFWs (blue), EFZs (red), and EHWs (green).

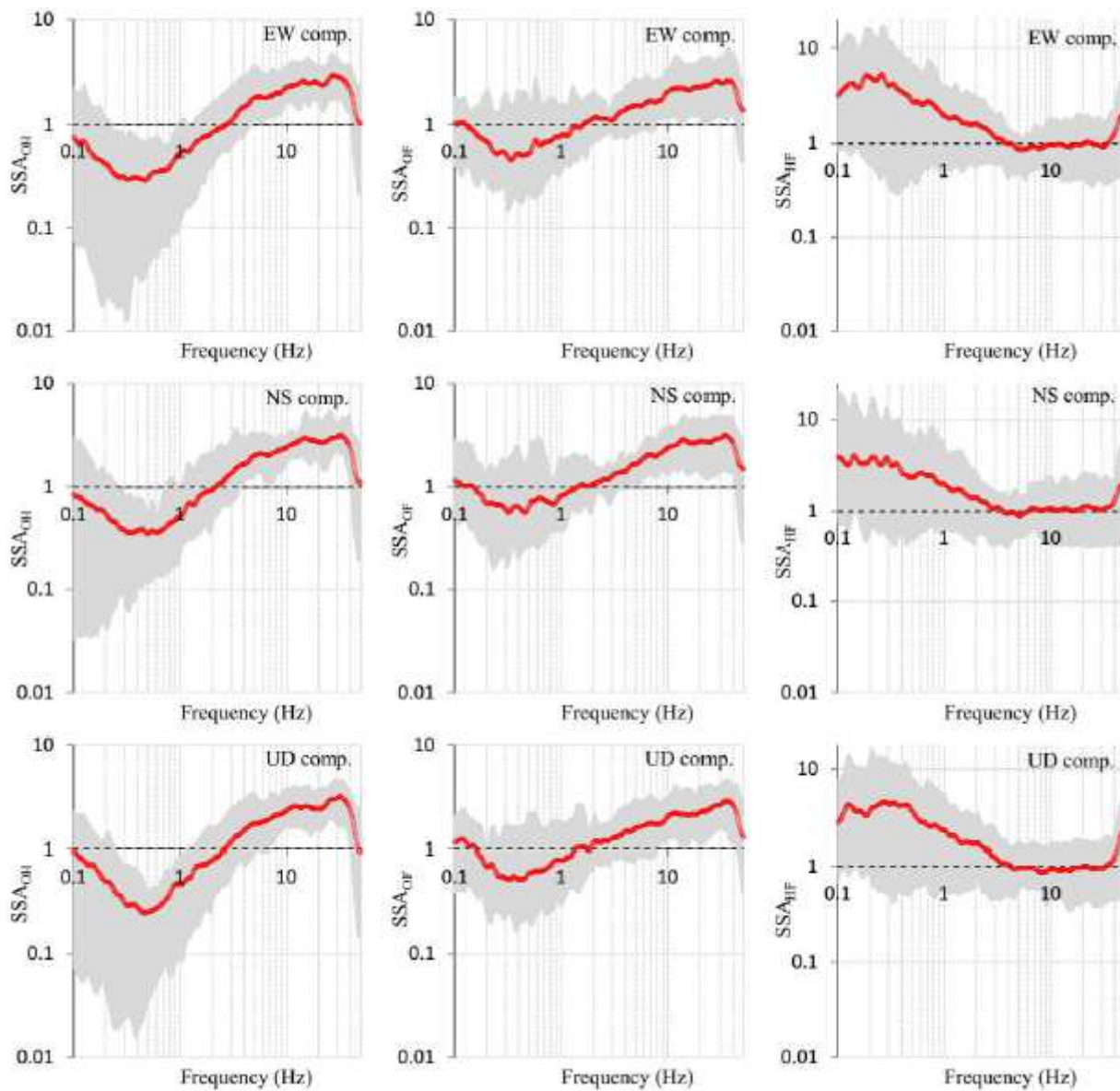


**Figure 15**

The estimated average SSAs (red) with their minimum and maximum (gray), which are calculated based on equations 1, 2, and 3 for the seismic stations located on the FW block in East Hokkaido study area.

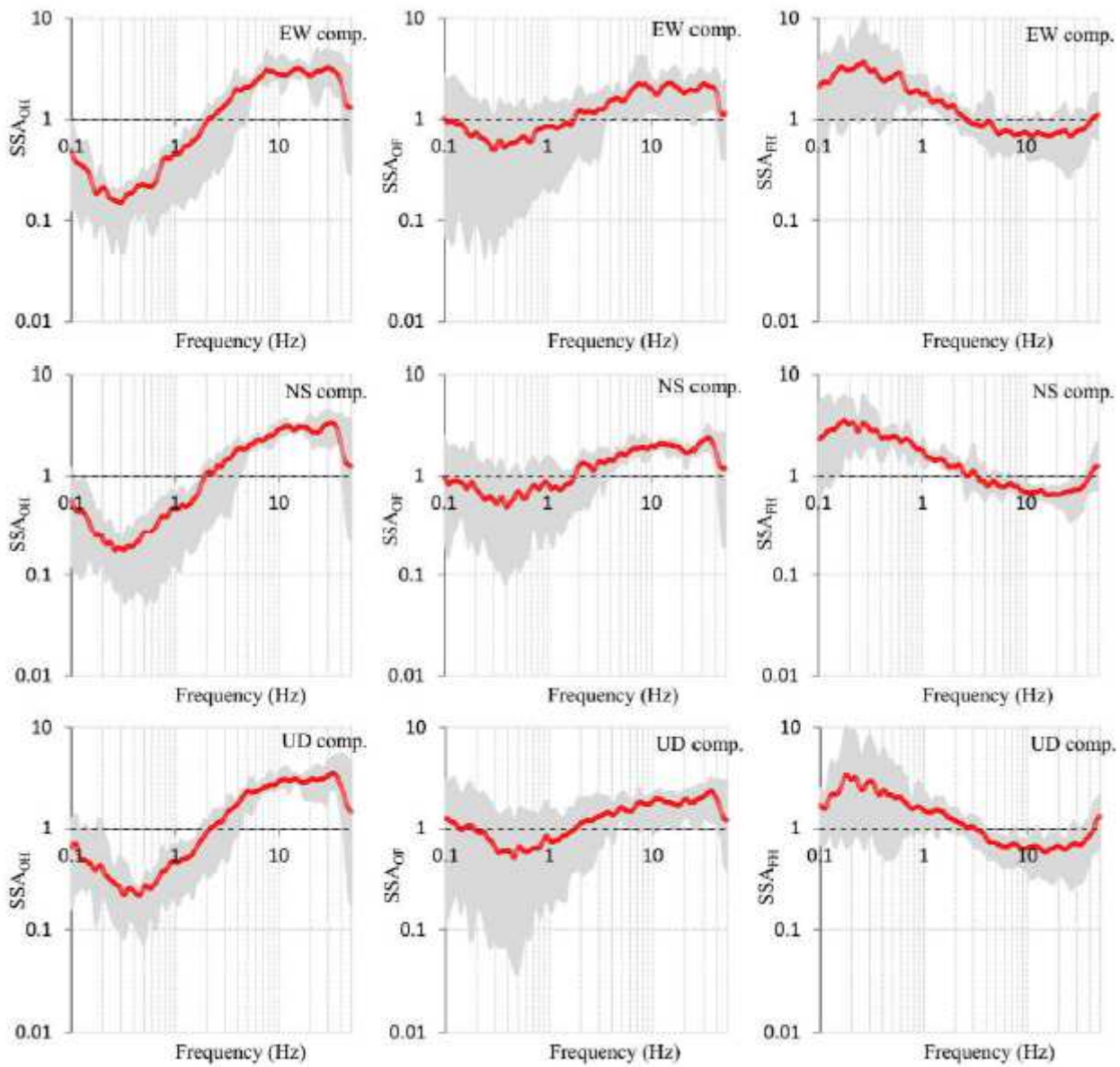


**Figure 16**

The estimated average SSAs (red) with their minimum and maximum (gray), which are calculated based on equations 1, 2, and 4 for the seismic stations located on the FZ in East Hokkaido study area.

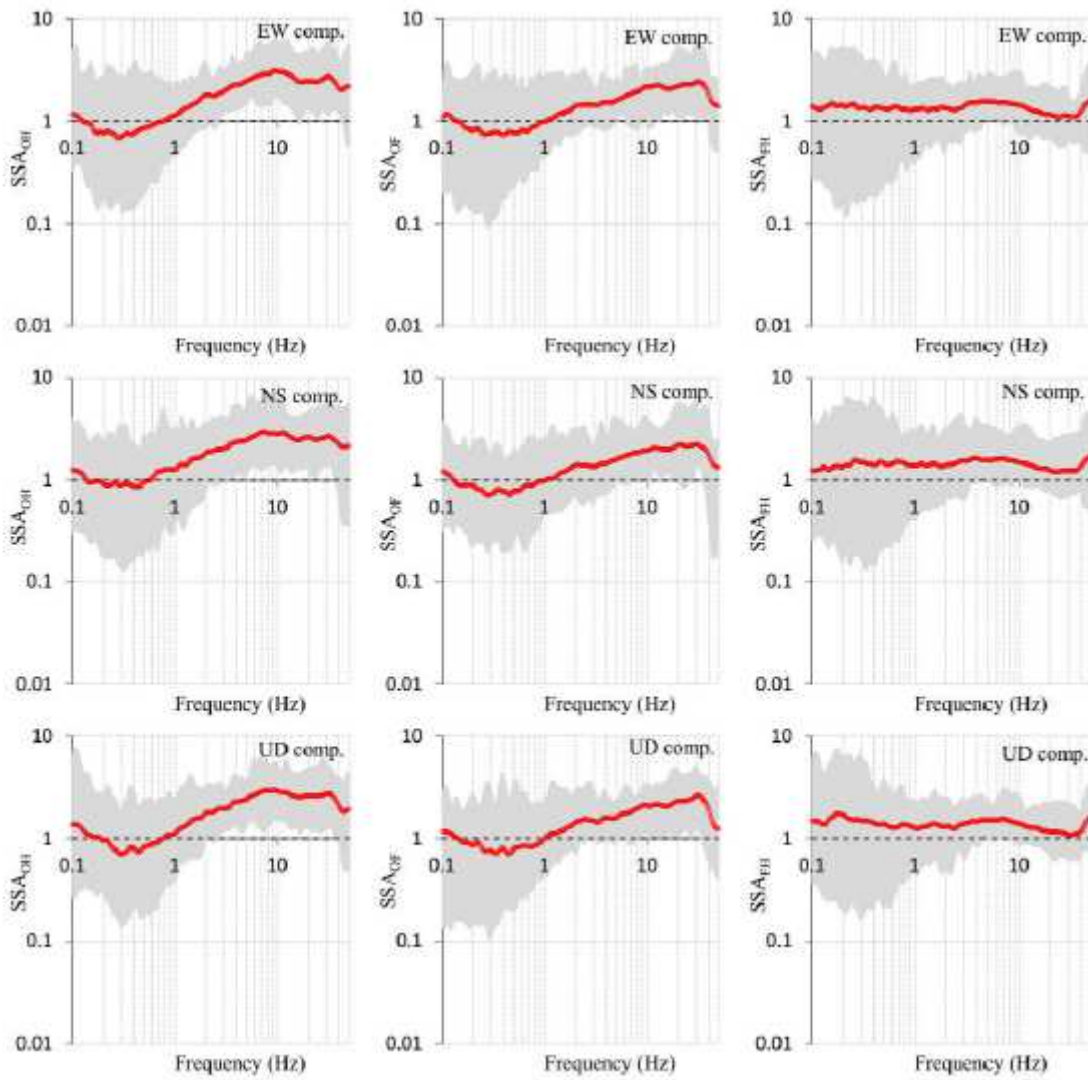


**Figure 17**

The estimated average SSAs (red) with their minimum and maximum (gray), which are calculated based on equations 1, 2, and 4 for the seismic stations located on the HW block in East Hokkaido study area.

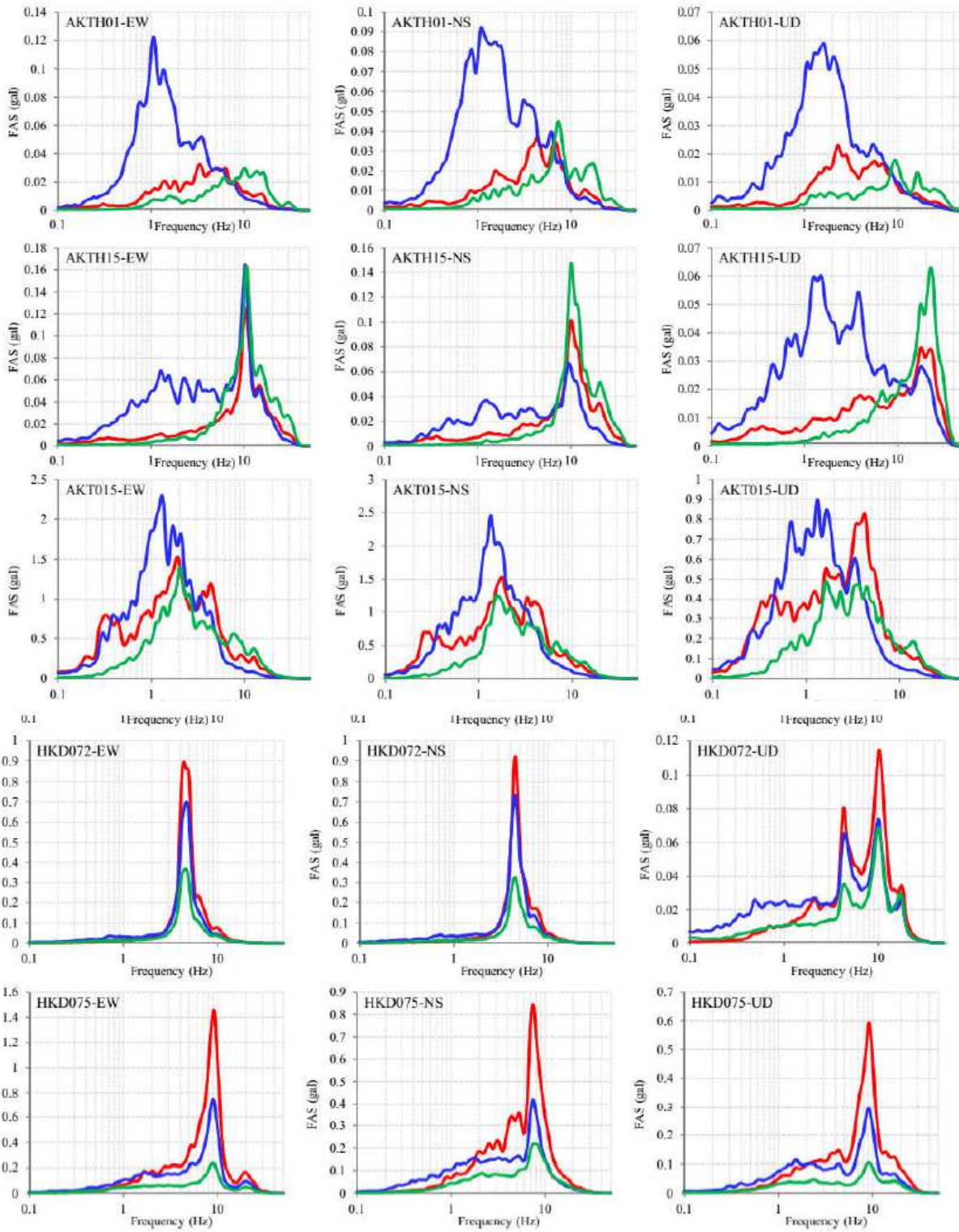


**Figure 18**

FASs at seismic stations located on I.FW block in Akita-Iwate study area due to recorded El.FWs (green), EFZs (red), and Er.FWs (blue).

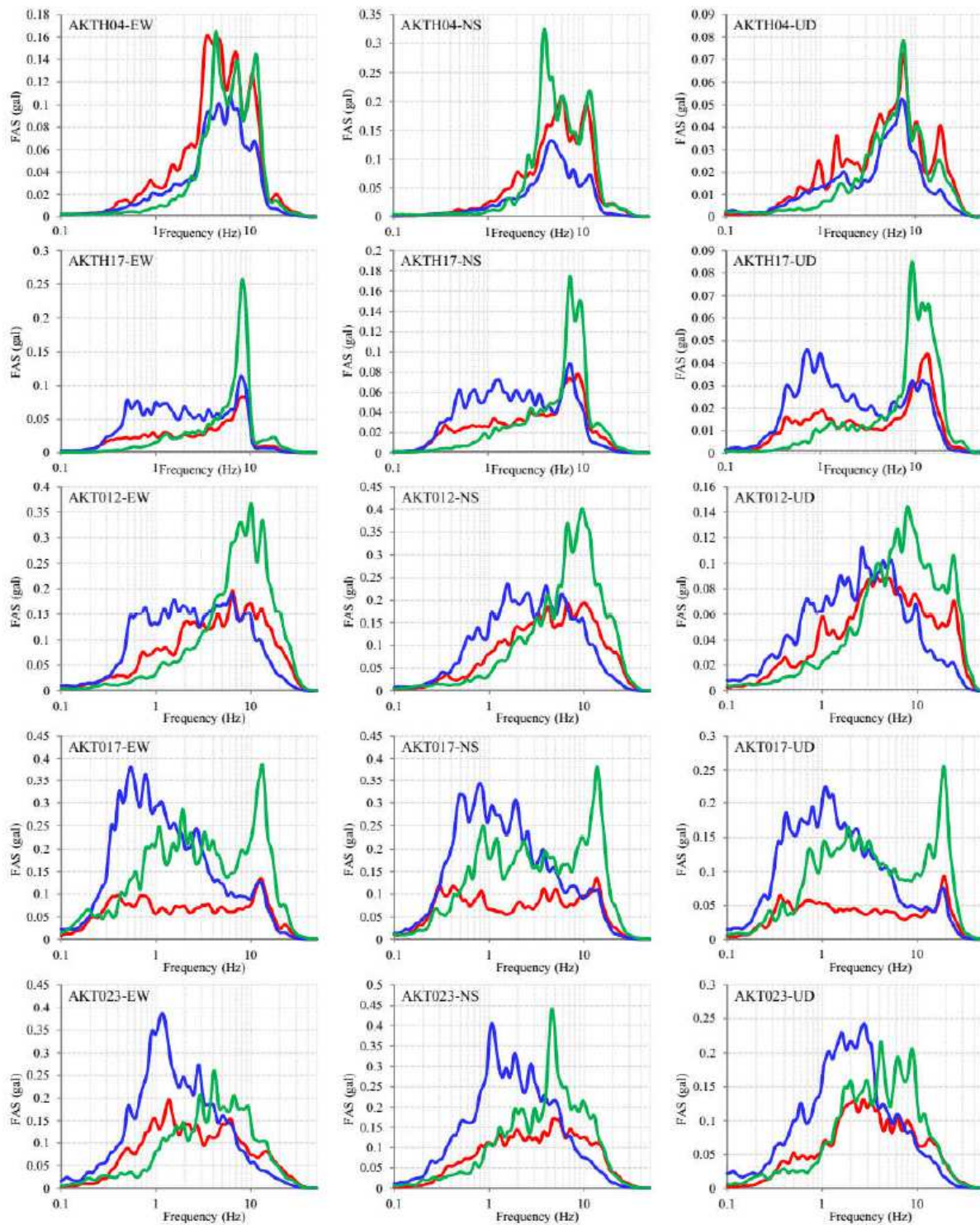


**Figure 19**

FASs at seismic stations located on FZ in Akita-Iwate study area due to recorded El.FWs (green), EFZs (red), and Er.FWs (blue).

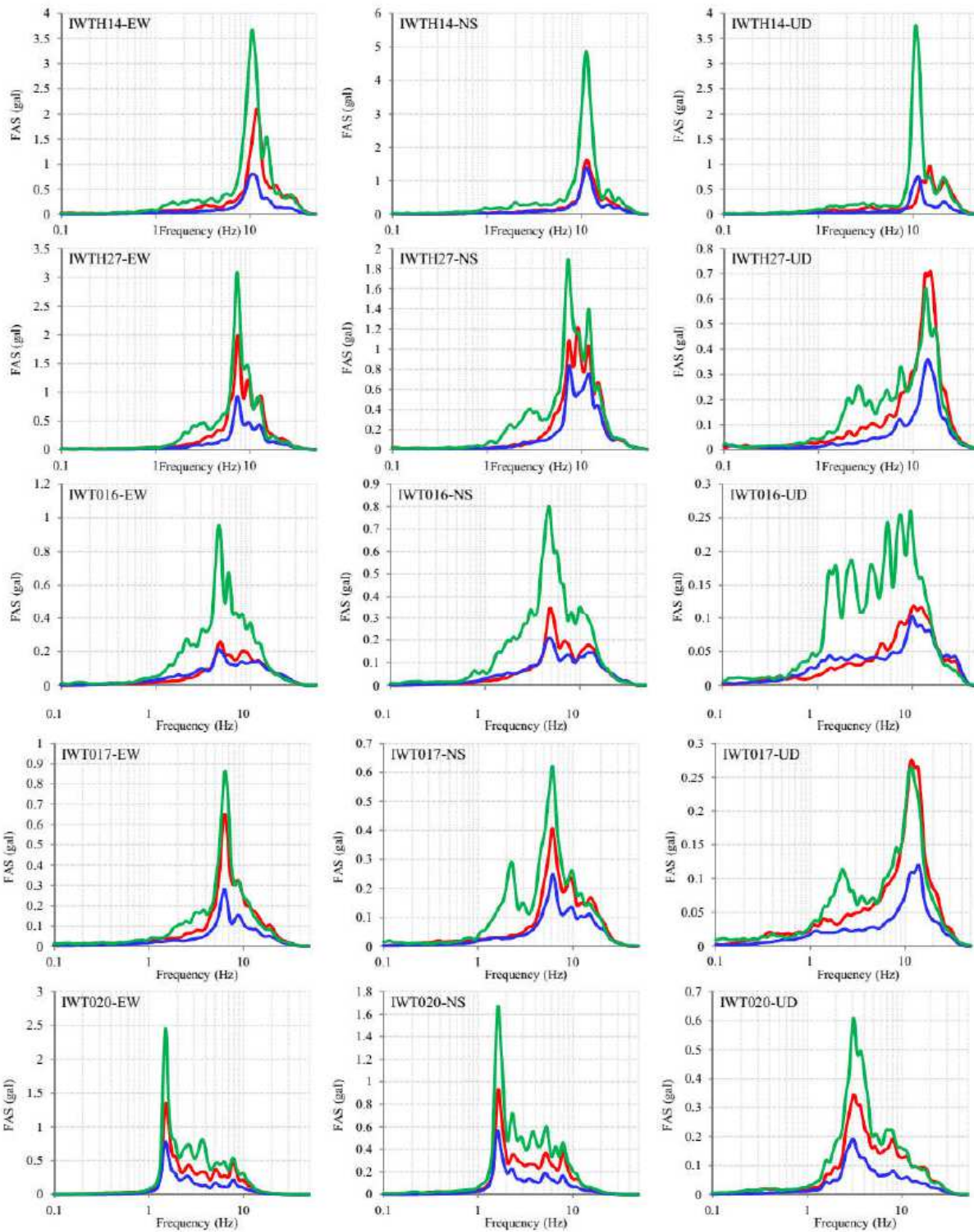


**Figure 20**

FASs at seismic stations located on r.FW block in Akita-Iwate study area due to recorded El.FWs (green), EFZs (red), and Er.FWs (blue).

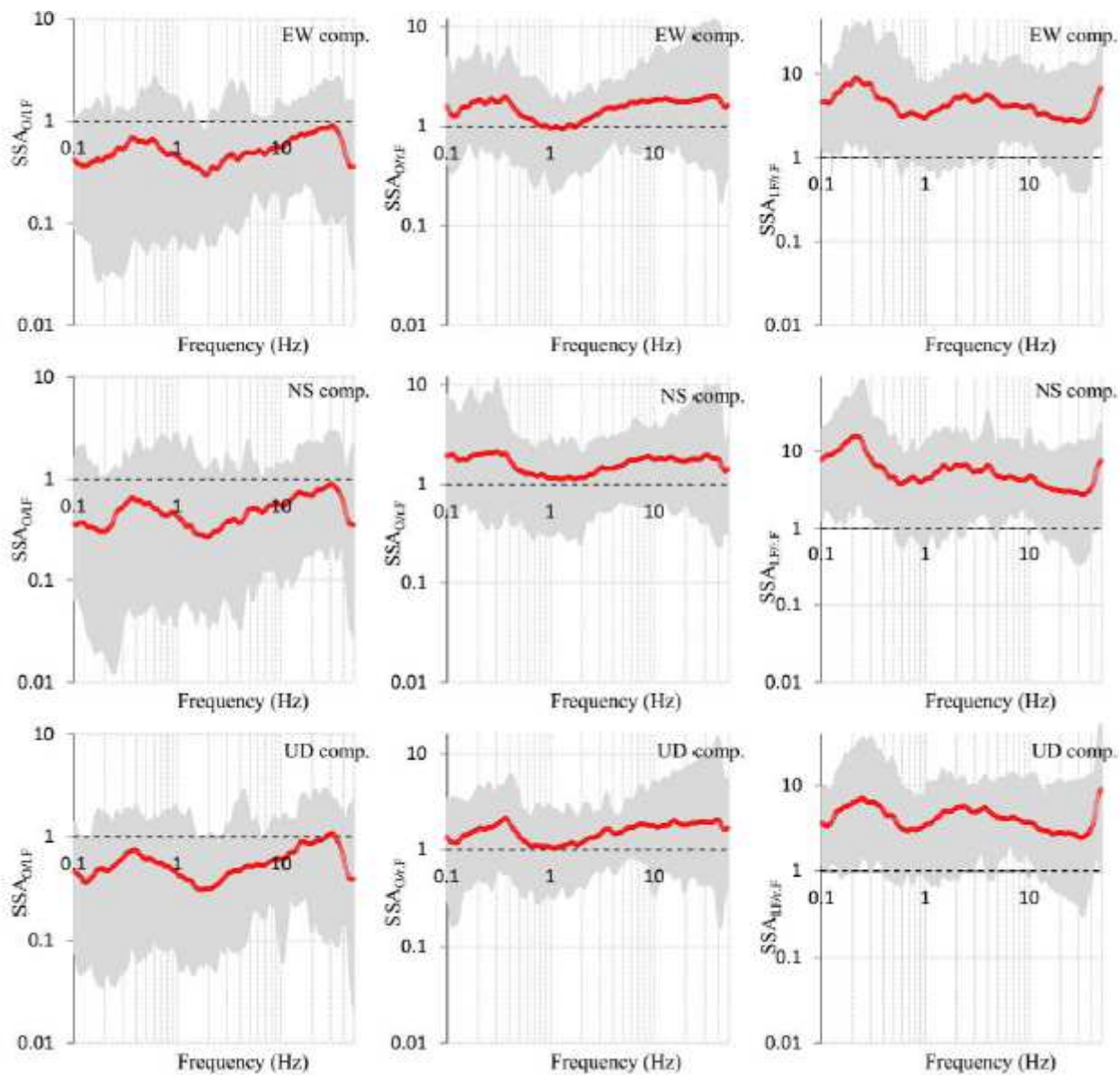


**Figure 21**

The estimated average SSAs (red) with their minimum and maximum (gray), which are calculated based on equations 1, 2, and 3 for the seismic stations located on the r.FW block in Akita-Iwate study area.

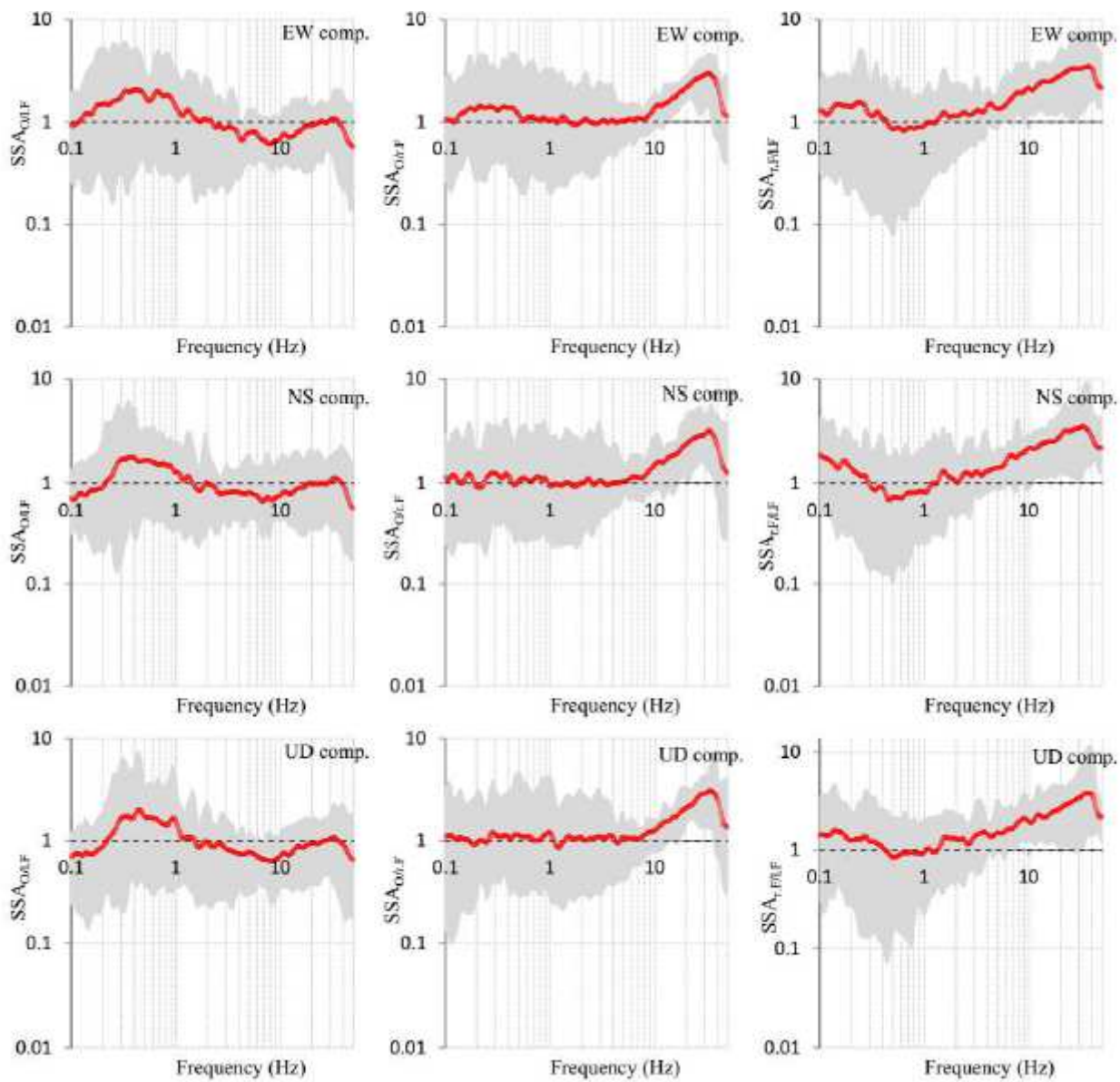


**Figure 22**

The estimated average SSAs (red) with their minimum and maximum (gray), which are calculated based on equations 1, 2, and 4 for the seismic stations located on the FZ in Akita-Iwate study area.

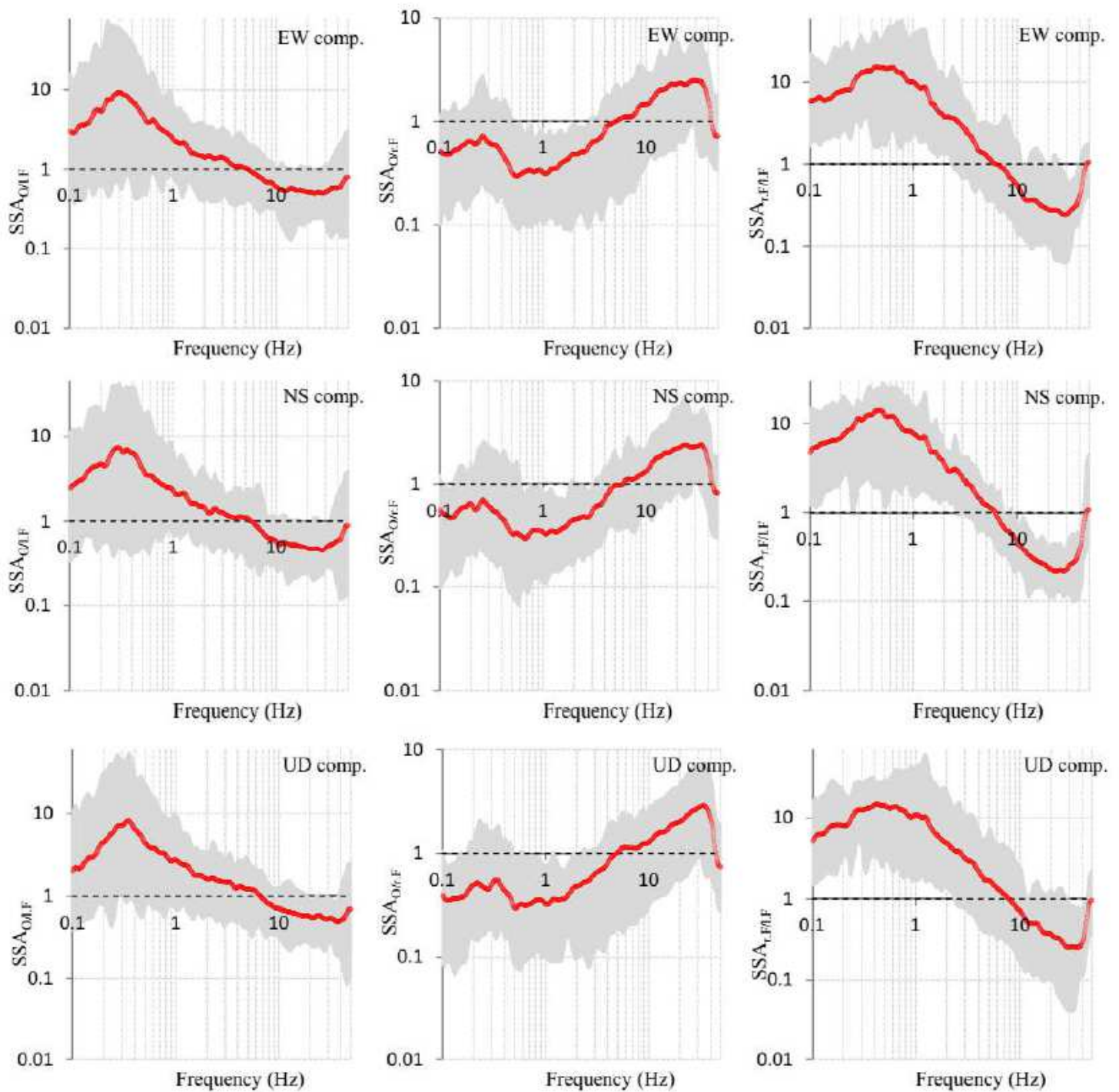


**Figure 23**

The estimated average SSAs (red) with their minimum and maximum (gray), which are calculated based on equations 1, 2, and 4 for the seismic stations located on the I.FW block in Akita-Iwate study area.

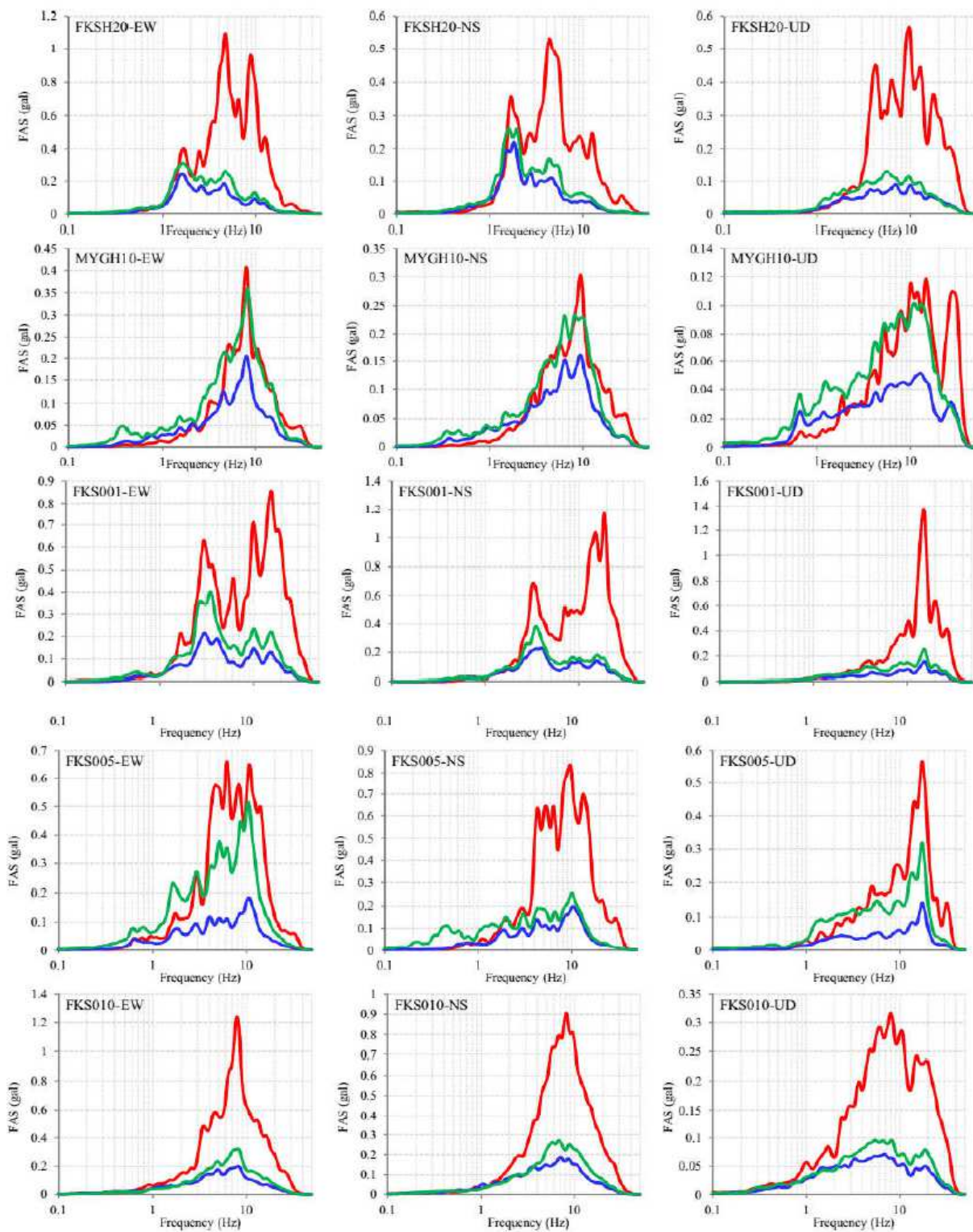


**Figure 24**

FASs at seismic stations located on FW block in Fukushima study area due to recorded EFWs (blue), EFZs (red), and EHWs (green).

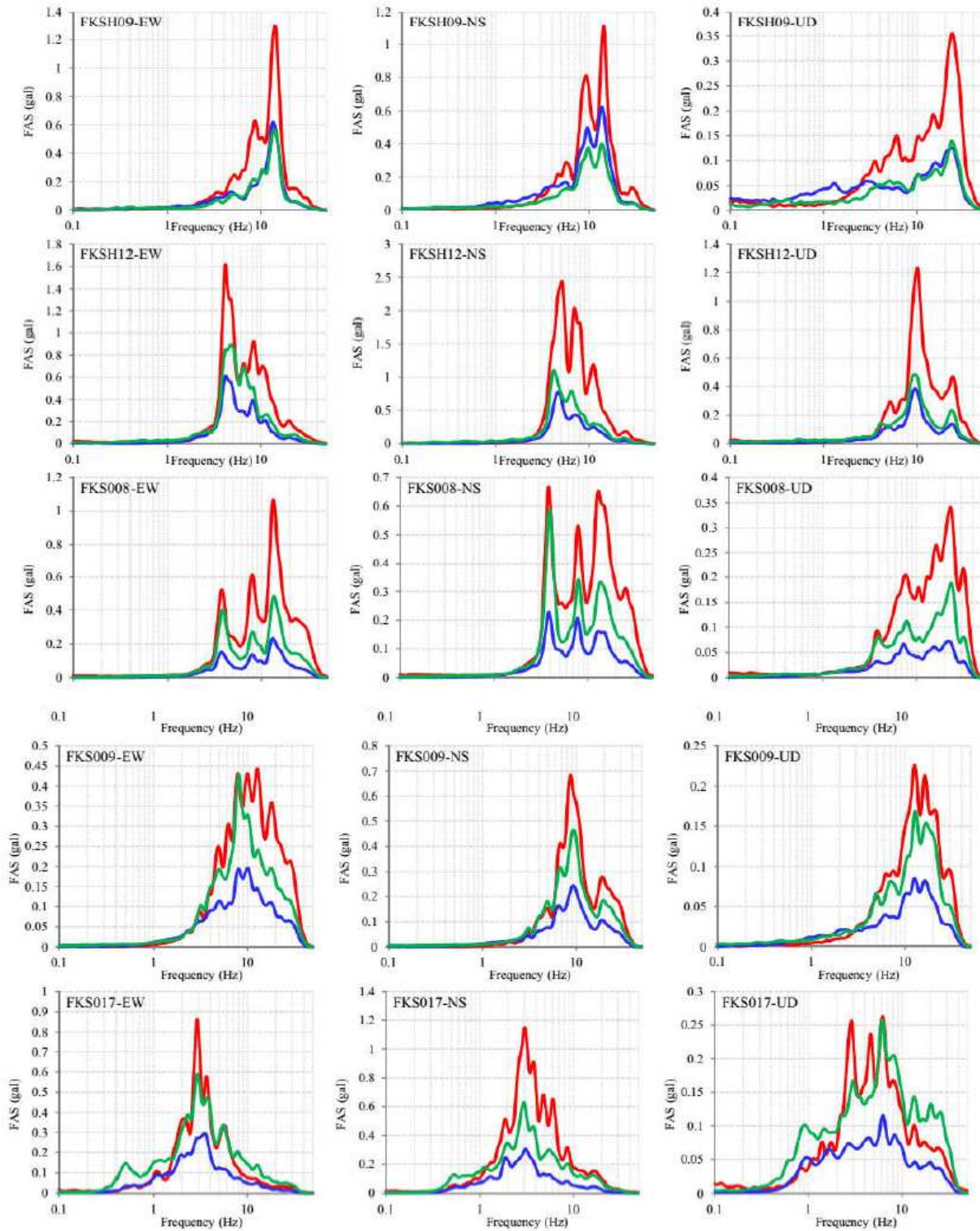


**Figure 25**

FASs at seismic stations located on HW block in Fukushima study area due to recorded EFWs (blue), EFZs (red), and EHWs (green).

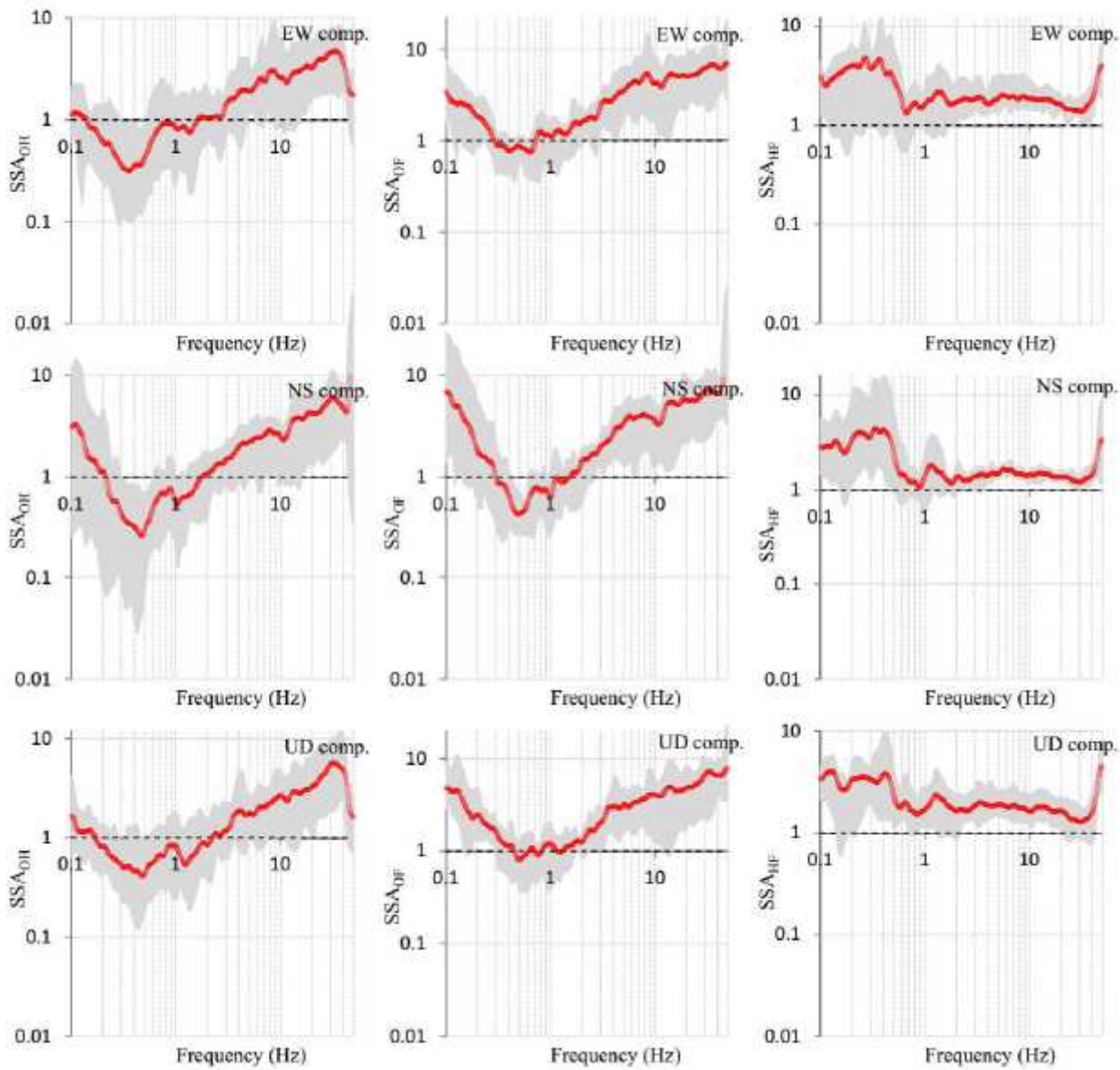


**Figure 26**

The estimated average SSAs (red) with their minimum and maximum (gray), which are calculated based on equations 1, 2, and 3 for the seismic stations located on the FW block in Fukushima study area.

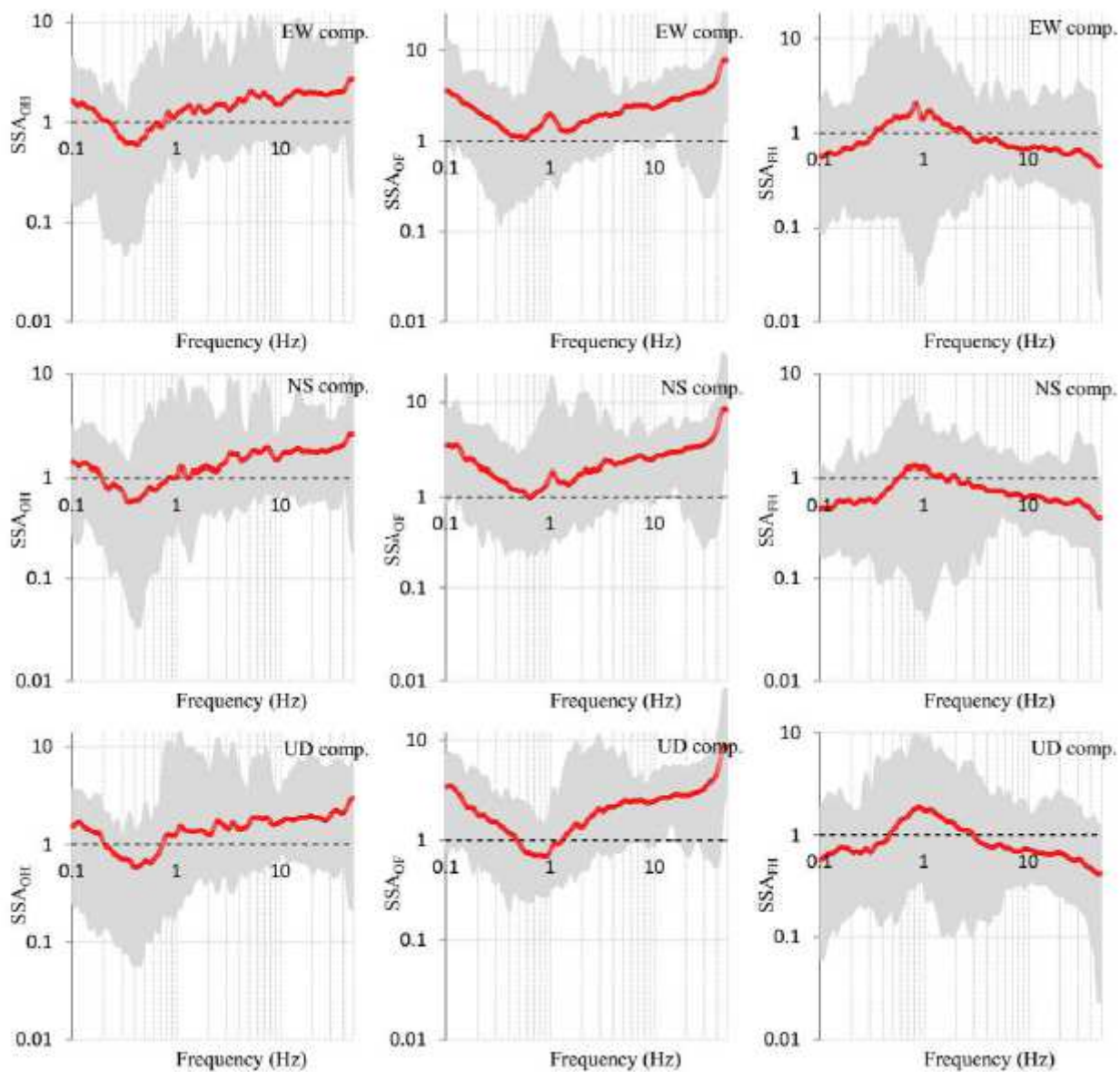


**Figure 27**

The estimated average SSAs (red) with their minimum and maximum (gray), which are calculated based on equations 1, 2, and 4 for the seismic stations located on the HW block in Fukushima study area.

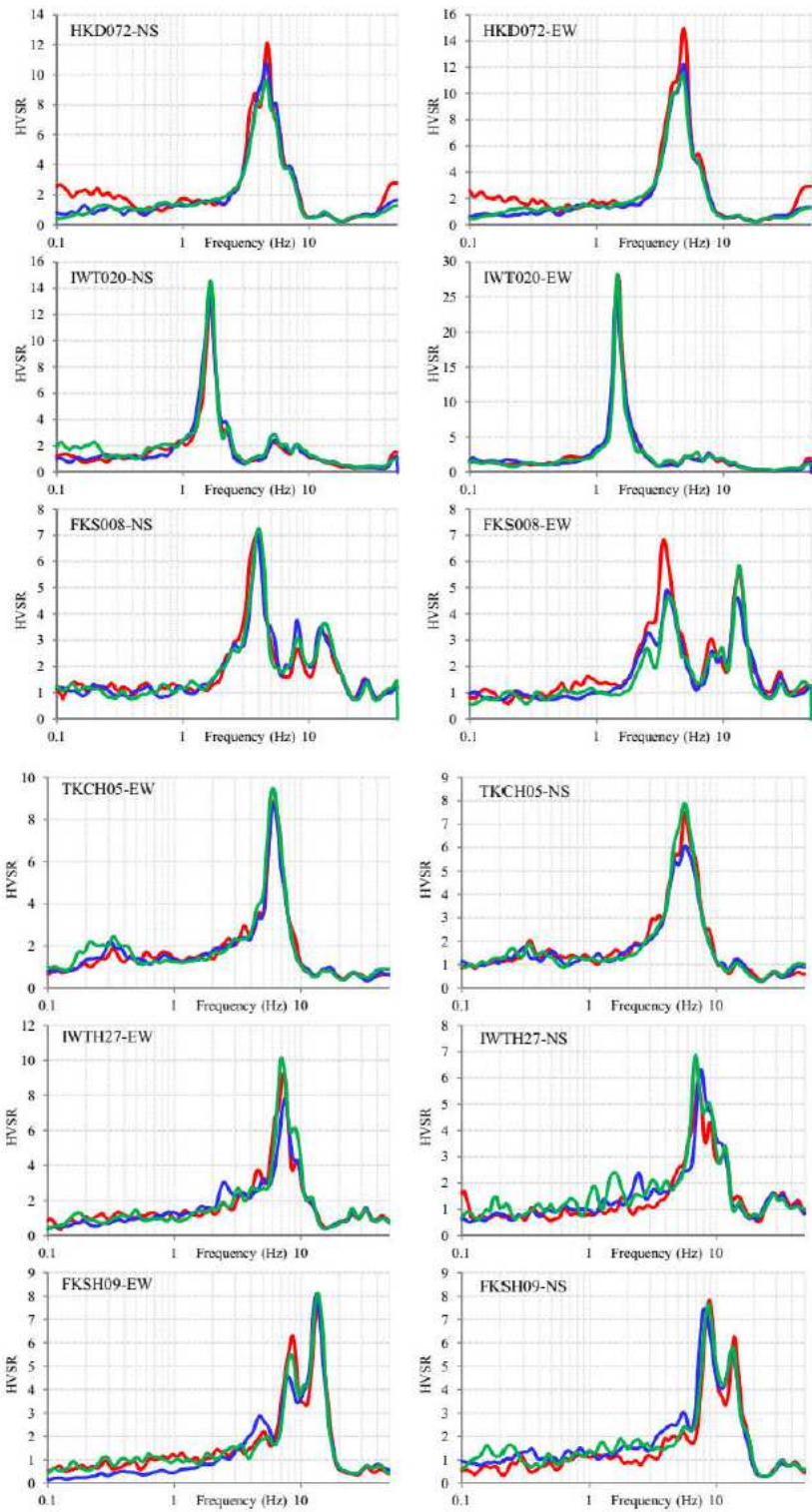


**Figure 28**

Examples of HVSRs at the three different study areas due to recorded EFWs or Er.FWs in Akita-Iwate area (blue), EFZs (red), EHWs or EI.FWs in Akita-Iwate area (green).

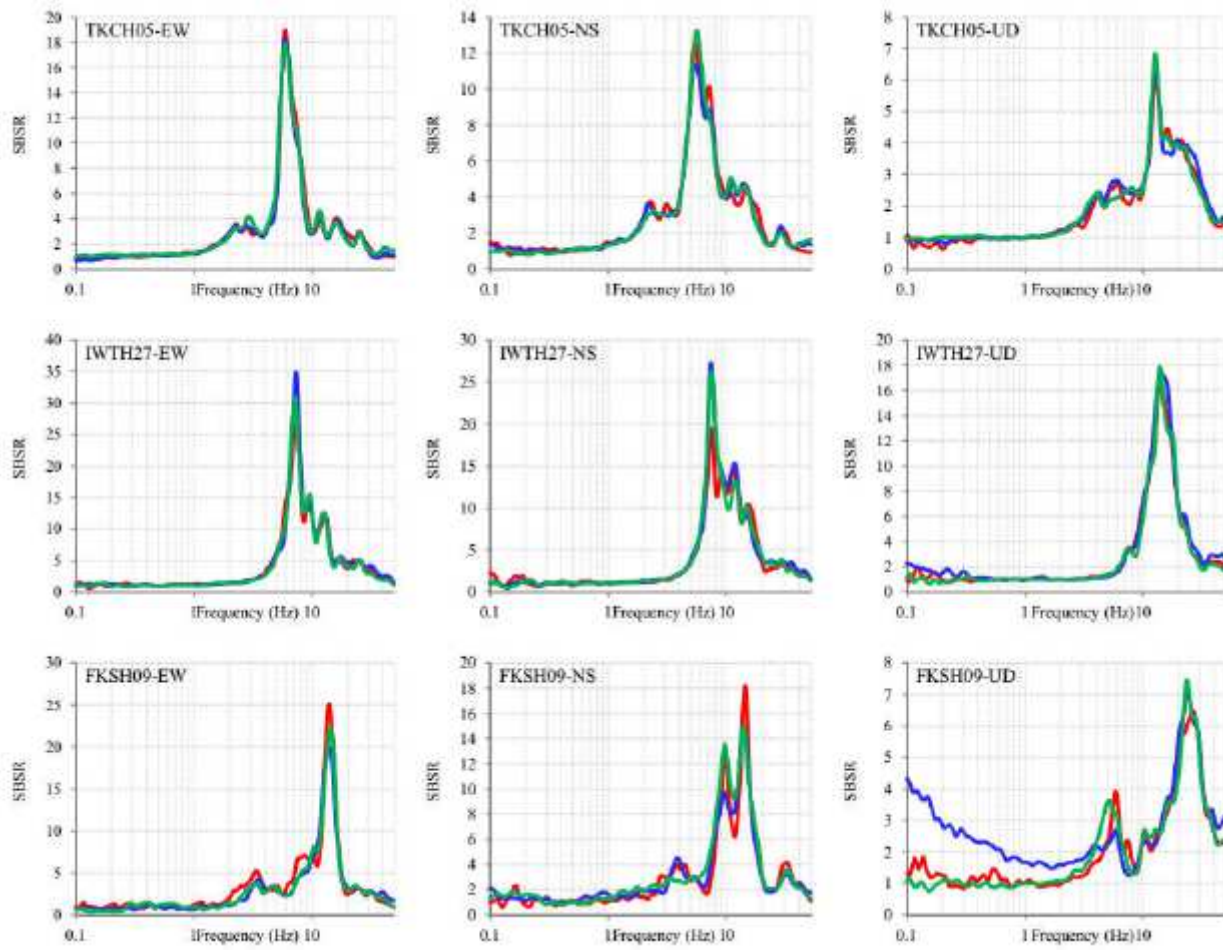


**Figure 29**

Examples of SBSRs at the three different study areas due to recorded EFWs or Er.FWs in Akita-Iwate area (blue), EFZs (red), EHWs or EI.FWs in Akita-Iwate area (green).

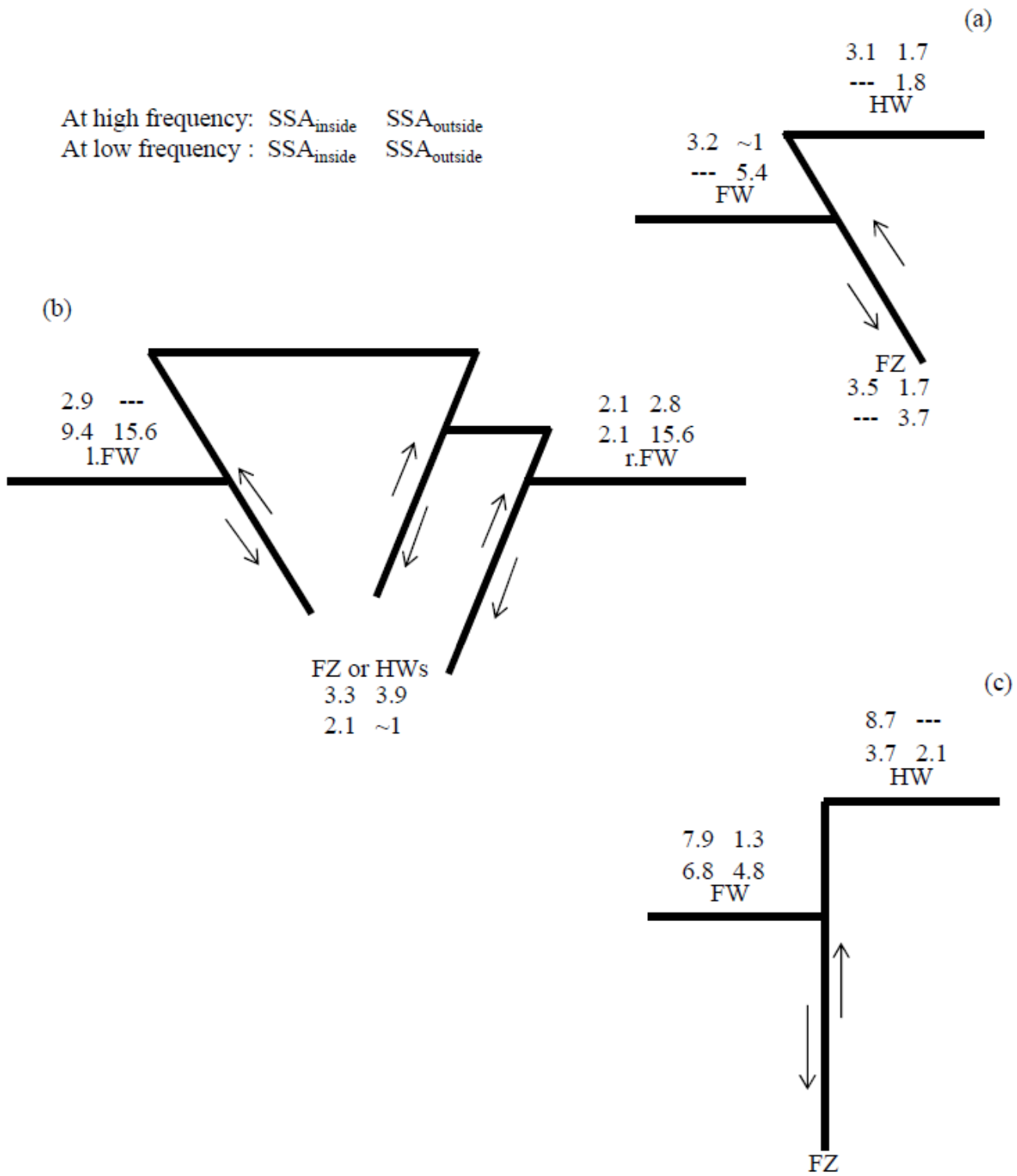


**Figure 30**

Schematic representations of active fault zones for the three present case studies. (a) East Hokkaido area, (b) Akita-Iwate area, and (c) Fukushima area. ( $SSA_{inside}$  and  $SSA_{outside}$  are the maximum of averages of SSA (refer to Tables 5, 6, and 7) due to sources inside and outside the active fault zones, respectively.)

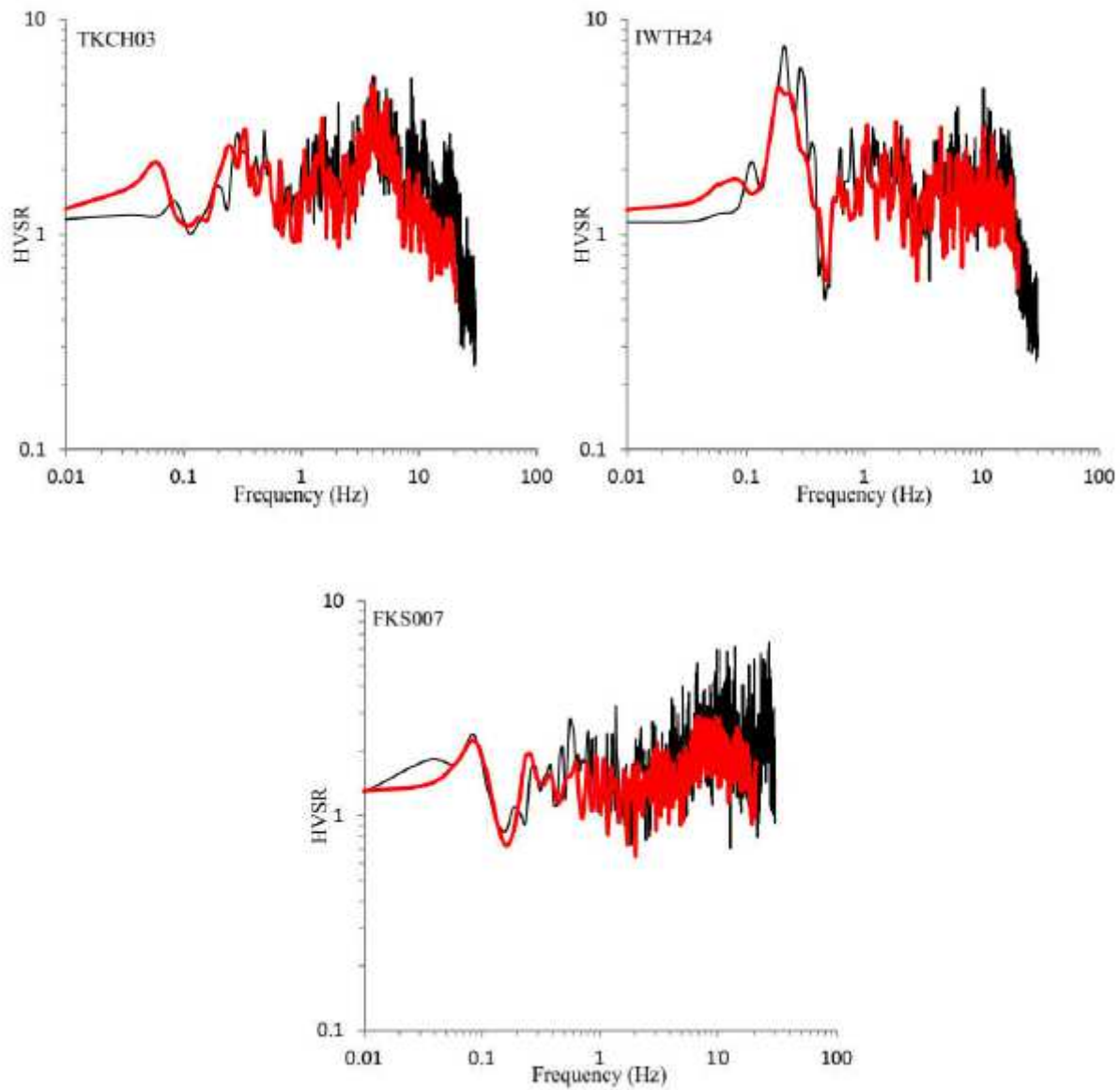


**Figure 31**

Examples of inverted EHVSs (red) superimposed with observed HVSRs (black) at three seismic stations on fault zones of the present study.

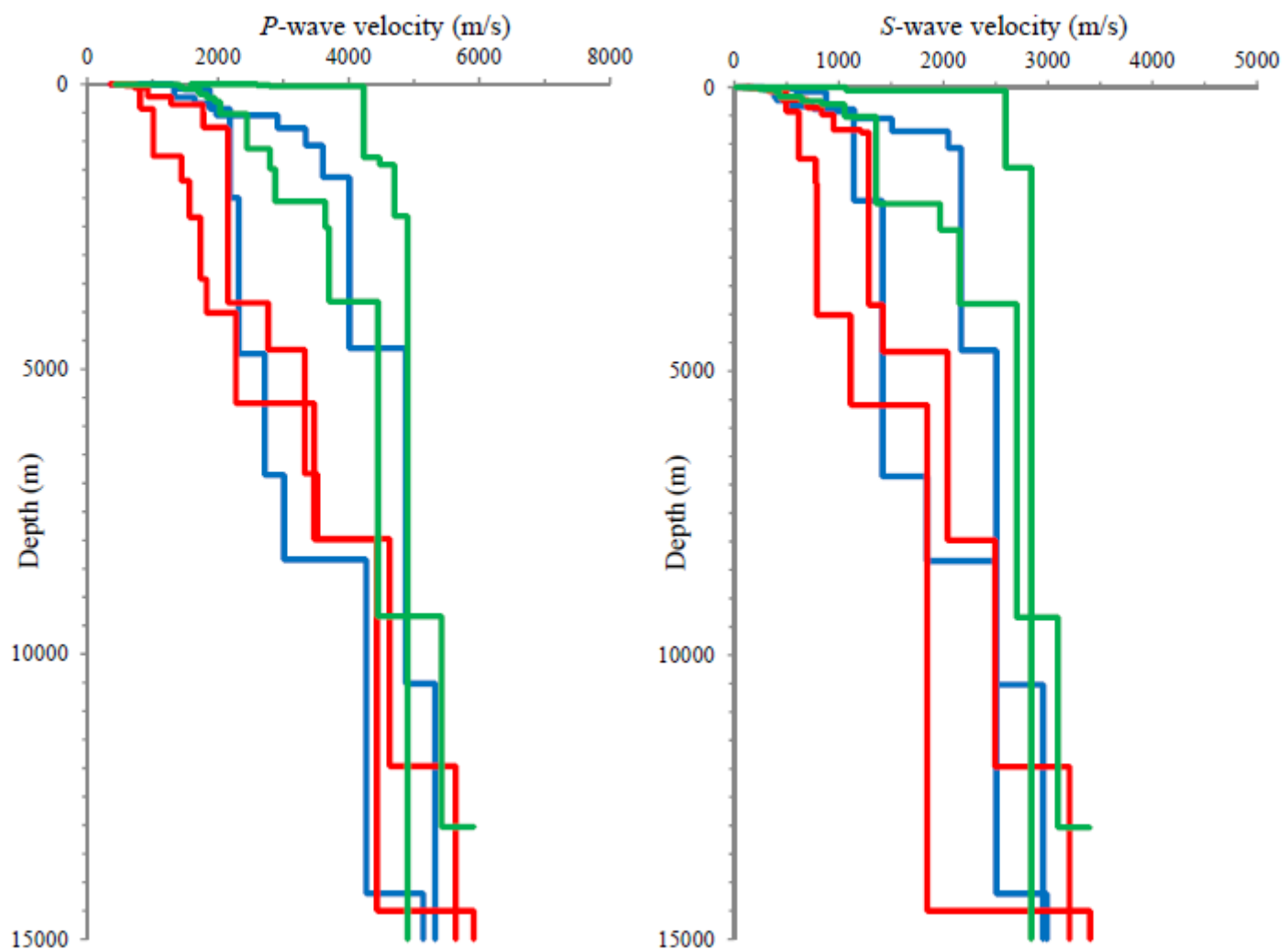


**Figure 32**

Inverted velocity structures in the East Hokkaido study area beneath stations on FW (blue), FZ (red), and HW (green).

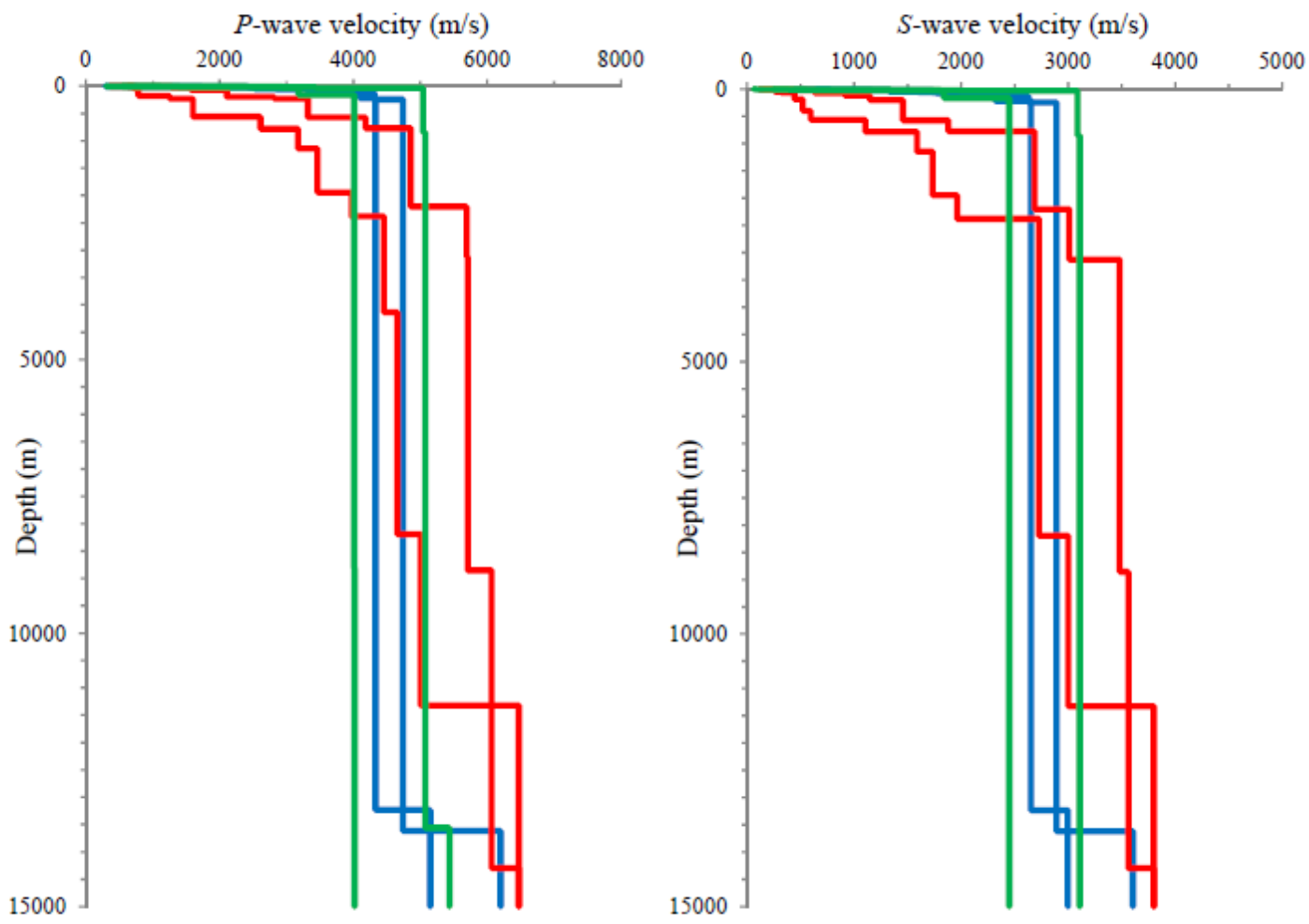


**Figure 33**

Inverted velocity structures in the Akita-Iwate study area beneath stations on r.FW (blue), FZ (red), and I.FW (green).

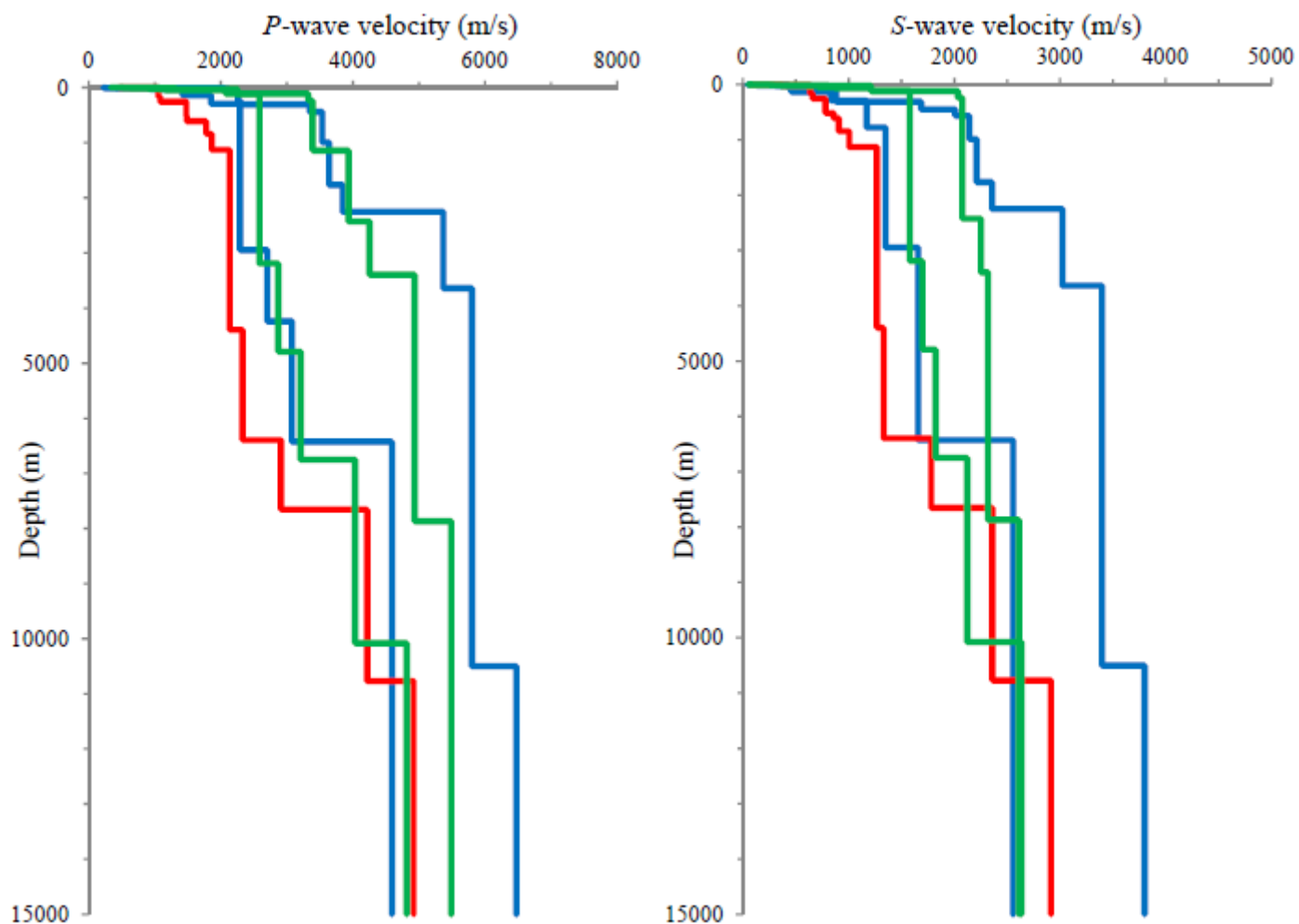


**Figure 34**

Inverted velocity structures in the Fukushima study area beneath stations on FW (blue), the closest to FZ (red), and HW (green).